Università degli studi di Napoli “Federico II”

DOTTORATO DI RICERCA IN FISICA

Ciclo XXIX

Coordinatore: prof. Salvatore Capozziello

Study of ν_τ properties with the SHiP experiment

Settore Scientifico Disciplinare FIS/01

Dottoranda
Annarita Buonaura

Tutore
Prof. Giovanni De Lellis

Anni 2014/2017

TABLE OF CONTENTS

INTRODUCTION

SHiP (Search for Hidden Particles) is a new general purpose fixed target experiment proposed at the CERN SPS accelerator looking for new particles with very weakly couplings and masses in the GeV region in the intensity frontier, thus complementing the energy-frontier physics program of LHC.

Thanks to the peculiar properties of the facility, the SHiP experiment can also be considered a Standard Model neutrino factory, in particular of tau neutrinos. Hence, it will host a neutrino detector to discover the tau anti-neutrino and to study tau neutrino and anti-neutrino cross-sections.

This detector will have a modular structure and will employ the Emulsion Cloud Chamber (ECC) technology, largely exploited by the OPERA experiment, interleaving lead plates acting as passive material and emulsion films acting as tracking devices with micrometric resolution. The micrometric resolution provided by the use of emulsions will allow to disentangle the τ lepton production and decay vertices, and to look for light Dark Matter (DM) particles produced via the decay of the dark photon. The detector is called Neutrino Detector and it is optimal for the detection of all three neutrino flavours as well as for the dark matter scattering. The Neutrino Detector will be placed in magnetic field so to allow the reconstruction of the charge of the τ lepton daughters and hence discriminate ν_τs from $\bar{\nu}_\tau$s. It will be followed by a magnetic spectrometer made of iron layers with high precision tracking stations to measure the charge and the momentum of muons produced in charged current muon neutrino interaction or in $\tau \rightarrow \mu$ decays.

My Ph.D. research activity, developed within the Napoli neutrino group and emulsion laboratory, has been mainly focussed on the design study of the Neutrino Detector and on the evaluation of its performances.

The first part of my work was devoted to carry on the studies which have ended up in the Technical Proposal of the experiment which was submitted to the SPS Committee in April 2015.

Starting from a simulation of 400 GeV protons impinging on the SHiP target, I have evaluated the expected signal and background yield for all the different neutrino flavours. I have also studied the potentiality of SHiP in measuring the structure functions F_4 and F_5 accessible only in ν_τ interactions. I have later focused my attention on studying the SHiP performances in the measurement of the ν_τ anomalous magnetic moment and in light (o(GeV)) dark matter detection. In both cases the signal is constituted by neutrino/DM scattering off electrons and in both cases

the main background contributions comes from quasi-elastic electron neutrino/anti-neutrino interactions when protons in the final state are not revealed in the Neutrino Detector. I also estimated the distribution of muon neutrino interactions with charm production in the Bjorken x, y and E variables, providing these data to the NNPDF group. Their addition to the NNPDF3.0 NNLO fit has allowed to estimate the power of SHiP in constraining the strange quark content of the nucleon.

In the second part of my Ph.D. I contributed to the development of FairShip, the official software of the experiment implementing in the software the geometry of the whole Neutrino Detector and a class to insert neutrino interactions and eventual secondary particles decay products in the simulation.

I have also actively participated to two test beams. One was held at the CERN PS to measure the particles momenta and charge in magnetic field with a Compact Emulsion Spectrometer (a cell of 3 emulsion films interleaved with Rohacell planes a few centimetre thick). This detector is attached downstream of each brick in the Neutrino Detector and aims at measuring the charge of the hadronic τ daughters which do not reach the muon magnetic spectrometer placed downstream. The other test beam was performed at the CERN SPS in collaboration with the GEM Frascati group to test the matching of emulsions and GEM detectors which are one of the options for the target tracker in the Neutrino Detector. I am the corresponding author of a paper which presents the results of this test beam and that is going to be submitted to a journal.

The thesis is structured in 6 chapters:

Chapter 1 contains a brief review of the different beyond standard model theories which might be tested at a beam dump facility. An overview of the neutrino physics studies that can be performed with the Neutrino Detector is then presented.

Chapter 2 reports the feasibility studies for the construction of the SHiP dump facility at CERN-SPS complex, describing: the beam line design, the target with its surrounding target complex and the muon shield necessary to bend out the muons produced in the proton interactions.

Chapter 3 gives an overview of the SHiP experiment, describing both the Neutrino Detector as I have implemented in the FairShip software and the detector to reveal the Hidden Sector. A short summary of the SHiP sensitivity to Hidden Sector particles is also reported, together with the project schedule.

Chapter 4 contains the results of the simulation studies to estimate the performances of the Neutrino Detector. The studies that have led me to evaluate the expected signal and background yields, together with the performances of the Neutrino Detector for ν_τ magnetic moment and light dark matter searches and for evaluating the s-quark content of the nucleon are here presented.

Chapter 5 contains the preliminary studies for the optimisation of the SHiP detector in view of the Technical Design Report. A new layout for the neutrino detector is presented and an overview of the overall detector performances is reported. In the last part of the chapter, a study on the electron and muon background is also described.

Chapter 6 describes the Test Beam activities I was involved in at CERN and the corresponding data analysis which I carried out in the Napoli Emulsion Laboratory. It also describes the analysis procedure for nuclear emulsion films and it gives the results obtained.

CHAPTER 1

PHYSICS MOTIVATION

1.1 Introduction

Since the mid of 1970s when the current formulation was finalised, the Standard Model (SM) of elementary particle physics has successfully explained a wide variety of experimental results, becoming the most validated theory to describe the fundamental constituents of Nature together with their interactions.

The most recent and striking proof of the validity of the SM was the discovery of a Higgs boson-like particle, announced by the ATLAS [1] and CMS [2] collaboration on the 4^{th} of July 2012.

Even though no significant deviation from the SM has been found so far, neither in direct nor in indirect searches, it cannot be considered the exhaustive theory of particle physics. As a matter of fact, it leaves some observed phenomena unexplained:

- *Neutrino masses*: It has been proved that neutrinos have non null masses as hypothesised instead in the SM. However, unlike the other particles, it is still not clear how these masses are acquired. The mechanism cannot be the same of the other fermions because, to couple with the Higgs field, a right-handed neutrino is needed, not foreseen in the original version of the SM. The introduction of a right-handed field ν_R would allow to form a Dirac mass term generated by coupling to the Higgs field, as it occurs for quarks and charged leptons. Calling Y_ν the associated Yukawa coupling, $m_D = Y_\nu v/\sqrt{2}$, where $v = 246$ GeV is the electroweak vacuum expectation value (vev). Nevertheless a neutrino mass of the order of 0.1 eV would result in a Yukawa coupling $Y_\nu \sim 10^{-12}$, several order of magnitudes smaller than other Yukawa couplings.

- *Baryon asymmetry of the Universe (BAU)*: Just after the Big Bang the Universe was so hot

that the energy was enough to create pairs of particles and antiparticles. As the Universe cooled,the annihilation process among particles and antiparticles started to dominate over their creation. If the amount of matter and anti-matter had been the same, everything would have disappeared. Our existence is the direct proof that there must have been more matter than antimatter. However, the SM can't explain this tiny (about one particle per billion) matter-antimatter imbalance in the early Universe. Indeed, the SM satisfies the three Sakharov conditions [3] but the CP violation, which occurs through the CKM mass matrix, is too small ($\epsilon_{CP} \sim 10^{-20}$) to account for the observed value of the baryon asymmetry ($\eta_B = \frac{n_B}{n_\gamma} \approx 10^{-10}$, being n_B the baryon density and n_γ the photon density).

- *Dark Matter (DM) and Dark Energy (DE)*: By fitting a theoretical model for the composition of the Universe with the combined set of cosmological observations, it has been estimated that ordinary matter accounts for only 5% of the total composition of the Universe. The remaining 96% is made by ~ 68% of DE and ~ 27% of DM. Dark Matter does not interact with the electromagnetic force: it does neither absorb, nor reflect or emit light, but it has gravitational effects which have brought to its discovery. Dark Energy seems to be related with the vacuum in space: it does not have any local gravitational effects, but a global effect on the Universe as a whole, thus influencing the expansion rate of the Universe itself.

These experimental evidences suggest the presence of new physics Beyond the Standard Model (BSM), however neither experiments nor theory provide clear hints on the nature and the scale of new physics.

The yet unknown particles or interactions that could solve the problems of the SM could be searched for either going at always increasing energies (the so-called *energy frontier* research) or focusing on very weakly couplings (the so-called *intensity frontier* research). The two options are schematically shown in fig. 1.1.

The first path is being explored in the last decades by the major particle physics experiments, such as ATLAS [4], CMS [5], LHCb [6]. The second one is still largely unexplored and could be investigated in beam dump facilities where ultra-rare processes can be studied being the number of interactions maximised.

The purpose of this chapter is to provide a review of the physics that can be explored at a proton beam dump facility for both SM and BSM scenarios. A detailed description is given in [7]. The first part of the chapter is devoted to a summary of BSM theories that foresee a so called Hidden Sector (HS), while in the second part the physics studies that can be performed using SM neutrinos will be described.

1.2 The Hidden Sector

The hypothetical BSM particles that have not been detected so far because they are either too light or do not couple directly to the SM constitute the Hidden Sectors.

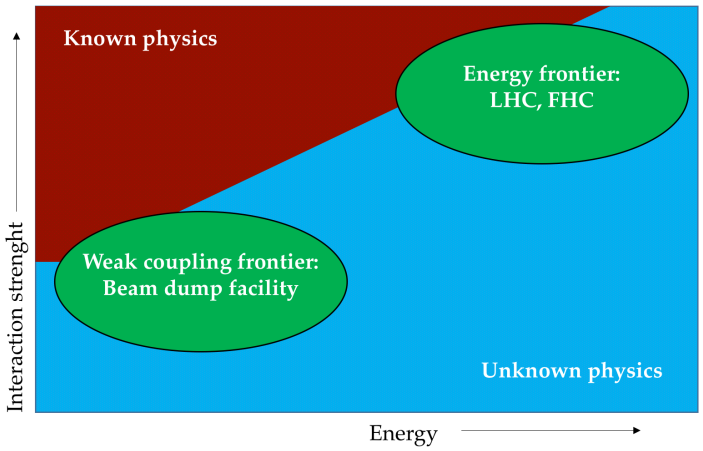

Figure 1.1: The two options to search for new physics: the intensity frontier and the energy frontier.

Hidden Sector particles can be produced at beam dump experiments:

- in the decay of mesons and baryons produced in the initial collision;
- in (quasi) elastic scattering of incident protons on the target nucleons with subsequent production of vector states via bremsstrahlung processes;
- through $q\bar{q}$ fusion.

If these particles couple to the SM via renormalisable interactions with small dimensionless coupling constant, it is possible to talk about Hidden Portals. Another option foresees their coupling to the SM by highly-dimensional operators suppressed by the dimensionful couplings Λ^{-n}, corresponding to a new energy scale of the HS.

The renormalisable portals for the SM are of three types, according to the mass dimension of the SM singlet operator.

1. **Vector portal:** The singlet operator has the dimension of a mass squared (GeV^2). The new particles are Abelian fields which couple to the hypercharge field though a dimensionless coupling ϵ which characterises the mixing between the new vector field with the Z-boson and the photon.

2. **Scalar portal:** The singlet operator has the dimension of a mass squared (GeV^2). The new particles are scalar fields coupled to the square of the Higgs field.

3. **Neutrino portal:** New neutral singlet fermions are introduced, coupling to singlet operators ($\bar{L}_\alpha \cdot \tilde{\Phi}$) with a dimension of $\text{GeV}^{\frac{5}{2}}$.

1.2.1 Vector Portal

It is possible to derive the SM gauge structure (SU(3)×SU(2)× U(1)) from a larger gauge group. In Grand Unified Theories (GUTs), the new vector fields are very heavy: masses are of the order of 10^{16} GeV. However, if additional gauge structures, as in the case of multiple U(1)'s (SU(3)×SU(2)× $[U(1)]^n$), accompany the SM, (sub-)TeV gauge bosons are also allowed. The LHC sets very strong bounds on these new vector states associated to the new U(1) gauge groups at the TeV scale [8, 9], but it provides very poor constraints to light vector states in the GeV mass range and with small couplings to the SM [10].

The simplest way to couple a new vector particle to the SM is to use the kinetically-mixed portal. In this case, none of the SM fields needs to be charged under the new gauge groups.

Minimalistic models consider a U(1)' gauge symmetry in the hidden sector with an associated gauge boson A' called *dark photon*. The SM lagrangian is extended to:

$$\mathscr{L} = \mathscr{L}_{SM} - \frac{1}{4}F'_{\mu\nu}F'^{\mu\nu} + \frac{\epsilon}{2}F'_{\mu\nu}F^{\mu\nu} + \frac{m^2_{\gamma'}}{2}A'_{\mu}A'^{\mu} \tag{1.1}$$

$F'_{\mu\nu} = \partial_\mu A'_\mu - \partial_\nu A'_\nu$ is the new field A' strength tensor. The term $F'_{\mu\nu}F^{\mu\nu}$ represents the interaction term among the dark photon and the SM one and it is assumed to multiply a small factor ϵ.

If a new Higgs field is present in the dark sector (*dark Higgs*) then the U(1)' gauge symmetry might be broken by a Higgs-like mechanism and the dark photon acquires a non-zero mass ($m_V = g' \cdot v'$). Extra interactions are also introduced. According to the relative sizes of the quartic coupling λ and the square of the gauge coupling g'^2, the dark Higgs can be heavier or lighter than the dark photon.

The vector portals are of great interest because they might help solving several known problems of the SM.

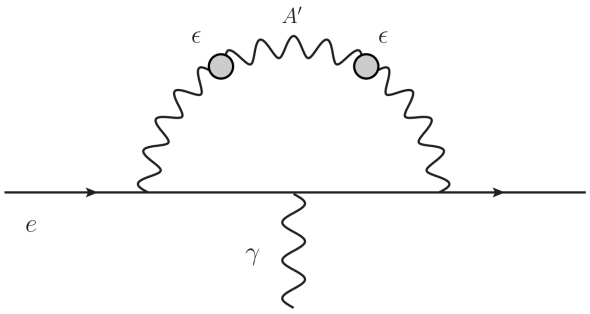

Figure 1.2: One-loop correction to the muon anomalous magnetic moment due to the exchange of the dark photon.

Light mass vector particles might provide a solution to the muon $g-2$ discrepancy. As a matter of fact, a simple one-loop diagram (as the one shown in fig. 1.2) can give a positive correction to the magnetic anomaly:

$$a_l^V = \frac{\alpha}{2\pi}\left(\frac{g'}{e}\right)^2 \times \begin{cases} 1 & \text{for } m_l \gg m_V \\ 2m_l^2/(3m_V^2) & \text{for } m_l \ll m_V \end{cases} \tag{1.2}$$

For the dark photon, $g'/e = \epsilon$ and choosing $\epsilon \sim$ few $\times 10^{-3}$at $m_V \sim m_\mu$ theory and experimental results would be in agreement.

Light mass vector particles can also be thought of as mediators of the interaction with DM and provide an explanation to the astrophysical positron excess.

In a beam dump experiment, dark photons can be originated via:

1. *Meson decays*: Mesons are copiously produced in proton on target collisions. The most important process is $\pi^0 \to \gamma A$, which is suppressed by ϵ^2, but not α, being the π^0 decay an electromagnetic process. Weak decays of K and D mesons have instead a subdominant role. Chances of dark photons to be originated in the decays of $\eta, \rho/\omega$ and Δ have also been taken into account [11].

2. *Proton bremsstrahlung*: The (quasi)elastic scattering of incident protons on nucleons in the target can lead to the production of vector states via bremsstrahlung process $pp \to ppA$ [12].

3. *Direct perturbative QCD production*: Processes like $q + \bar{q} \to A$ and $q + g \to q + A$ become dominant for larger masses of the vector particles [13].

The decay width of the dark photon is given by:

$$\Gamma_{A'} = \sum_l \Gamma_{A' \to l^+ l^-} + \sum_{hadrons} \Gamma_{A' \to hadrons} + \sum_\chi \Gamma_{A' \to \chi\bar{\chi}} \tag{1.3}$$

The last term represents the possibility for a dark photon to decay in new dark states χ which are charged under U(1)'. By looking at the explicit expression of the different partial widths, it can be noted that, if dark states are kinematically accessible, then "visible" vs "dark" decay widths scale as $\approx \alpha\epsilon^2/\alpha_D$ (here $\alpha_D = g'^2/4\pi$). Choosing specific parameters, it can be seen that in the absence of dark decays, (boosted) dark photons can propagate over macroscopic distances. On the other hand, if dark decays are dominant ($2m_\chi < m_{A'}$ and $\alpha_D \gg \alpha\epsilon^2$), the only model-independent signature is the missing energy decays of A'. If the χ states do not decay into lighter dark states then they can scatter on SM particles, such as electrons or nucleons and nuclei, via the exchange of the mixed γ - A' propagator (fig. 1.3).

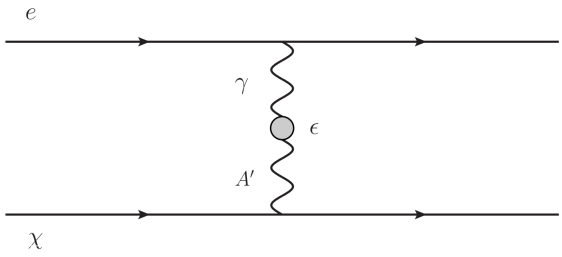

Figure 1.3: Interaction through the exchange by a mixed γ - A' propagator between the SM particles and particles χ.

The sub-GeV Dark Matter model Hints of the existence of the Dark Matter (DM) come from a variety of gravitational signatures.

If DM was made of particles, they could either be relativistic when decoupling from the early Universe plasma (Hot Dark Matter, HDM) or non relativistic (Cold Dark Matter, CDM). In the Λ_{CDM} model for the early Universe, the dominant component is the CDM.

The preferred CDM candidates are the WIMPs (Weakly Interacting Massive Particles). These particles should have a mass $\sim M_{W,Z}$, must be neutral and very weakly interacting with all the other known particles (the cross-section is $\sigma < 10^{-6}$ pb). So far experiments have not found any hint on DM mass particles.

High intensity fixed target experiments can probe sub-GeV DM with a sensitivity not achievable otherwise.

A simple benchmark model for Light Dark Matter (LDM) uses the vector portal with a light dark photon (see 1.2.1) as a mediator (see e.g. [14–17]). The lagrangian for this model is:

$$\mathscr{L} = \mathscr{L}_\chi - \frac{1}{4}V_{\mu\nu}V^{\mu\nu} + \frac{1}{2}m_V^2 V_\mu V^\mu - \frac{\epsilon}{2}V^{\mu\nu}F_{\mu\nu} + q_B g' V_\mu J_B^\mu \tag{1.4}$$

where g' is the Gauge coupling and q' is the charge of the DM field χ, which can be considered either as a scalar field or as a fermionic field under the additional gauge symmetry U(1)'. The U(1)' charge can be identified with the baryon number, giving two different mediation channels:

- Vector portal, which is UltraViolet (UV) complete[1] and can be obtained by setting q_B=0 in eq. 1.4;
- Baryonic Vector Mediatior, which requires additional UV completion to ensure anomaly cancellation.

Assuming the Light Dark Matter (LDM) to be a thermal relic requires to have annihilation channels through light mediators to avoid over production in the early Universe. The minimal

[1]Its correlation functions or amplitudes can be calculated and yield unambiguously finite results for arbitrarily high energies

vector portal model provides a natural thermal relic DM candidate. The annihilation rate ($\chi + \bar{\chi} \rightarrow f + \bar{f}$) determines the freeze out abundance. Constraints on its value results in limits on the parameters $\epsilon, \alpha' = g'/4\pi, m_V, m_\chi$.

There are three different reactions that can originate LDM from a dark photon:

- π^0/η *decay in flight*: This process is relevant for small dark photon masses:

  $$\pi^0/\eta \rightarrow \gamma + V^{(*)} \rightarrow \gamma + \chi^\dagger + \chi$$

  $(*)$ indicates that the dark photon can be on-shell or off-shell in the production process, depending on whether the condition $m_{A'} > 2m_\chi$ is verified or not.

- *Bremsstrahlung and resonant vector mixing:* This process is relevant for small dark photon masses:

  $$p + N \rightarrow p + N + V$$

  In this case the DM particle is produced with a very little angular spread and therefore can be revealed in on-axis detectors in a fixed target experiment.

- *Direct production:* This corresponds to a parton level process like:

  $$p + N \rightarrow V^* \rightarrow \chi^\dagger \chi$$

LDM particles can be detected by observing one of the following processes (the relative Feynman diagrams are reported in fig. 1.4):

- Electron scattering
- Inelastic Neutral Current π^0-like nucleon scattering
- Deep Inelastic Scattering

The most stringent constraints, that do not however rule out MeV-scale dark matter models, come from the LSND experiment [18], an 800 MeV neutrino experiment collecting 1.8×10^{23} protons on target, with a $\nu - e$ scattering analysis recasted as a constraint on light dark matter [19]. A dedicated search for light dark matter stases produced by the decay of the dark photon is currently ongoing at MiniBooNE [20] and several papers have reported a dedicated study of the detection of this light dark matter [13, 21–23].

1.2.2 Scalar Portal

Many extensions of the SM Higgs sector foresee additional light scalar or pseudoscalar particles that are singlet under the SM gauge group and have highly suppressed couplings to SM particles.

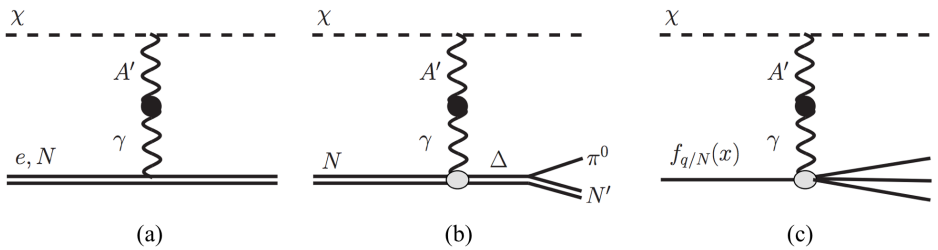

Figure 1.4: Feynman diagrams showing the different interactions LDM can undergo: elastic scattering on electrons or nucleons (a), quasi-elastic (incoherent) single pion production (b), and deep inelastic scattering (c).

These scalar states can also arise as pseudo-Nambu- Goldstone bosons (PNGB) of a spontaneously broken symmetry.

If the HS is made of scalar fields, the portal operators in the extended lagrangian are renormalizable. Therefore, if the interactions between the extra scalar and the Higgs boson are generated at very high scales such as the GUT or the Planck scale, they can remain as a relevant interaction down to the energy scales probed by experiments today. Furthermore, since DM is neutral under all SM gauge interactions, it is possible that the additional scalars coupled through the Higgs portal can either play a role in dark sector physics, or be the DM candidates.

When including an additional (CP-even) singlet scalar, the SM lagrangian modifies as follows:

$$\mathscr{L} = \mathscr{L}_{SM} + \frac{1}{2}\partial_\mu S \partial^\mu S + (\alpha_1 S + \alpha S^2)(H^\dagger H) + \lambda_2 S^2 + \lambda_3 S^3 + \lambda_4 S^4 \tag{1.5}$$

where $\lambda_{2,3,4}$ are the scalar self couplings while α_1 and α represent the portal couplings to the SM Higgs doublet H.

For a light scalar with a mass well below the Higgs mass ($m_S \ll m_h$) and in the limit of a small α_1 coupling, the mixing angle is given by:

$$g_* = \sin\theta \simeq \theta \simeq \frac{\alpha_1 v^2}{m_h^2}$$

where $v = 246$ GeV denotes the electroweak vacuum expectation value (vev). In this case, both the production mechanisms and decay modes coincide with those of a SM Higgs boson having the same mass of the considered light scalar. However, with respect to the Higgs boson, the production cross sections and the decay rates are suppressed by a factor g_*^2. Figure 1.5 [24] shows the decay branching ratios as a function of the scalar mass m_S, the gap around 2 GeV is due to the appearance of a large number of hadronic resonances.

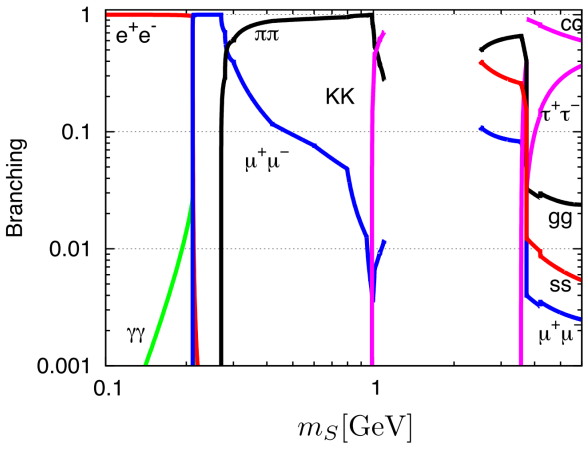

Figure 1.5: Decay branching ratios as a function of the scalar mass m_S [24]

1.2.3 Neutrino Portal

The Neutrino Minimal Standard model (νMSM) [25, 26] is a minimalistic model that solves the SM puzzles by inserting three heavy right-handed neutrinos that couple to the left-handed SM neutrinos (see fig. 1.6). These heavy neutrinos are sterile, i.e. they do not couple, apart from gravity, to any of the fundamental SM interactions, and are also referred to as Heavy Neutral Leptons (HNLs).

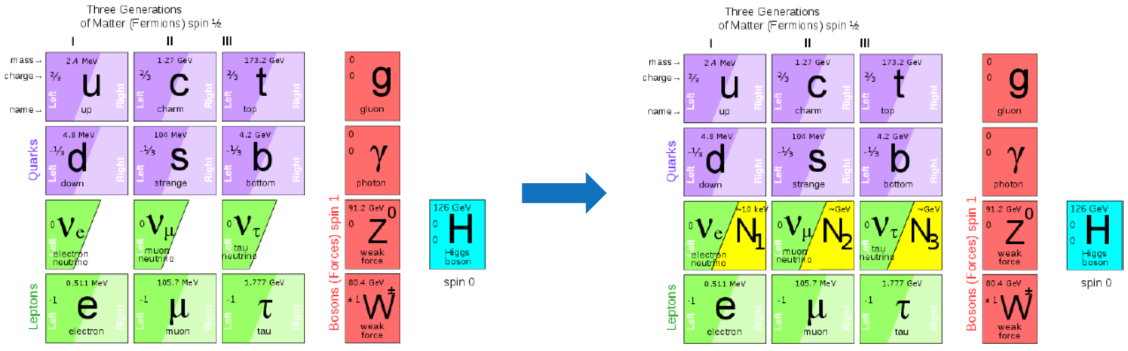

Figure 1.6: Particle content of the SM (left) and of its minimal extension, the νMSM where right-handed partners of SM neutrinos are added.

HNLs are singlets with respect to the SU(2)×U(1) group and they couple to the Higgs boson. Their introduction modifies the SM lagrangian in the following way:

$$\mathscr{L} = \mathscr{L}_{SM} + \overline{N}_i i\partial N_i - U_{i\alpha}\Phi N_i L_\alpha - \frac{M_i}{2}\overline{N}_i^c N_i + h.c. \tag{1.6}$$

where:

- N_i is the HNL field;
- $U_{i\alpha}$ is the Matrix of the Yukawa couplings with $\alpha = e, \mu, \tau$
- Φ is the Higgs field
- L_α are the SM left-handed lepton fields
- M_i are the Majorana masses

Requiring the Majorana mass to be of the order of the electroweak scale forces the Yukawa couplings to be very small: $U_i^2 \approx O(m_\nu M_i / v^2) \approx 10^{-15}$, where v is the vacuum expectation value of the Higgs field (246 GeV) and m_ν are the masses of active neutrinos.

In the model of ref. [25, 26], the lightest of the HNL, N_1 has a mass of a few keV and it is a DM candidate with a lifetime bigger than the lifetime of the Universe. It can decay either in three neutrinos (invisible) or in a photon and a neutrino ($N_1 \to \nu\gamma$). In the latter case, it can be searched for by looking for a monochromatic line with energy of a few keV. In 2014, two possible signals hinting at this decay were observed, details of the measurements are reported in [27, 28].

On the other hand, N_2 and N_3 are degenerate in mass, in the MeV-GeV range. They can explain the baryon asymmetry through a process of leptogenesis made possible by their lepton number violating Majorana mass term [26, 29–31]. Furthermore, they can provide an explanation to the observed pattern of neutrino masses through the type I see-saw mechanism [25].

HNLs can be produced in association with a charged lepton in 2-body meson decays, and in 3-body meson decays into HNL, light (pseudoscalar or vector) meson and a charged lepton. Possible HNL production mechanisms are shown in the left panel of fig. 1.7. It is exactly their mixing with active neutrinos through the Higgs boson that makes them unstable. They decay emitting a charged lepton and a vector boson (W or Z) giving rise to final states containing either another charged lepton or hadrons:

$$N_i \to e^+e^-\nu, \mu^+\mu^-\nu, \mu^\pm e^\mp \nu, \tau^+\tau^-\nu \text{ , etc} \tag{1.7}$$

$$N_i \to \pi^\pm e^\mp, \pi^\pm \mu^\mp, K^\pm e^\mp, K^\pm \pi^\mp \nu \text{ , etc.} \tag{1.8}$$

Potential two- and three-body decay modes of $N_{2,3}$ are shown in the right panel of fig. 1.7.

1.2.4 Axion Like Particles

While the new particles hypothesised by the models described in the previous sections are coupled to the SM via renormalizable interactions with small dimensionless coupling constants, Axion Like Particles (ALPs) would couple via a higher(5)-dimensional operator.

Pseudo-Nambu-Goldstone bosons (PNGBs) come from spontaneously broken global symmetries (U(1) or other groups). They exhibit two crucial properties:

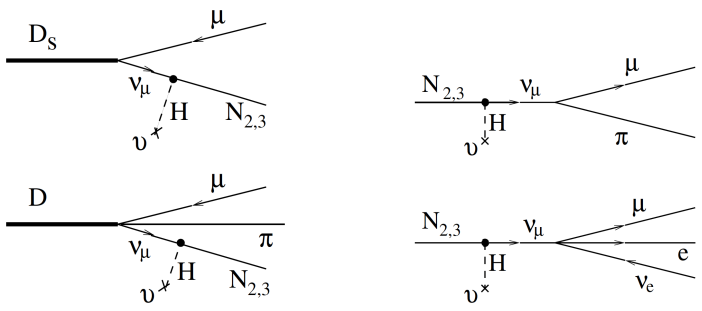

Figure 1.7: Feynman diagrams for the production of HNLs (left) and for their decays (right). The dashed line denotes the coupling to the Higgs vacuum expectation value, leading to the mixing of active neutrinos and HNLs via Yukawa couplings.

1. *Small couplings:* Their interactions are suppressed by the scale of spontaneous symmetry breaking f_A

2. *Small mass:* A small explicit breaking of the symmetry at a scale Λ leads their mass to be suppressed by the scale of spontaneous symmetry breaking: $m_A \simeq \Lambda^2/f_A$.

An example of a very light PNGB is the axion.

The axion comes from the breaking of the Peccei-Quinn U(1) symmetry related to the axial anomaly of QCD [32–35]. It was introduced to solve the strong CP problem in QCD and, according to the considered model, it can either couple to two gauge bosons or present derivative couplings to SM fermion. Its mass is fixed by the QCD anomaly and by the scale of symmetry breaking and it is slightly model dependent.

Axion Like Particles are pseudo-scalar particles with interactions similar to the axion and different masses.

ALPs are predicted in string theory, in extended Higgs sectors. They can also appear in quantum field theory on torsion manifolds [36–38] or they can be originated in spontaneously broken global flavour symmetries and in this latter case they are called familons [39].

ALPs can also help solving the DM puzzle providing a mediator between DM and SM particles together with additional annihilation channels relevant for the thermal freeze-out of DM. Indeed, if the pseudoscalar is lighter than the DM particle χ, $\chi\bar{\chi} \to A\bar{A}$ with subsequent decay of the ALPs into SM particles, allows for the highly efficient annihilation of DM particles. However, it is important to require that the ALPs produced in DM annihilations decay before Big Bang Nucleosynthesis (BBN). This request sets a lower bound on the couplings between the pseudoscalar and SM states.

To probe untested regions in parameter space both for ALPs coupled to two gauge bosons and for those coupled to SM fermions, the following production modes can be considered, either direct from proton interaction:

$$pp \to A + X, \qquad A \longrightarrow \gamma\gamma$$

or via B-meson decay:

$$pp \to B + X \to A + K + X, \qquad A \longrightarrow \mu^+\mu^-$$

1.2.5 SUSY

Supersymmetry (SUSY) is one of the most motivated extension of the SM where bosons and fermions are connected.

The minimal supersymmetrical model considering only the minimum number of new particle states and new interactions consistent with phenomenology is the *Minimal Supersymmetric Standard Model* (MSSM) [40]. A supersymmetric transformations changes a bosonic state in a fermionic one and vice-versa: each fermion has a bosonic partner with the same quantum numbers but with a spin which differs by half a unit. Therefore, in the MSSM there are both vector superfields associated with the Standard Model gauge groups which contain the vector bosons and associated gaugino and chiral superfields for the SM fermions and Higgs bosons with their respective superpartners.

If the supersymmetry were an exact symmetry, all the particles belonging to the same supermultiplet should have the same mass. Hence, we should have been able to observe a s-electron with the same mass of an electron, a squark u with the same mass of the quark u and so on. Since any of these observations has been done yet, the supersymmetry must be a broken symmetry.

The most general supersymmetric lagrangian contains terms violating both the boson and the lepton number, thus being in contrast with the non observation of proton decays. To explain the stability of the proton, the MSSM imposes a new discrete symmetry named *R-parity*, which associates to a particle or to its supersymmetric partner with spin s the quantic number $R = (-1)^{3(B-L)+2s}$ [41, 42]. R-parity is multiplicative quantic number which is also assumed to be conserved in the physical processes.

Supersymmetric searches are now spanning the mass region of 100 GeV - 10 TeV and are currently ongoing at LHC [43, 44]. However, the possibility that SUSY particles have a mass which is a couple of orders of magnitude lighter than the mass of the W and Z bosons has not yet been excluded neither from LHC searches nor from precision fits of the SM. There are indeed many supersymmetric models that still allow for new light neutral particles to be in the MeV to few GeV range that can be looked for at a beam dump experiment.

For example, even though a stable neutralino in the mass range between 0.7 eV and 24 GeV is excluded because it gives too much DM, if the possibility of the R-parity to be violated is introduced [45], than it becomes allowed. Not having a convincing theory of supersymmetry breaking leaves a lot of space to the experiments to investigate. In this case, however, the

neutralino cannot be considered a DM candidate anymore. This could instead be the axino, or the axion [46].

Neutralinos might be produced in the decays of $D^{\pm}$ or B mesons, via the diagrams in fig. 1.8 and can later decay in: $\tilde{N}_1^0 \longrightarrow K_{S/L}^0 + \overset{(-)}{\nu}$ or $\tilde{N}_1^0 \longrightarrow K^{\pm} + l^{\mp}$. Direct searches of neutralinos are complementary to those performed at the LHC and also allow to (indirectly) probe sfermions in the region of a few tens of TeV.

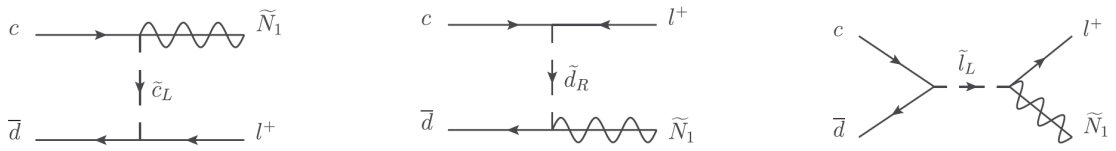

Figure 1.8: Relevant Feynman diagrams for neutralino production through D^+ meson decay.

1.3 Neutrino physics at a Beam Dump experiment

Since 1930 when neutrinos were firstly predicted by Pauli [47] and since their first observation done by Reines and Cowan in 1956 [48], the knowledge on the physics of such a tiny particle has significantly grown.

Nowadays, in particle physics neutrinos represent the only window into BSM physics. From observations, it is clear that neutrinos have a small non null mass and that they mix, thus implying the non conservation of the lepton number. Instead, according to the SM, neutrinos have three different flavours, zero mass and do not oscillate.

Today, neutrino oscillations are well established. After the first evidence reported by the Super-Kamiokande Collaboration in 1998 of a zenith-angle deficit in the number of up-going high energy ν_μ [49], neutrino oscillations were confirmed by the observation of the appearance of ν_τ and ν_e in a pure ν_μ beam by the OPERA [50] and the T2K experiment [51] respectively.

Neutrino oscillations are described by a simple and widely accepted extension to the SM where the three flavour eigenstates and the three mass eigenstates are connected by means of a 3×3 unitary matrix (the Pontecorvo - Maki - Nakagawa - Sakata matrix, PMNS). The PMNS matrix can be written in terms of three mixing angles and one CP-violation phase: $\theta_{12}, \theta_{23}, \theta_{13}, \delta_{CP}$.

The observation of $\nu_\mu \rightarrow \nu_e$ in appearance mode by the T2K experiment in 2014, with 28 ν_e events observed in a pure ν_μ beam leading to the exclusion of a $\theta_{13} = 0$ with a 7.3 σ significance [51] has led to the exclusion of a $\theta_{13} = 0$ with a 7.3 σ significance. Precise measurements of θ_{13} performed at reactor experiments (Daya Bay [52, 53], RENO [54, 55], Double Chooz [56, 57]) have estimated: $\theta_{13} = (9 \pm 0.5)^\circ$.

A non null value of θ_{13}, as well as of all the other mixing angles, allows to search for CP violation in the lepton sector. The latest results from T2K [58], obtained combining the analysis of

neutrino and antineutrino oscillations and using reactor measurements of $\sin^2 2\theta_{13}$ as additional constraint, show that the one-dimensional confidence interval at 90% for δ_{CP} ranges from -3.13 up to -0.39 for normal mass ordering. This analysis excludes the hypothesis of $\delta_{CP} = 0, \pi$ at 90% confidence level.

Direct neutrino mass measurements cannot be determined in oscillation experiments, because these experiments are sensitive only to the difference of the squared masses ($\Delta m^2_{21(32)}$), therefore they do not even provide information on the ordering of the neutrino masses (neutrino mass hierarchy problem).

To measure the neutrino mass in a direct and model-independent way, the low energy nuclear beta decay $H^3 \rightarrow He^3 + e^- + \bar{\nu}_e$ can be used. In this respect, results are awaited from the KATRIN experiment [59] which is expected to achieve a 0.2 eV (with about equal contributions of statistical and systematical errors) for the mass of the electron neutrino.

Hints on the neutrino mass hierarchy might come from searches for $0\nu\beta\beta$-decay, i.e. $(A,Z) \rightarrow (A,Z+2)+2e^-$, foreseen in several extensions of the SM. These studies would also allow to assess whether the neutrino is a Majorana or a Dirac particle. Results are expected from projects like MAJORANA [60], KamLAND-Zen [61], SNO+ [62] which will be able to reach a sensitivity of 20-50 meV on the effective Majorana mass $|m_{\beta\beta}|$ defined as:

$$|m_{\beta\beta}| = \left| \sum_i U_{ei}^2 m_i \right|$$

where m_i are the neutrino mass eigenstates and U_{ei} are the elements of the PMNS matrix.

Despite the progresses done in the recent years in the studies of neutrino physics, there are still lacking information about the third neutrino and anti-neutrino generations, with only 9 ν_τ events collected by the DONUT [63] and 5 the OPERA [50, 64–68] collaborations. The tau anti-neutrino still has to be observed, de facto being the last missing tile of the SM. The so few so far collected events do not provide sufficient data to measure the ν_τ cross-section.

Most of the studies of electron neutrino interactions are conducted by neutrino oscillation experiments. Therefore, their efforts focus in the few-GeV energy range where the neutrino oscillation effects are more enhanced at the used neutrino baselines. In this energy range quasi elastic processes dominate the neutrino scattering. The latest result in the low energy range have thus been obtained by the MINERνA experiment [69]. At the energies above 20 GeV, data are completely lacking and the lepton universality is assumed for electron neutrino deep inelastic CC cross section.

Neutrinos are also important to study the nucleon strangeness content through charmed hadron production induced by neutrino scattering. Precise knowledge of the strangeness is an important information for many precision tests of the SM: the precise measurement of the W mass itself depends on the knowledge of the strangeness content in the proton [70]. Data used by the PDF groups to estimate the strange see quark content of the nucleon are predominantly given by the NuTeV/CCFR collaboration [71].

In a fixed target facility, with a high intensity and high energy proton beam impinging on a target, a high flux of neutrinos of all flavours can be expected. Therefore, it is ideally suited to perform studies on neutrino and antineutrino physics.

1.3.1 ν_τ cross section

In the final analysis, the DONUT collaboration reported the observation of 9 events with a background of 1.5 [72] but no distinction could be made between ν_τ and $\bar{\nu}_\tau$. Other 5 tau neutrino events were reported so far by the OPERA experiment [64–68] leading to the discovery of $\nu_\mu \rightarrow \nu_\tau$ oscillations in appearance mode with a significance larger than 5σ [50].

With so few detected events, there has been no possibility to make a precise estimation of the tau neutrino and the tau anti-neutrino cross sections.

Due to its inability in disentangling ν_τ from $\bar{\nu}_\tau$, the DONUT experiment quoted an average CC cross section:

$$\sigma_{\nu_l} = \sigma_{\nu_l}^{\text{const}} \cdot E \cdot K(E), \qquad l = e, \mu, \tau \tag{1.9}$$

where:

- $\sigma_{\nu_l}^{const} = (0.39 \pm 0.13 \pm 0.13) \times 10^{-38}$ cm^2 GeV^{-2} and has to be compared with the average ν_μ and $\bar{\nu}_\mu$ cross sections (0.51×10^{-38} cm^2 GeV^{-2})
- K(E) describes the kinematical suppression due to the tau mass

The measurement agrees well with the related muon neutrino charged current (CC) cross section; however, as it can bee seen.

In a charged current deep inelastic scattering (CC-DIS), fig. 1.9, a neutrino with incoming four-momentum k_1 scatters off from a quark (anti-quark) in the nucleon exchanging a $W^\pm$ boson with four-momentum q.

$$\nu_l(k_1) + N(p) \rightarrow l(k_2) + X(p_1)$$

In the laboratory frame, the process is studied by measuring the energy and the direction of the outgoing lepton (E_l, θ_l) and hadrons (E_{had}, θ_{had}).

The Lorentz invariant quantities used to describe a neutrino interactions are:

$$\nu = \frac{p \cdot q}{M} = E_{had}$$

$$Q^2 = -q^2 = -(p - p_1)^2 = -(k_1 - k_2)^2$$

$$x = \frac{Q^2}{2p \cdot q}$$

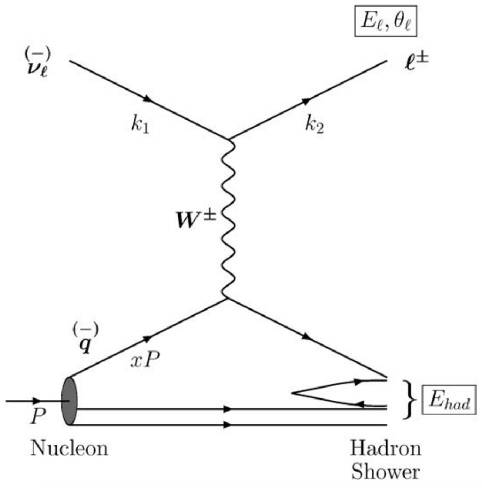

Figure 1.9: Tree-level Feynman diagram for a charged current deep-inelastic neutrino scattering.

$$y = \frac{p \cdot q}{p \cdot k_1}$$
$$W^2 = (p+q)^2$$

where k_2 is the four-momentum of the outgoing lepton, p is the four-momentum of the nucleon while p_1 is the momentum of the final hadron shower.

Using the previous defined variables, the tau neutrino and anti-neutrino DIS cross-section can be written:

$$\begin{aligned}\frac{d^2\sigma^{\nu(\overline{\nu})}}{dxdy} = \frac{G_F^2 M E_\nu}{\pi(1+Q^2/M_W^2)^2}\Bigg\{&\left(y^2 x + \frac{m_\tau^2 y}{2E_\nu M}\right)F_1 + \left[\left(1-\frac{m_\tau^2}{4E_\nu^2}\right)-\left(1+\frac{Mx}{2E_\nu}\right)\right]F_2 \\ &\pm\left[xy\left(1-\frac{y}{2}\right)-\frac{m_\tau^2 y}{4E_\nu M}\right]F_3 + \frac{m_\tau^2(m_\tau^2+Q^2)}{4E_\nu^2 M^2 x}F_4 - \frac{m_\tau^2}{E_\nu M}F_5\Bigg\},\end{aligned} \tag{1.10}$$

where E_ν is the initial neutrino energy and M and m_τ are the mass of the nucleon (average of the proton and neutron mass) and the mass of the τ lepton respectively. F_i ($i = 1 \rightarrow 5$) are called structure functions and depend on both x and Q^2. The positive sign of F_3 applies to neutrino scattering while the negative sign applies to antineutrinos.

As it can be seen in eq. 1.10 both F_4 and F_5 are suppressed by a factor proportional to the square of the charged lepton mass divided by the nucleon mass times neutrino energy, which is negligible for muon and electron neutrinos due to the lower mass value. A precise estimation of the tau neutrino and anti-neutrino cross section would allow a measurement of the structure functions F_4 and F_5 [73] which are negligible in other flavoured neutrino interactions.

At leading order (LO), in the limit of massless quarks and target hadrons:

$$F_4 = 0$$

$$2xF_5 = F_2$$

These are the Albright-Jarlskog relations [73]. On the other hand, at next to leading order (NLO), including full dependence on heavy-quark masses, $F_4 \approx 1\%$ of F_5 [74].

If $F_4 = F_5 = 0$, the ν_τ and $\bar{\nu}_\tau$ charged-current deep-inelastic cross sections would increase as well as the number of expected ν_τ and $\bar{\nu}_\tau$ interactions. In fig.1.10 the expected cross sections for DIS neutrino and antineutrino interactions are presented highlighting the differences between the hypothesis of $F_4 = F_5 = 0$ and the cross section including the full tau mass dependence. The discrepancies enhance at lower neutrino energies: at E = 20 GeV, $\sigma^{CC}_{\nu_\tau}$ with the full m_τ dependence is ~ 30% lower than $\sigma^{CC}_{\nu_\tau}$ obtained neglecting the impact of F_4 and F_5, while at E = 200 GeV, the contribution of F_4 and F_5 reduces the cross sections by about 7%. For $\bar{\nu}_\tau$ the previous described behaviour is even more emphasised being the solid line ~ 53% lower than the dashed line at E = 20 GeV and about 14% lower for 200 GeV.

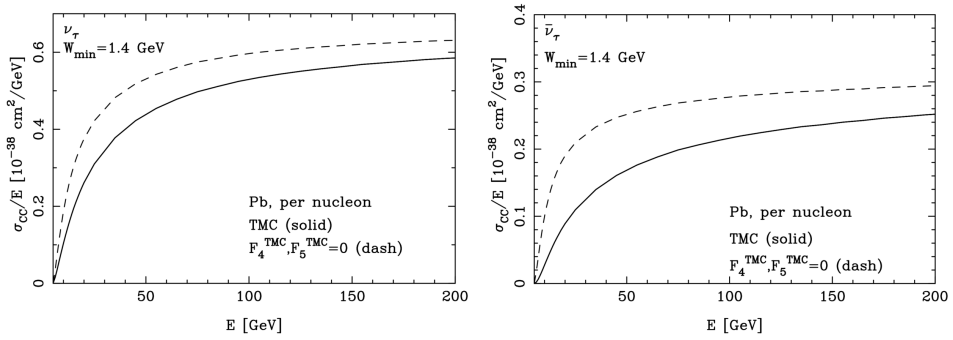

Figure 1.10: ν_τ and $\bar{\nu}_\tau$ CC DIS cross section at both LO (solid curve) and NLO (dashed curve).

1.3.2 ν_τ magnetic moment

In the SM neutrinos can couple to other particles only through weak interactions. Furthermore, there can be loop diagrams where a neutrino transforming into a lepton radiates a W boson which then couples to the produced lepton to give back the initial neutrino. In this case, the intermediate particles can couple to an external electromagnetic field and the neutrino acquires a magnetic moment [75]:

$$\mu_\nu = \frac{3eG_F m_\nu}{8\pi^2\sqrt{2}} \tag{1.11}$$

The presence of a non-zero magnetic moment adds an extra-component to the elastic cross-section for the process $\nu + e^- \rightarrow \nu + e^-$ that in the SM involves only the neutral current. Therefore, an anomalous increment of the measured value of this cross-section can prove the hypothesis of anomalous magnetic moment.

So far, non-zero magnetic moment for ν_μ and ν_e has been excluded down to $\mu_\nu < 6.9 \times 10^{-10} \mu_B$ [76] and to $\mu_\nu < 2.9 \times 10^{-11} \mu_B$ [76] respectively. For ν_τ, the DONUT experiment set the upper limit to $3.9 \times 10^{-7} \mu_B$ [77].

In the elastic scattering of a neutrino on an electron, the scattering angle of the outgoing electron with respect to the direction of the incoming neutrino is limited, in the laboratory frame, by kinematic constraints [78]:

$$\theta^2_{\nu-e} < \frac{2m_e}{E_e}. \tag{1.12}$$

Therefore, for $E_e > 1$ GeV, $\theta_{\nu-e}$ must be below 30 mrad. This can help suppressing the background given by events showing the same topology.

1.3.3 Neutrino induced charm production

Charmed hadrons production in neutrino interactions was observed for the first time in 1974, with the observation of opposite sign dimuons [79].

Nowadays it is known that charmed hadrons are produced at a level of a few percent in high energy neutrino and anti-neutrino charged-current interactions whose Feynman diagrams are reported in fig. 1.11.

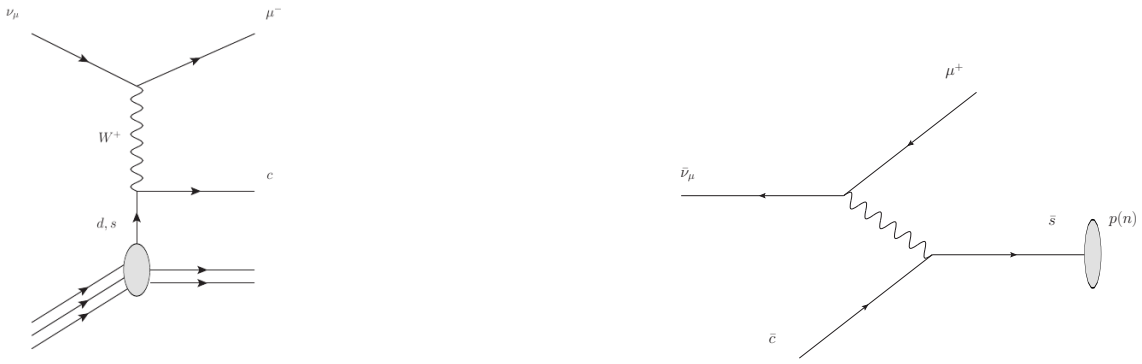

(a) (b)

Figure 1.11: Diagram for charm production in neutrino charged-current interactions (a) and for anti-charm production in anti-neutrino charged current interactions (b).

So far, the identification of charmed hadrons produced in neutrino interactions using calorimetric techniques was based only on the dimuonic decay channel, with two opposite charged muons expected in the final state, requiring also a 5 GeV cut on the minimum momentum to reduce the background from pion decays. This has in fact limited the available statistics to less than 8 thousand charm candidates coming from ν_μ and to less than 2 thousand charm candidates from $\bar{\nu}_\mu$ [80]. No charm candidate from electron neutrino interactions has been observed yet.

Anti-charm production in charged current anti-neutrino interactions selects the anti-strange quark content of the nucleon. The production of a charmed hadron in a neutrino scattering can occur either when the neutrino scatters off a d or a s quark. Even though the CKM coupling favours the $s \to c$ transition, this process is suppressed with respect to the $d \to c$ transition being the d-quark a valence quark. Instead, in anti-neutrino scattering the production of a charm quark occurs through the scattering of the neutrino off a $\overline{d}$ or a $\bar{s}$ quark, which are both sea quarks. Therefore the fraction of ν-induced charmed hadrons coming from a $s \to c$ transition is above 90% in anti-neutrino scattering.

The precise knowledge of nucleon strangeness is critical for Beyond Standard Model Physics at LHC and for many precision tests of the SM. Until now, the strange sea quark determination has been performed by all the PDF groups using the dimuon data collected by the NuTeV/CCFR collaboration [71]: the current status for the proton strangeness $(s + \bar{s})$ is summarised including uncertainty bands in fig. 1.12.

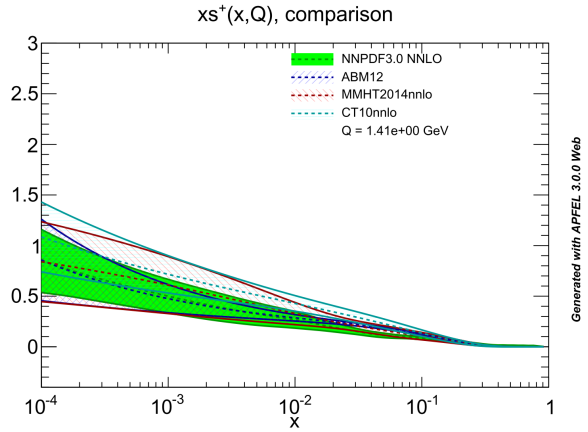

Figure 1.12: Current status for $s + \bar{s}$ distribution in the proton.

A beam dump experiment has indeed the unique possibility not only to explore physics beyond the Standard Model but also to perform accurate studies of SM neutrino physics and QCD measurements.

CHAPTER 2

THE SHiP DUMP FACILITY AT THE SPS

The SHiP (Search for Hidden Particles) experiment is a new general purpose fixed target facility proposed at the CERN Super Proton Synchrotron (SPS) which could provide a unique platform to search for new physics at the Intensity Frontier.

The SPS is a particle accelerator at CERN. With a 7 km circumference, it is the second-largest machine in CERN accelerator complex. Today, it is used as the final injector for high-intensity proton beams for the Large Hadron Collider (LHC), but it also provides proton beams for different fixed-target experiments, such as COMPASS [81], NA61/SHINE [82] and NA62 [83].

SHiP is designed to use protons of the SPS impinging on a beam dump. The project foresees the construction of the SHiP facility at the CERN Prevessin Site, on the North Area of the SPS accelerator complex, in a geographical location that allows a full integration on the CERN land with minor impact on the existing facilities. The proton beam is extracted via the TT20 transfer line, shared with the other North area facilities. In fig. 2.1, the proposed location of the SHiP facility at the CERN Prevessin site is shown in a schematic drawing.

This chapter and the following one present the feasibility studies performed by the SHiP Collaboration, together with a task force of the CERN accelerator sector and the occupational health and safety and environmental protection unit, which have been collected in the Technical Proposal (TP) [84] submitted to the SPS-Committee in April 2015. In particular this chapter focuses on the description of the beam dump facility which is made of a high intensity proton beam from a new extraction line, a high density target, followed by a hadron stopper and a muon shield.

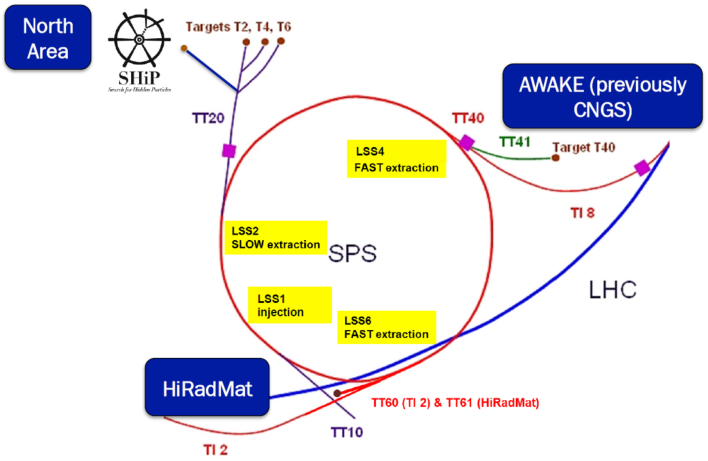

Figure 2.1: SHiP facility location in the North Area at the SPS accelerator complex.

2.1 The Beam

For the SHiP physics program, a 400 GeV/c proton beam is required to be delivered on the SHiP target. Being the weakly coupled particles foreseen in different models beyond the Standard Model mainly produced in the decay of charmed hadrons, the choice of 400 GeV energy protons fits the requirement of a high charm production cross-section.

The beam intensity available for the SHiP cycles is of 4×10^{13} protons extracted in slow extraction mode with a ≈1 second long flat-top every 7.2 seconds in order to reduce background from muon pile-up. While the CERN Neutrinos to Gran Sasso (CNGS) programme [85] has already shown that it is possible to perform two fast extractions (10.5 μs short pulses) per cycle with 50 ms separation of $2.4\times10^{13} p.o.t$, the slow beam extraction represents indeed the main challenge in meeting SHiP requirements. As a matter of fact, the slow-extraction of 4×10^{13} p/cycle is equal to the historical maximum extracted intensity per spill.

The slow extraction is accomplished by first creating a large momentum spread: a set of suitably located extraction sextupoles is used to create a stable area in horizontal phase space of the beam. This initial phase space area is larger than the area occupied by the beam, which is then shrinked by 4 short QMS quadrupoles. Protons with coordinates outside the stable area move away from the beam core along the outward going separatrices, and eventually cross the wires of the ZS electrostatic septa, into its high field region.

The first ZS electrostatic septum was designed and built in the 1970s. It is composed by four identical units, each consisting of two parallel electrodes of 3 m length, mounted in an ultra vacuum tank providing a horizontal electric field. The anode is at ground potential and separates a region without electric field traversed by the beam from the region with the electric field where the protons are deflected in such a way that they can be extracted.

Five ZS units are needed to extract the beam at 400 GeV/c. After the particles have been

deflected, two magnetic septa are used to move the beam into TT20 transfer line. A servo quadrupole is used in combination with a beam current transformer in TT20 to modulate the rate at which the beam is extracted.

Beam losses of the order of 0.5-1% on the wires as the beam is driven across the ZS septa cannot be avoided. They can lead to sparking, vacuum pressure rise, and eventually damage of the wires of the ZS septa through beam heating. To prevent this, additional instrumentation is going to be added along the extraction region to allow fast monitoring and optimisation of the quality of the extraction to minimise the overall losses.

2.1.1 Beam Line Design

Considering the location of the SHiP target, about 600 m of the present TT20 transfer line could be reused, having it a sufficient aperture for the slow-extracted beam at 400 GeV/c.

New laminated and bipolar splitters are needed to switch the beam into a new line while mantaining the existing functionality and splitting the beams to the rest of the North Area for Fixed Target cycles. The new beam line is approximately 360 m in length and will transport and dilute the slow extracted beam onto the SHiP target. The layout of the switch region from TT20 to the new beam line towards the SHiP target is schematically represented in fig. 2.2.

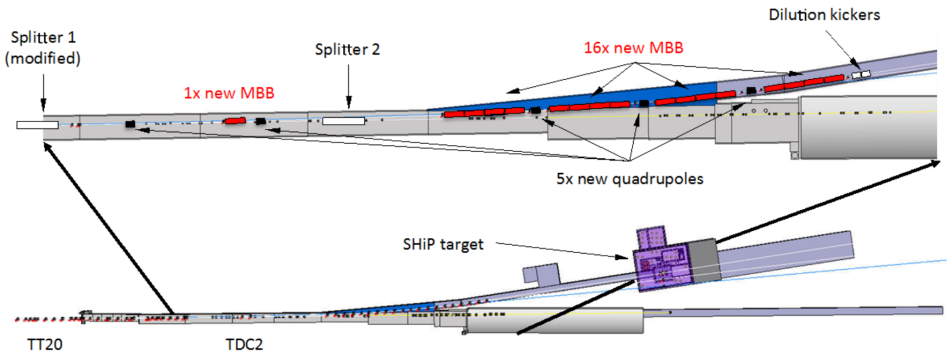

Figure 2.2: Switch region from TT20 to the new beam line towards the SHiP target schematic layout.

The splitter/switch magnet is followed by a set of 17 main dipole magnets deflecting the beam out of TDC2 by 136 mrad towards the Western side via an 86 m long junction cavern into a new 150 m extraction channel towards the target complex for the SHiP secondary beam line. In this way the SHiP facility stays safely clear of the existing installations and the transfer line is as short as possible.

The SHiP beam line is entirely in the horizontal plane. Dispersion and motion induced by momentum variations during the extraction are minimised with the use of bending magnets and

a set of quadrupoles. The 120 m of drift space composing the transfer line is needed to produce a sufficient dilution of the energy deposited in the target.

The beam sweep is implemented with a pair of orthogonal deflection magnets similar to the existing SPS MPLH and MPLV bumper magnets, with a fast Lissajous powering function to produce an Archimedian spiral sweep with constant arm separation and uniform speed. This choice for the peculiar way of diluting the beam is motivated by the power deposition on the target. With a drift of about 120 m and a bending power of 0.25 mrad per plane, it is possible to achieve a sweep radius of up to 30 mm and a total sweep path of more than 600 mm. In order to protect the target and the downstream equipment and detectors, the SPS beam extraction is interlocked on the beam dilution system.

2.1.2 Spill structure and control

Being the SHiP experiment sensitive to combinatorial background, large spikes in the extracted proton rate have an impact on the sensitivity. The maximum transverse proton density could also exceed the maximum value sustainable by the target if the spill shape departs too far from the ideal trapezoid. Therefore, it is very important to control the slow extraction spill quality.

The SPS slow extraction spill is controlled by the servo-spill system [86], which stabilises the beam intensity but cannot correct the 50 Hz harmonics compensated using a feed-forward system. However, the 50 Hz line of the amplitude modulation is expected to be only at the level of a few %. The fixed-target beam spectrum in the SPS has a pronounced structure at the revolution frequency of 43 kHz and its second harmonic of 86 kHz, due to the filling of the SPS from the PS. The time needed for the beam to completely debunch to wash out this structure is much longer than the ~1 s time available for the extraction.

A 200 MHz structure is also present on the proton beam. It is due to the main SPS accelerating RF system and lasts until the debunching and phase space mixing is complete, meaning that the particles with negative offset in one bunch overlap fully with the positive offset particles from adjacent bunches. While in the SPS ring this structure vanishes after some 10 ms, when the slow extraction of the beam is performed it lasts for several 100 ms.

Being the sources of variation on the time structure of the slow extracted spill well understood, it is important to take into account the spill structure while designing the SHiP experiment.

2.2 The Target

2.2.1 Proton Target

The SHiP target is one of the most challenging aspects of the facility because of the high energy and power density that it has to sustain. Considering the SPS operational parameters leading to a high pulse intensity, a cycle averaged beam power on target of 355 kW is expected. Integrating over the spill duration ($\Delta t_{spill} \sim 1$s), the expected beam power is of 2.56 MW.

The choice of materials must take into account not only the high energy deposited and the high temperatures reached, but also the physics that is performed at SHiP. To search for hidden particles mainly coming from heavy mesons, their production must be maximized, while the fraction of neutrinos and muons coming from pion/kaon decays must be reduced as much as possible. These requirements justify the choice of a high A material and with the shortest possible nuclear interaction length for pion and kaon reabsorption from spallation.

Despite a Tungsten target would be an optimal solution satisfying the previous material requirements, it does not sustain the high temperatures reached during the steady state operations. Therefore, a hybrid solution, with a transversal size of 30×30 cm^2 and a longitudinal dimension of 116 cm, was presented:

- 58 cm divided in 13 layers with variable length of TZM ((0.08%)titanium-(0.50%)zirconium-molybdenum alloy) particularly suited for high temperature applications for a total of 4 interaction lengths;
- 58 cm made of 4 blocks of Tungsten, for a total of 6 interaction lengths.

A top view of the target is shown in fig. 2.3.

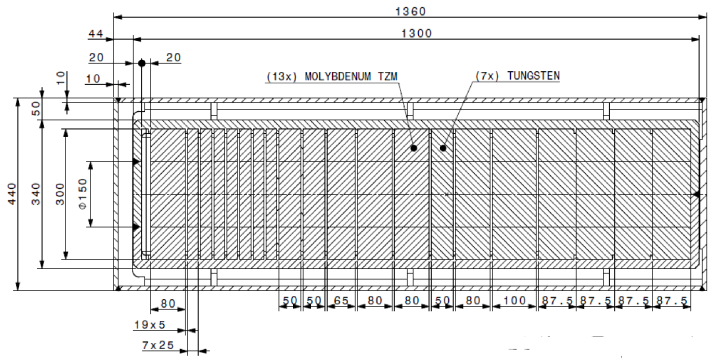

Figure 2.3: Top view of the SHiP target assembly cut at the level of the beam axis.

To evaluate the response of the target, the SPS beam was simulated as a beam of 400 GeV/c with a gaussian shape with a 6 mm sigma. The beam dilution was then reproduced as an Archimedean spiral with a starting radius r_0 of 5 mm and a 6 mm of increment at each turn up to a maximum of 35 mm. FLUKA Monte Carlo simulations [87] [88] have been performed in order to evaluate the energy deposited on the target and the shielding around the target. The longitudinal dimension of the different target blocks has been chosen so to have the most uniform possible energy deposition in each block.

Due to the high energy deposition and to the high temperature reached during steady state operations, active cooling of the target is foreseen: each block is separated by a 5 mm gap, in which water flows. The vessel containing the target and the water system is made of stainless

steel with a wall thickness of 2 cm and is included in a second external containment tank where a closed helium gas circulation ensures a dry and controlled environment (to reduce corrosion) as well as the possibility of monitoring a possible water leak from the internal containment.

Assuming a baseline intensity of 4×10^{13}p/pulse, the energy density averaged around the beam centre is shown in fig. 2.4 as a function of the longitudinal coordinate, while the maximum deposition in the longitudinal direction is shown in fig. 2.5. The maximum energy deposited is approximately 844 J/cm^3/pulse and it occurs at the level of the fourth TZM block.

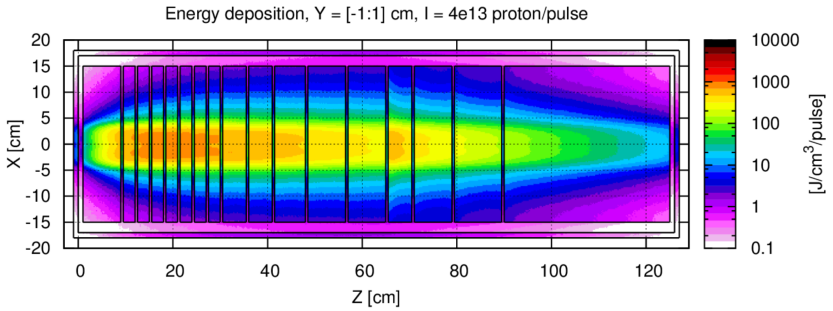

Figure 2.4: Energy density averaged over 2 cm around the beam centre in the horizontal direction versus the target longitudinal position.

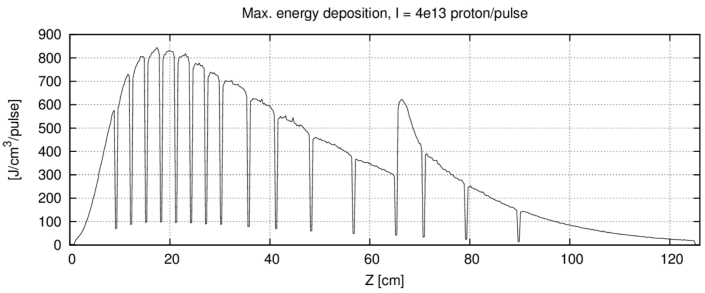

Figure 2.5: Maximum energy density per pulse as a function of the target longitudinal position.

Simulations based on FLUKA have also been employed to evaluate the Displacement per Atom (DPA) as well as the hydrogen and helium gas production, since the latter contribute to the swelling of the target material and therefore in the embrittlement of the material properties. According to the simulation, most of the damage (>0.5 DPA) is concentrated around the beam line in a volume of roughly 1000 cm^3 and the maximum DPA value for 2×10^{20} protons on target is around 0.9 DPA in the TZM section of the SHiP target. The maximum helium gas density produced in the target plates and averaged over the volume of the target plates themselves is less than 430 appm (atomic parts per million) in the TZM region, well below the critical value reported in [89] for (pure) molybdenum of 753.2 appm, while it is of ~353 appm in the W region,

with a critical quoted value of 87.2 appm, requiring therefore further investigation to understand the impact of these values.

Simulations have been conducted also to verify the response of the materials to the oscillating temperature fields on the target generated by the very high energy pulses of the proton beam coming from the SPS and combined with the high cooling rate. The maximum temperature is reached after 5 SPS pulses on target and depends not only on the integral energy deposited per piece but also on its thickness. For TZM, the maximum temperature ranges between 216 and 387°C, while for Tungsten it ranges between 106 and 312°C. Even though these temperatures can be handled by both the materials, they can generate mainly compressive stresses in the inner part of the blocks and tensile stresses on the external surfaces. The compressive stresses oscillate between 185 and 376 MPa for TZM, while the tensile stresses oscillate between 136 and 219 MPa for TZM. For pure W the stresses are ranging between 106 and 312 MPa in compression and 25 and 34 MPa in tension. A dedicated study for the tensile stresses is foreseen for the TDR design because it appears on the surface where the cladding will be applied thus leading to a possible delamination of the cladding material.

The target core is assembled in a double-walled compartment of stainless steel 316LN. A schematic view of the target assembly is presented in fig. 2.6.

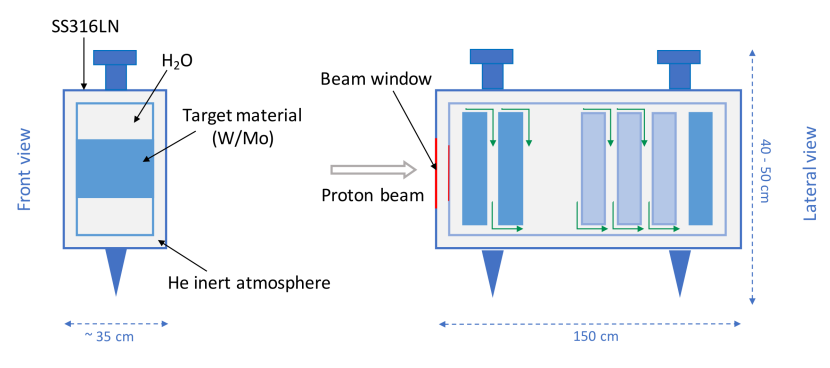

Figure 2.6: Schematic view of the SHiP target assembly.

The external shroud (10 mm thick) contains helium gas at 99% purity that creates an inert environment and avoids the corrosion of the steel parts. Oxygen detectors placed in the He circulation loop help to detect potential leakages from the internal water-containing vessel. The inner shroud (20 mm thick) contains the pressurised water cooling circuit and the TZM and pure W blocks and it is composed by two halves electron beam welded together. The beam window has a round shape of 160 mm diameter: in this way the primary proton beam is not painted onto the electron beam welded part. The inner vessel is build in such a way to withstand the 15-20 bar pressure requested by the cooling circuit in order to increase the water boiling point. It also enforces the high flow water circulation between the target slabs. In view of the TDR submission,

a possibility to use helium for cooling is being investigated.

2.2.2 Target Complex

The SHiP beam dump target will be hosted in a new target complex that will be built in the Prevessin area. The design of the complex is made in such a way that it can be easily re-used by future experiments by exchanging the target and the shielding configuration around the target.

The target hall is designed as a building covering a surface of roughly 30×40 m^2 and approximately 15 m high. It houses the target bunker, the storage zones for both the activated target and the shielding blocks during the interventions, a cooling and a ventilation bunker. It is also designed to contain the first 15 m of the muon sweeper placed immediately downstream of the target bunker. In fig. 2.7 a top view of the SHiP target hall, with a view of the different underground areas foreseen for the operation of the experiment, is presented.

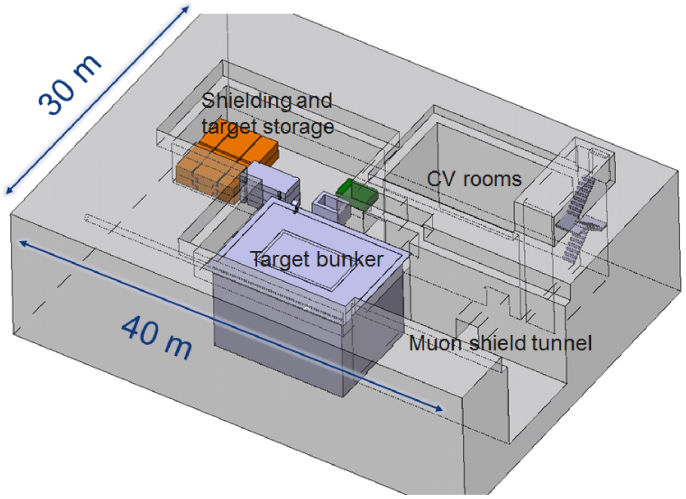

Figure 2.7: Schematic view of the SHiP target complex. A 30×40×15 m^3 building houses the entire complex.

The proton target is located at about 12 m with respect to the surface of the target hall in a shielded bunker.

The target bunker is embedded in a helium vessel containing high purity He gas (>99%) at atmospheric pressure. This secondary helium atmosphere prevents production of high mass isotopes generated by the interaction of secondary neutrons with air and protects the equipment from radiation-accelerated corrosion. A service pit on the top of the vessel allows human interventions on the various feed-throughs and also connects the underground area with the cooling and ventilation equipment to the target bunker.

The target bunker is a compact multi-compartment complex with a floor size of 7.8×10 m^2 at a depth of 11 m to comply with the radiological requirements. It is composed of a massive cast

iron bunker (440 m^3), with an inner core consisting of water-cooled cast iron blocks (*proximity shielding*) with embedded stainless steel water cooling pipes (about 20 m^3).

In order to minimise possible radiation streaming towards the primary beam line, the upstream shielding has only a limited passage for the beam vacuum chamber of about 20 cm diameter. An absorber for neutral particles protects the upstream beam line from neutrons and other neutral particle radiation. A fixed collimator is also foreseen in the first part of the target bunker shielding, in order to protect the fixed cast iron together with the proximity shielding and the target itself against uncontrolled primary beam.

The proximity shielding is made of four cast iron blocks and its total size is $2\times2.6\times4$ m^3, for a total volume of roughly 18 m^3. Each block is equipped with a series of plugin systems in order to pass the water between them. As a matter of fact, the proximity shielding is the most critical element in terms of energy deposition and radiation after the production target, hence needing a water cooling system to remove the heat deposited by secondaries produced in the SHiP proton target. According to FLUKA Monte Carlo simulations evaluating the total energy deposited on the proximity shielding blocks, a cooling capacity of $\approx$ 20 kW is required.

The downstream proximity shielding, 5 m thick, also acts as a hadron stopper. The hadron stopper serves both as an absorber of the remaining hadrons and the non-colliding protons emerging from the target and as a mean to reduce the radiation exposure of the muon shield which separates the target bunker from the experimental hall.

Figure 2.8 shows the design of the four proximity-shielding blocks piled one on top of the other and the SHiP target installed in the centre.

The target bunker is designed to be accessible from the top. As a matter of fact, a removable shielding optimised for radiation protection considerations is placed on top of the water-cooled blocks. The configuration of the blocks is such as to reduce radiation streaming to the top of the target bunker and therefore minimise prompt dose rate on the top of the target hall.

The remaining gap between the shielding and the He-vessel structure is filled by removable concrete blocks.

Another building, adjacent to the target hall, with a surface of 25×15 m^2 is foreseen to host all the other services related to the operation on the target:

- access for the delivery of the heavy equipment;
- personnel access;
- control room for fully remote operation.

This building is also designed to house the radiation protection monitoring control systems, intermediate heat exchangers for the target and shielding cooling unit, the target hall ventilation system as well as ancillary systems such as UPS, control racks for the access and safety systems.

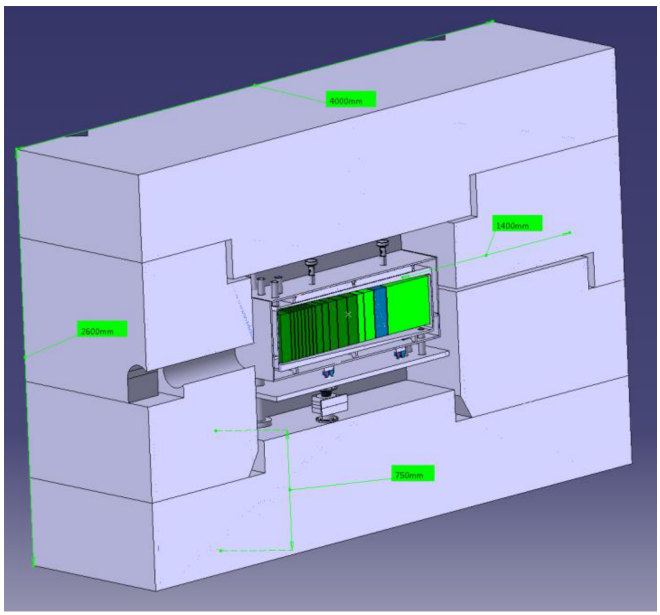

Figure 2.8: Picture showing the four proximity shielding blocks piled one on top of the other with the SHiP target located in the middle. The bottommost block not only supports the SHiP target but it also provides the required services (cooling medium and electrical connections).

2.3 The Muon Shield

In the SHiP beam-dump, the 4×10^{13} protons impinging on the target per each spill produce an order of 10^{11} muons per second coming out, the majority having a momentum above 0.6 GeV/c. In fig. 2.9 the integrated muon flux above a momentum cut as a function of the muon momentum cut is shown. The different contributions to this background muon flux are also reported. Below 40 GeV/c the majority of muons comes from the decay of residual pions and kaons. At higher momenta, the muon flux comes predominantly from resonances.

These muons represent the main source of background to the detection of the hidden particles, hence their flux has to be reduced by several orders of magnitude over the shortest possible distance. The reduction of this type of background is also of great advantage for the neutrino physics program where precise limits on the acceptable muon rates are set from the use of a nuclear emulsion target. To clear a 5 m horizontally wide region, a 48 m long active muon shield based on magnetic deflection of the muons in the horizontal plane is introduced right after the hadron stopper.

To bend out muons with a momentum of 350 GeV/c, a total field of 40 Tm is required. The design of the muon shield of the SHiP experiment is reported in fig. 2.10, while a two-dimensional scheme with the magnets behaviour is shown in fig. 2.11. The different colours in fig. 2.11 represent the different polarisation of the magnetic field: the regular field is depicted in light blue, while the return field is depicted in green.

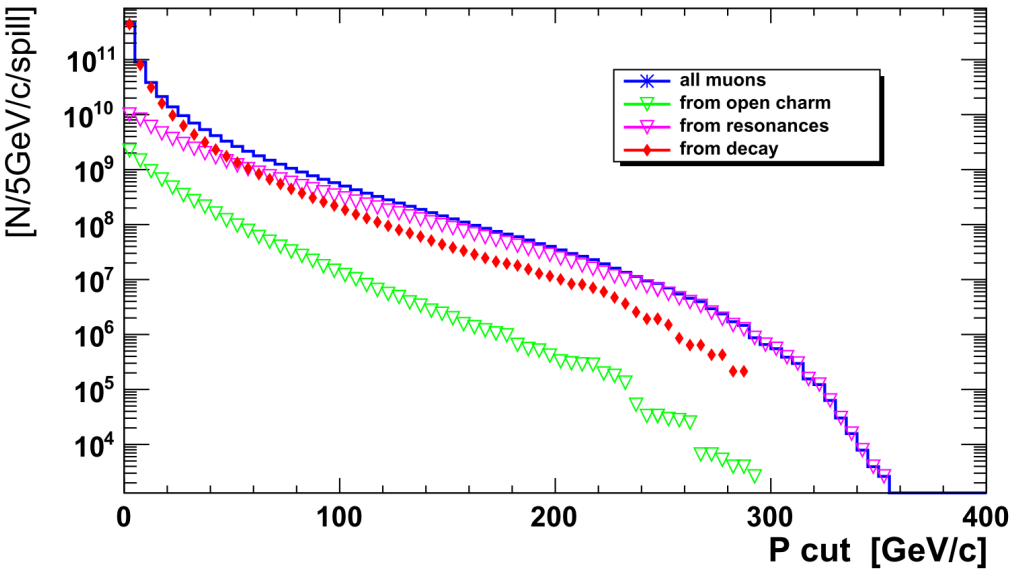

Figure 2.9: Integrated muon flux per spill (in the simulation is 5×10^{13} protons on target) above a momentum cut as a function of the momentum cut .

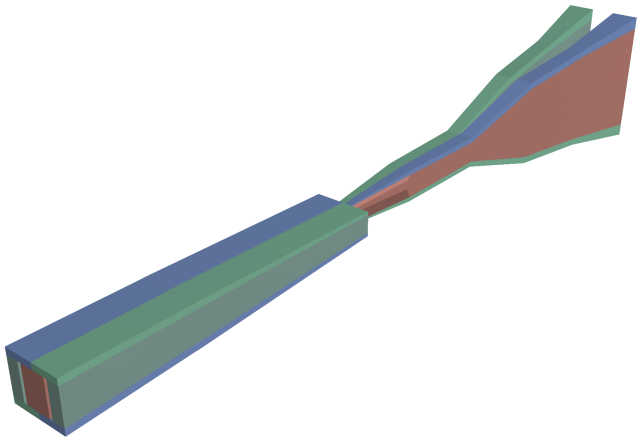

Figure 2.10: Three dimensional view of the active shield. The different colours show the field orientation in the iron.

The first 19 m of the muon shield are used to separate μ^+ and μ^- so that, irrespective of their initial direction, they are bent to two opposite sides: the regular field is close to the z axis, while the return field is placed at x~1.5 m.

In the second region of the muon shield (19 m < z < 48 m), the field polarisation is reversed: the return field is closer to the z axis and the regular field is placed at larger x: in this way the muons that have been bent out in the first part of the shield are bent further outward and are

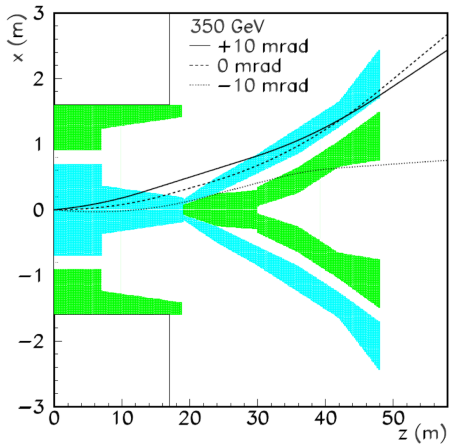

Figure 2.11: The x, z configuration of a possible active muon filter showing the trajectory of three 350GeV muons with a range of initial angles. The blue and dark green show the regions of field and return field respectively. While the muons with initial directions 0 and 10mrad are swept out, the muon with -10mrad will traverse the detector. The field (return-field) is shown in light blue (green).

not sent back towards the detector, as it would happen if a single long sequence of magnets were used. The peculiar shape of the final part of the shield allows to bent out also those particles which have not been deflected in the first part of the shield.

The full three-dimensional GEANT4 simulation of the shield has proved the capability of the muon shield to reduce the muon background in the detector region at the desired level.

CHAPTER 3

THE SHiP EXPERIMENT

The main goal of the SHiP experiment is to search for very weakly interacting particles with masses in the GeV region, within the so called "Hidden Sector" (HS), foreseen in models beyond the Standard Model (SM). These particles may be light sgoldstinos foreseen in the symmetry breaking of the SUSY theory, sterile neutrinos called Heavy Neutral Leptons (HNL) also foreseen in a minimal extension (νMSM [90]) of the SM as heavy (order of GeV) right handed partners of the SM neutrinos and other singlets with respect to the SM. To detect the decay products of these very long-lived particles, a 50 m long decay vessel, placed ~60 m far from the beam dump and equipped with a magnetic spectrometer, calorimeters and muon detectors at the far end is foreseen, as described in section 3.2.

The general layout of the SHiP experiment is illustrated in fig. 3.1 as implemented within the official SHiP software framework (FairShip), described in more detail in section 4.1.

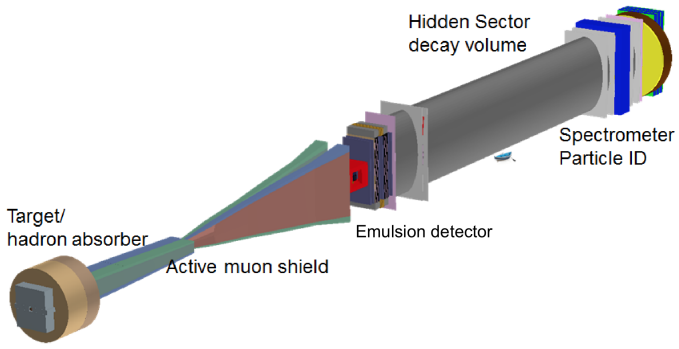

Figure 3.1: Overview of the SHiP facility.

The SHiP experiment can also be considered a neutrino factory, in particular of tau neutrinos, being the 400 GeV beam optimised to enhance the production of charmed mesons and of D_s

mesons too. Hence, SHiP will host a neutrino detector to discover the tau anti-neutrino and to study tau neutrino and anti-neutrino cross-sections. Exploiting the Emulsion Cloud Chamber (ECC) technology [91], this detector will have a micrometric resolution which makes it suitable not only to disentangle the τ lepton production and decay vertices, but also to look for light Dark Matter (DM) particles produced via the decay of the dark photon and scattering off the electrons of the target.

In this chapter, I describe the general layout of the SHiP experiment as presented in the Technical Proposal (TP), mainly focussing on the description of the neutrino detector and its sub-detectors, being the main subject of my Ph.D. activity. Indeed, I have actively taken part in designing this detector and I have also taken care of implementing it in all its details within the FairShip framework.

The still on going optimisation of the detector is instead reported in ch. 5, but the basic idea of the project, i.e. a high density proton target followed by a hadron stopper, a muon shield to reduce muon background, a neutrino detector and a decay volume for detection of HP decays, is left unchanged.

3.1 The neutrino detector

The neutrino detector of the SHiP experiment is designed to perform the first direct observation of the $\bar{\nu}_\tau$ and, thanks to an unprecedented statistics of tau neutrinos and anti-neutrinos, also to study their properties and cross-sections.

It is located immediately after the muon shield in an area which has been cleared from the muon background flux and it is made of an emulsion target, placed in magnetic field and equipped with electronic detectors (Target Trackers), which is followed downstream by a muon magnetic spectrometer. The layout of the detector is shown in fig. 3.2.

3.1.1 The emulsion target

The emulsion target exhibits a modular structure and employs the Emulsion Cloud Chamber (ECC) technology [91], largely exploited by the OPERA experiment, interleaving layers of passive material with emulsion films, acting as tracking devices with micrometric resolution. The micrometric resolution allows not only to disentangle the τ lepton production and decay vertices, but it also makes this detector suitable to look for Light Dark Matter (LDM) particles produced via the decay of the dark photon and scattering off the target electrons.

The fundamental target unit is made of a brick and a Compact Emulsion Spectrometer (CES) (fig. 3.3).

Nuclear Emulsions Nuclear emulsion films are made of AgBr crystals dispersed in a gelatine binder. AgBr crystals are semiconductors with a band-gap of 2.6 eV. The transit of a charged

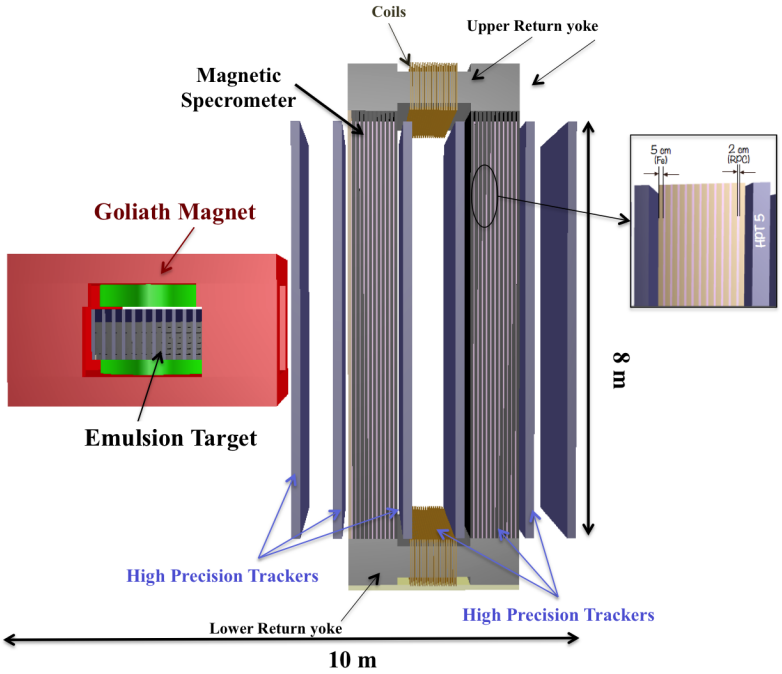

Figure 3.2: Layout of the emulsion detector: the emulsion target is placed inside the Goliath Magnet that provides the 1T field and it is followed downstream by a muon magnetic spectrometer.

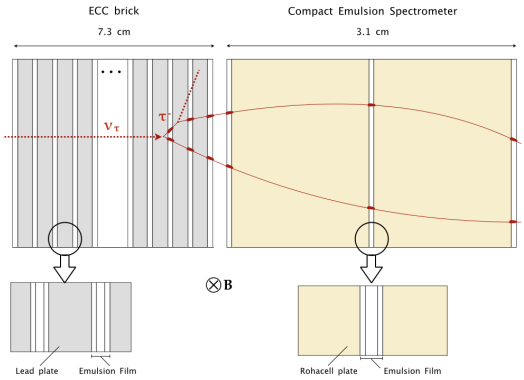

Figure 3.3: Schematic representation of the target unit: the Brick and the CES.

particle creates electron-hole pairs producing Ag metal atoms acting as latent image centres. Through a process called development, the number of silver atoms multiplies and the size of silver grains increases from 0.2 μm to 0.6 μm, becoming visible with an optical microscope. The sensitivity of the film is about 36 grains/100 μm for a minimum ionising particle (MIP).

Each emulsion film is made of two active layers poured on the two sides of a plastic base as shown in fig. 3.4. For the OPERA experiment, the so-called OPERA films were used: 44 μm of gel were poured on a 205 μm thick plastic base, for a total thickness of (293±5) μm and a transverse

size of (124±0.3)×(99±0.2) mm^2. The OPERA films were industrially produced by the Fuji Film [1] company being the total emulsion surface to produce of about 110,000 m^2.

A project for large-scale production of films with improved sensitivity (number of grains produced by a Minimum Ionizing Particle per unit track length) has already started at the University of Nagoya in cooperation with engineers of the Fuji Film company. So far, it has led to a successful production of about 1000 m^2 of films with a sensitivity of 50 grains/100 μm. These newly produced emulsion films are made of 60 μm of gel poured on a 170 μm-thick polystyrene base. In the future this production could be such, that it could cover the needs of the SHiP experiment, ≈8700 m^2 assuming to replace the target every six months along the 5 years of data taking.

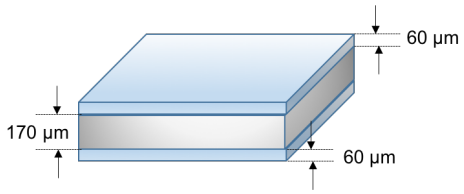

Figure 3.4: Sketch of the transversal section of an emulsion film.

The Brick and the Compact Emulsion Spectrometer The brick is made of 57 emulsion films interleaved with 56 lead plates and it can act as a standalone detector. The lead plates are the high density layers required to maximize the number of neutrino interactions in a compact detector. The emulsion films act as sub-micron resolution trackers. One brick has a transverse section of 128×102 mm^2 and it is 79 mm long (~ 10 radiation lengths) for a total weight of 8.3 kg. The number of radiation lengths not only makes the brick suitable to measure the momenta of the charged particles produced in the neutrino interactions using the deviations they undergo along their trajectories because of the Multiple Coulomb Scattering (MCS) [92, 93], but also guarantees high efficiency in the electron identification through the identification of the induced showers. This latest feature is of great importance also to perform Light Dark Matter (LDM) searches and will thus be object of future optimisation studies. Given the short lifetime of the τ lepton (3×10^{-13} s), in one brick both the neutrino interaction and the τ decay vertices can be identified allowing a full three-dimensional reconstruction of the event. In the SHiP emulsion target, the bricks are arranged in 11 vertical walls, each made of 105 units, as shown in fig.3.5, for a total mass of 9.6 tons. The number of walls has been chosen so to fit the region of uniform magnetic field produced by the magnet hosting the Neutrino Target.

The Compact Emulsion Spectrometer (CES) is made of a sandwich of 1.5 cm of light material (e.g. Rohacell) and emulsion films for a total length of 3.1 cm and it is attached immediately downstream of each ECC brick. The passive material between the emulsion films is carefully

[1] Fuji Photo Film Co., Ltd, Minamiashigara, Kanagawa 250-0193, Japan.

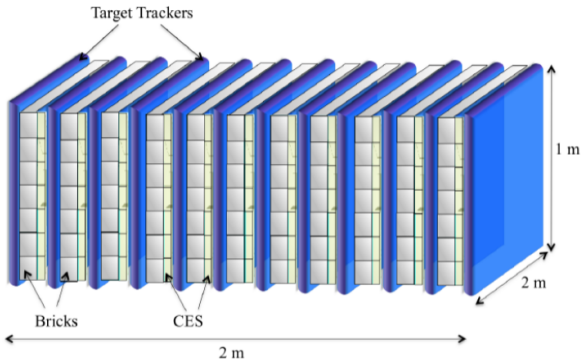

Figure 3.5: Schematic view of the target with the 12 Target Tracker layers.

chosen in order to minimize the effect of multiple coulomb scattering which could otherwise spoil the measurement of the magnetic deflection. The aim of the CES is to measure the electric charge of the hadronic τ daughters which do not reach the magnetic spectrometer downstream hence enabling to distinguish between ν_τ and $\bar{\nu}_\tau$ charged current interactions also in the hadronic τ decay channels. To this purpose, the sagitta method is used. The two-dimensional sagitta s = (s_x, s_y) is the distance between the track position in the middle plate and the intercept in this sheet of the straight line joining the track positions in the two external plates. The x component of the sagitta reflects the curvature due to the magnetic field, while the y component reflects the effects of the multiple coulomb scattering.

A CES prototype made of three emulsion films interleaved with two spacers, each producing an air gap of 15 mm, was tested for the first time in Japan at KEK in 2008 [94]. It was placed in a 1T magnetic field and it was exposed to charged pions of 0.5, 1.0 and 2.0 GeV/c. Results have shown that in this momentum range, the electric charge can be determined with a significance level better than the three standard deviations. A Geant4 simulation well reproducing the sagitta measurements, both for its mean and RMS values, was used to estimate the performances of the CES for $\pi^\pm$ in the 1-15 GeV/c range. The results show that with a magnetic field of 1 T it is possible to measure the electric charge of particles with momenta up to 10 GeV/c. To prevent the emulsion sheets from bending, the CES prototype was designed in such a way that the fiducial area was 4×4 cm^2, less than 15% of the available emulsion surface [94].

The challenge for the SHiP experiment is the design of a detector with a larger sensitive area (close to 100%), while guaranteeing the flatness of the emulsion sheets over their whole surface. The use of Rohacell instead of air as spacer between the films might solve this problem. This solution has been tested and results are reported in chapter 6.

Target Magnetisation The magnet identified to host the emulsion target, thus allowing to perform charge measurements for the hadrons produced in a neutrino interaction, is the Goliath magnet, currently on the H4 beam line inside the PPE134 zone, shown in fig. 3.6.

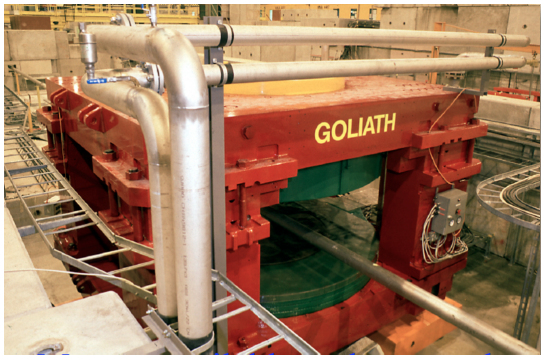

Figure 3.6: Photograph of the Goliath magnet in the H4 room.

Produced in 1976, its overall dimensions are 4.5×3.6×2.8 m^3. Two horizontal parallel coils (the one on the top made of copper and the other one made of aluminium) with a diameter of 2 m are mounted in series at a vertical distance of 1.05 m extendable up to 1.5 m. It exhibits an open window of 2.4 m on two of the four sides, thus allowing to replace target bricks during the run.

The produced magnetic field shows a cylindrical symmetry. The field is approximately constant in a 1 m diameter region, varying up to 30% when approaching the radius of the coils. It then drops rather fast, halving with respect to its maximum value at ≈ 1.2 m from the axis.

I have parametrised its behaviour at different heights (z coordinate) between the two coils thus identifying a region where the field is approximately constant. The results of this study are shown in fig. 3.7 displaying the magnetic field behaviour in the target region. The y coordinate is fixed to 0 so that $r = |x|$ and two regions are identified in terms of z and x. The region within the blue lines defines a volume where the field is approximately constant and equal to 1.5 T. The wider region identified by the red lines defines a volume were the magnetic field is above 1 T. The need for a magnetic field of at least 1 T defines a cylinder of $r = 1$ m and a height of 1 m in which the neutrino detector has to fit.

Target Trackers To provide the time stamp of an event reconstructed in the emulsion bricks and link the muon track reconstructed in the emulsion with the downstream muon spectrometer, electronic detectors are needed. Each brick wall of the emulsion target is interleaved with an electronic detector plane, so-called Target Tracker (TT) plane. In total, 12 TT planes are foreseen, with the most upstream one used as a veto.

These tracking chambers must satisfy very strict requirements: they must cover the whole detector surface (≈ 2 m^2) while keeping a constant distance of a few mm from the bricks so to ensure good planarity and uniform tracking performances. Furthermore, 100 μm position resolution on both coordinates and a high efficiency (>99%) for angles up to 1 rad are required. This request is to ensure an efficient vetoing of background muon tracks. Replacing the emulsion bricks every 6 months leads to the integration in the emulsion films of ~1000 background muon tracks per mm^2 with an average distance of ~30 μm. Assuming a tagging efficiency of 95%, the

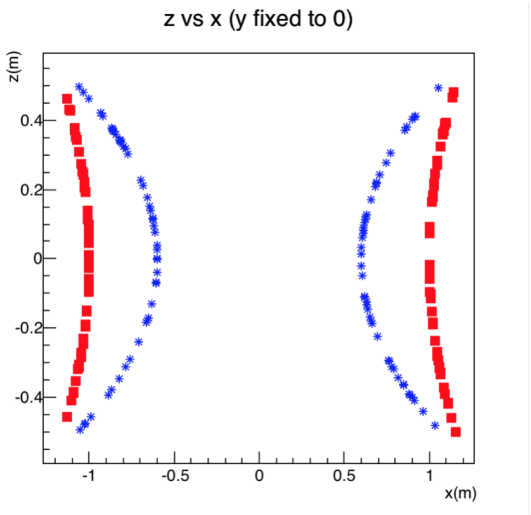

Figure 3.7: Magnetic field behaviour in the target region. Within the blue lines the field is approximately 1.5 T. Within the red lines the field is always above 1 T.

average distance between the untagged tracks is ~150 μm. Therefore it is necessary to have a detector which is able to identify them. An additional advantage of having an electronic detector with a 100 μm position resolution on both coordinates is that it could also allow to associate a V_0 topology (i.e. D_0 decay) to the corresponding neutrino interaction.

Two different technological options under evaluation for this kind of detector: scintillating fibres and micro-pattern gaseous detectors (such as MicroMegas and GEM).

3.1.2 The muon magnetic spectrometer

The muon magnetic spectrometer has the same concept of the OPERA magnetic spectrometer. As shown in fig. 3.8, it is made of 2 arms with opposite 1.5 T magnetic fields and it is also equipped with 6 Drift Tube Tracker (DTT) planes. Each arm is made of 12 iron layers, 5 cm thick, interleaved with 11 Resistive Plate Chamber (RPC) planes, 2 cm thick. The RPCs are used for a course tracking of muons inside the iron, while the measurement of the bending is performed with the more precise DTTs. The main role of the magnetic spectrometer is indeed to identify with high efficiency the muons produced in neutrino interactions and in τ decays and measure their charge and momentum.

One of the advantages of this design is indeed the possibility of producing a high uniform magnetic field which remains contained within the magnetised iron, thus not spreading to external detectors. Moreover, the opposite orientation of the magnetic field in the two arms maximises the acceptance on crossing muons.

The pace of the iron layers is chosen in such a way that there is a high tracking efficiency which, if necessary, allows to measure the momentum of muons stopping within the spectrometer arms and not reaching the DTT planes. The iron thickness is chosen to minimise the effects of

Multiple Coulomb Scattering. For the expected muon momentum range a 15% resolution on the track measured position is achieved satisfying the requirements needed for the SHiP experiment.

The resolution achieved on the measurement of the muon charge and of the muon momentum with a significance of 4σ is:

$$\frac{\Delta p}{p} \simeq \frac{\Delta\theta}{\theta} = \frac{1}{eBd}\sqrt{6\left(\frac{\epsilon p}{a}\right)^2 + \frac{d}{X_0}\left(\frac{13.6MeV}{c}\right)^2} \leq 0.25 \tag{3.1}$$

where: d is the thickness of iron which affects the passage of a particle traversing the whole spectrometer ($d = 24 \times 5\text{cm} = 120$ cm), ϵ is the track resolution ($\epsilon = 200$ μm) and a is the lever arm given by the distance between the two most upstream DTTs ($a = 55$ cm).

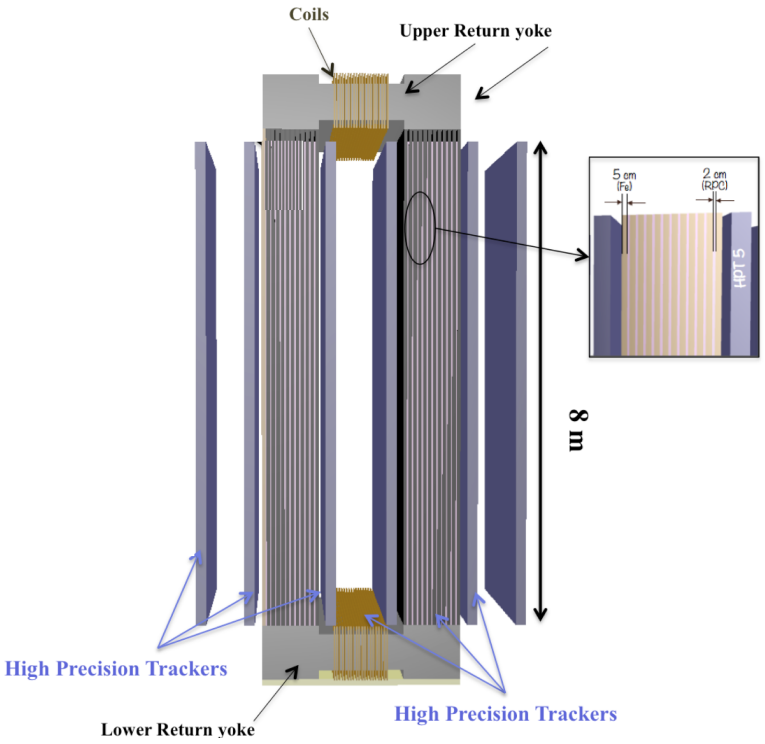

Figure 3.8: Sketch of the muon magnetic spectrometer of the emulsion detector.

The whole spectrometer magnet is 4 m wide and almost 10 m high if both the top and bottom yokes are taken into account. The transverse dimension is chosen in such a way that it is possible to reconstruct muons with an angle up to $\pi/4$ with respect to the incoming neutrino direction. On the other hand, the width is limited from the constraint of remaining in the region cleared from the background muon flux. The averaged 1.5 T field along the walls is produced by means of two coils of 20 turns each in which a current of 1600 A circulates. The non-uniformity of the field along the magnet height is expected to be within 5%.

The RPC system allows to reconstruct tracks inside the magnet. The 1 cm position resolution provided by these detector is enough to perform the coarse tracking between the magnetised iron slabs. A OPERA-like RPC, as I have implemented it in the FairShip framework, is schematically drawn in fig. 3.9: two resistive electrode bakelite plates are separated by two PET spacers with an area of 1 cm^2 and a pace of 10 cm and are painted on the external surface with graphite of high surface resistivity. The gas gap of the RPCs is 2 mm thick. When a charged particle traverses the gas gap, it produces a quenched spark, which induces signals on the read-out strips, typically 3 cm wide and made of copper.

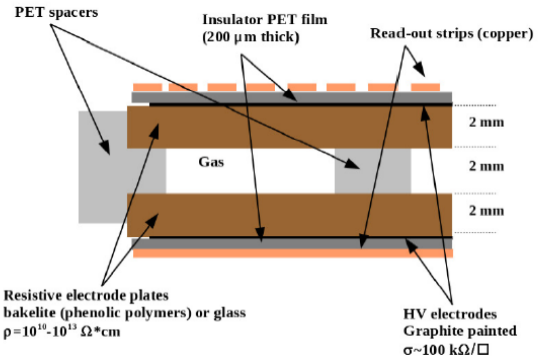

Figure 3.9: Cross-section of a resistive plate chamber used in the OPERA experiment.

I have estimated that the muon flux (see 5.3) at the SHiP RPCs is $\approx$ 4 kHz/m^2. However, there is a strong $e^{\pm}$ component, due to the bremsstrahlung of muons when crossing the upstream muon shield, which raises the rates of particles hitting the RPCs of approximately one order of magnitude.

This sets some requirements on the design of these chambers. One idea could be to re-use OPERA RPC chambers with a resistivity ranging from $5\times10^{11}\Omega$/cm up to $10^{13}\Omega$/cm, but operated in avalanche mode. The use of high resistivity chambers would have as advantage the greater stability, therefore an R&D is ongoing to evaluate the performances of these chambers when operated in avalanche mode and also to define the best electronic read-out. If the feasibility of re-using OPERA RPC chambers is discarded, the construction of new high resistivity OPERA-like chambers will be investigated. Otherwise, another option might be to build new chambers with a lower resistivity, which can more easily tolerate higher rates.

The DDT system has to provide a precise measurement of the charge and momentum of muons emerging from neutrino interactions in the emulsion target. Each DTT plane is made of 48 aluminum tubes staggered in four layers. Each drift-tube is 7926 mm long and has an outer diameter of 38 mm and a 0.85 mm wall thickness. A 45 μm gold-plated tungsten wire in the center serves as sense wire. A spatial resolution of 255 μm can be obtained after the alignment. Instead of the Ar/CO_2 mixture at a ratio of 80/20, used for the OPERA experiment, an Ar/CO2/N2 mixture is foreseen, so to decrease the drift-times, allowing for faster collection times. For a high

precision track reconstruction, the drift times have to be known with a precision of 2 ns. The momentum resolution of the muon spectrometer up to 20 GeV/c is entirely dominated by multiple scattering and taking advantage of the use of the DTT system in the OPERA experiment, it has been measured to be of the order of 20% (eq. 3.1).

3.2 A detector to reveal the Hidden Sector

The Hidden Particles (HP) are produced in the decay of charmed hadrons, hence they exhibit a relatively large opening angle to the beam direction. Since they couple very weakly with SM particles, they also exhibit a long lifetime ($c\tau \sim O(\text{km})$). This implies that their detection requires a long decay volume equipped with detectors at the far end in order to be able to reconstruct their decay products. The different final states that SHiP aims to reconstruct and the different models that can be explored with each of them are reported in table 3.2.

Table 3.1: default

Final states	Models tested
$\pi l, Kl, \rho l (l = e, \mu, \tau)$	ν portal, HNL, SUSY neutralino
$e^+e^-, \mu^+\mu^-$	V, S and A portals, SUSY s-goldstino
$K^+K^-, \pi^+\pi^-$	V, S and A portals, SUSY s-goldstino
$l^+l^-\nu$	HNL, SUSY neutralino

Table 3.2: Different final reconstructable states for the different models that can be explored at SHiP.

Searching for very rare events, one of the main challenges of the SHiP experiment is to be a zero background experiment. The requirements that the detector has to satisfy for the observation of HP are not very strict. What really matters is its capability of tagging and rejecting the possible background sources, such as:

- inelastic interactions of neutrinos produced in the decay of hadrons in both the material upstream of the decay vessel and in the decay vessel itself;
- combinatorial background from residual muons entering the decay volume and muons scattering off the cavern walls;
- inelastic interactions of muons either with nucleons of the concrete cavern walls or for not sufficiently deflected muons by interactions with the material close to the entry of the decay volume;
- cosmic muons entering the decay volume.

To reduce the background due to SM neutrinos to less than one interaction in 5 years, a vacuum of the order of 10^{-6} bar is required and it is achieved by means of turbomolecular pumps with a magnetic levitation of the rotor. To provide efficient protection against particles produced in neutrino interactions in the upstream material, the vessel entrance window is covered by a large array of scintillators detecting with high efficiency any charged particle entering the vessel. In addition, a tracker chamber placed 5 m downstream of the entrance window allows to detect the decay products of neutral particles (e.g. K_{0_L},K_{0_S}) produced in neutrino interaction upstream and which have entered the vessel. Instead, to minimize the combinatorial background, the entire vessel is surrounded by liquid scintillator and right at the exit window, a large array of scintillators form a TOF detector with a resolution of ~ 100 ps to reduce the random coincidences of tracks.

3.2.1 Vacuum vessel and veto system

The layout of the vacuum vessel is depicted in fig. 3.10. It has an elliptical cross section with 10 m vertical and 5 m horizontal inner dimensions, chosen to maximize the geometrical acceptance while still remaining in the region cleared by the background muon flux. To fit to this region, the horizontal diameter of the vacuum vessel has been reduced from 5 m to 3.724 m for the first 5 m length of the vacuum vessel. The overall length of the elliptical tube is 62 m, consisting of 50 m of fiducial decay volume and a 12 m long magnetic spectrometer.

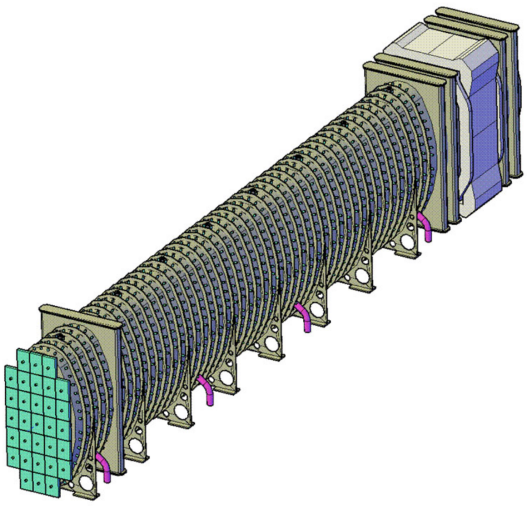

Figure 3.10: Layout of the vacuum vessel.

To withstand an outside pressure of 1 bar, the vacuum vessel has a strong wall ≈ 3 cm thick, with welded transverse and longitudinal reinforcing ribs with a pitch of 1 and 1.5 m respectively.

Five large prismatic volumes to house the tracking detectors cross the vacuum vessel. They all have an elliptical opening of 10×5 m^2 on both sides so that no metal obstructs the SHiP's decay vacuum volume. The first tracking station is located at 5 m distance from the upstream

entrance of the vacuum vessel. It acts as a veto to reject the residual background events from K_0 decays and any other residual charged background in the forward region of the vessel. The other four stations are placed in the downstream magnetic spectrometer region.

The vessel has a double-wall structure: the 30 cm gap inside the double external wall of the decay volume is filled with liquid scintillator, separated into 863 sections of approximately 1.5 m^2 of surface, each read out by two large-area photodetectors. This Surrounding Background Tagger (SBT) not only acts as a veto detector but also offers the possibility to decide offline whether activity in the tracking and calorimeter detectors is produced from particles entering from outside.

The choice of the liquid scintillator as SBT lies in its being very cost-effective and at the same time also highly efficient. As a matter of fact, it can cover very large areas with any given shape and it can perform a real-time detection of charged particles and neutrons starting from a low energy threshold.

To reject neutral kaons produced by neutrino and muon interactions occurring upstream of the vacuum vessel, an upstream veto tagger station located between the emulsion detector and the vacuum vessel is foreseen. The veto tagger station is made of an array of plastic scintillator bars providing very high efficiency, good time resolution, low maintenance and large area coverage. The most crucial parameter is the dead time that this veto introduces, which is proportional to the signal rate (expected to be at most 100 kHz) and the time resolution. Bars 4 m long, with Wave Length Shifter (WLS) fibres and read out at both ends by silicon photomultipliers, can achieve a time resolution below 1 ns, thus resulting in a dead time of $\sim 0.01\%$. In total 120 bars (400 cm long, 12 cm wide and 1 cm thick) are needed to cover the full 4×12 m^2 area.

3.2.2 Detectors to reveal the Hidden Sector

The Spectrometer The spectrometer of the HS has to be able to reconstruct the tracks of charged particles coming from the decay of hidden particles with a high efficiency, providing also an accurate estimation of the particle momentum and of the flight direction in the fiducial volume.

The spectrometer consists of four tracking stations, a dipole magnet and a timing detector. To remove possible combinatorial background it is important that the precision of the extrapolated track position performed with the spectrometer trackers matches the segmentation of the timing detector.

Spectrometer Tracker The layout of the spectrometer tracker foresees four tracking stations placed two upstream and two downstream with respect to the spectrometer magnet.

Each station contains four views: two vertical (Y) and two stereo views (U and V) in the order Y-U-V-Y. The vertical coordinate, Y, is measured using the horizontal elements composing the tracking station, while the X coordinate is measured using the two stereo views rotated of $\pm\theta_{stereo}$.

The stereo angle is chosen taking into account the precision required for the X coordinate since the accuracy of its measurement degrades by $\sim 1/\sin\theta_{stereo}$. For the current design $\theta_{stereo} = 5°$.

The distance between the two stations on the same side of the magnet is 2 m, while the second and the third stations which are placed on the two different sides of the magnet are 5 m apart.

To guarantee good spatial resolution, minimize the contribution from multiple scattering and assure the possibility of working in vacuum conditions the best solution is to use thin polyethylene terephthalate (PET) tubes 5 m long. Each tube has an inner diameter of 9.75 mm and an outer diameter of 9.83 mm.

The layout for one tracker view foresees two planes of two layers each. In each layer the straws are separated along the vertical axis by 17.6 mm corresponding to almost four times the effective radius of the straw where its efficiency is ≈100 %. The second layer is shifted by 26 mm with respect to the first and it is staggered vertically by 4.4 mm.

The overall layout of the spectrometer and the four views in one station are shown in fig. 3.11.

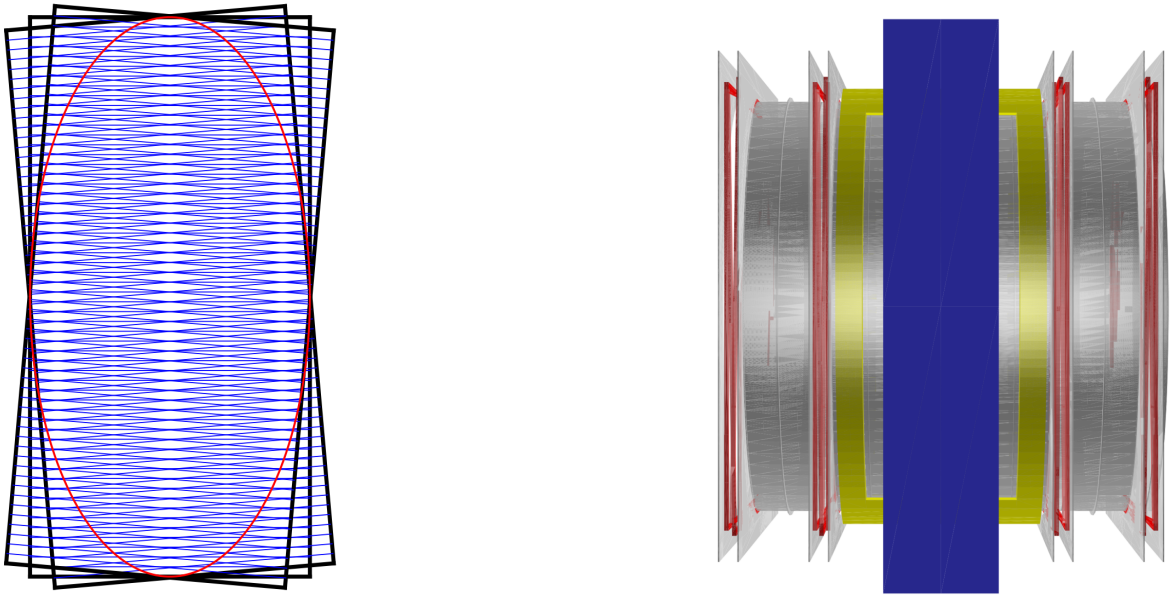

(a) (b)

Figure 3.11: Four views in one strawtube station (a) and the general spectrometer layout (b).

A fifth tracking station, acting as a veto and with only two views, is located a few meters downstream of the vacuum vessel entrance window. As the other stations, it uses drift tubes as technology but its main goal is the reconstruction of tracks originating upstream of the veto station and reaching the spectrometer.

Spectrometer Magnet The spectrometer magnet is a dipole with a free aperture of 5.10×10.35 m^2 with an horizontal field providing a vertical bending plane for the horizontally

oriented straw tracker. As it can be seen in fig. 3.12, it consists of two coils which are surrounded by a window-frame yoke structure and have a shape which guarantees a uniform magnetic field inside the magnet aperture.

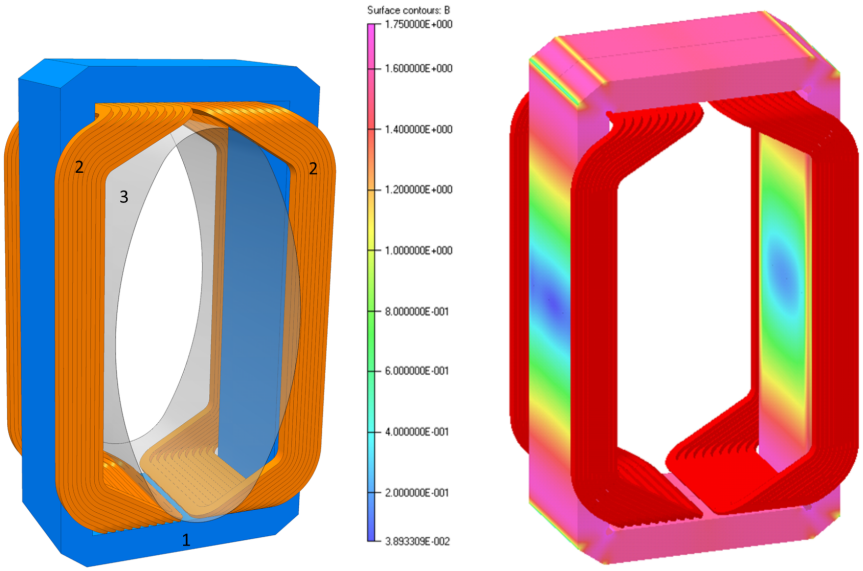

Figure 3.12: 3D schematic view of the magnet (left) and its field amplitude map inside the iron yoke (right).

The maximum field achievable is of 1.5 T and its field amplitude map inside the iron yoke is shown in the right plot of fig. 3.12.

Spectrometer Timing detector It is possible that two random muons enter the vessel and cross the tracker producing a fake signal. To reduce this kind of background a detector reaching a timing resolution of 100 ps or better is needed. Since the other detectors have a time resolution of the order of 1 ns, a dedicated timing detector has to be placed in front of the calorimeter system. There are currently two options under investigation for this timing detector: plastic scintillators and multigap resistive plate chambers (MRPCs).

The design of the spectrometer timing using plastic scintillators is inspired by the layout of forward time-of-flight detector of the NA61/SHINE experiment [82] because it has shown to be capable of reaching 110 ps in time resolution for bars of dimensions $120\times10\times2.5$ cm^3. Improvements in the time resolution can be obtained using different types of plastic and different read-out techniques. The design of the detector array considers two columns of horizontal bars 305 cm long, 11 cm wide and 2 cm thick overlapped by 10 cm. Also the bars are staggered with 1 cm overlap vertically so that inactive regions between adjacent bars are avoided. A total of 240 bars, each of them read at both ends by PMTs, is used covering an area of 72 m^2. The two columns layout is presented in fig. 3.13 (a). Another option with a single bar 6 m long, which

would reduce the number of PMTs by a factor two, is also being considered and it is shown in fig. 3.13 (b).

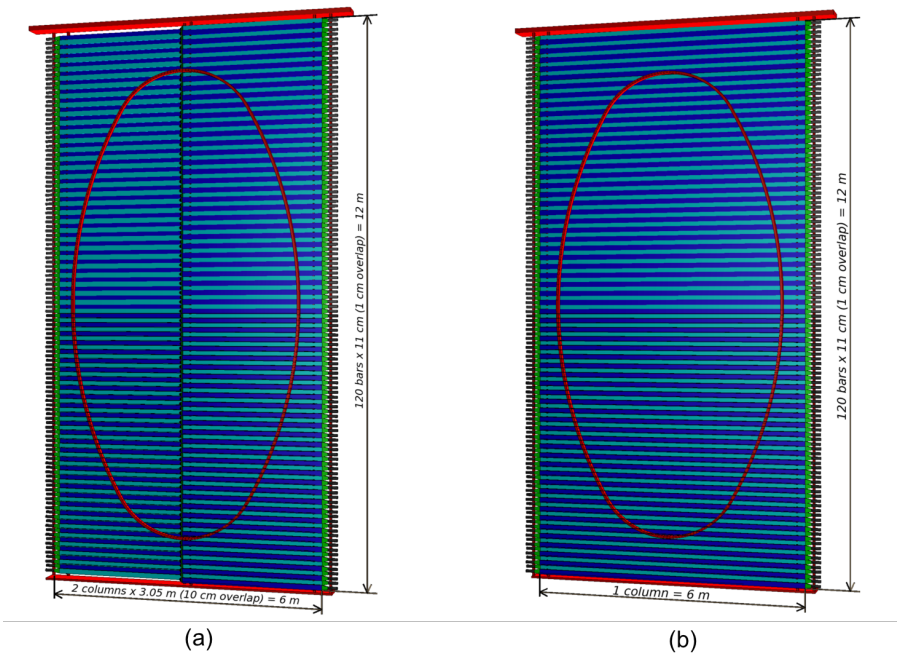

Figure 3.13: Possible layouts of the spectrometer timing detector in the plastic-scintillator bar option with the two-columns setup (left) and the single-column one (right). The red oval line represents the acceptance of the vacuum vessel.

The MRPCs are already used in the time-of-flight detector of ALICE [95] and in the Extreme Energy Events project (EEE) [96] providing in both cases a time resolution better than 100 ps. These chambers are made of stacks of glass plates, separated by commercial nylon fishing lines used as spacers making the gas gaps (see fig. 3.14-a). The outer glass plates are coated with resistive paint, and act as high voltage electrodes, while the inner ones are left electrically floating. Signals induced by charged particles traversing the chamber are induced on segmented readout strips which lie along the x axis: the y coordinate of the incoming particle is therefore obtained directly from the fired strip while the x coordinate is given by the difference of the signal arrival times at the two strip edges. A possible layout of the spectrometer timing detector using the MRPC option is illustrated in fig. 3.14 (b). To cover the whole surface, 61 chambers should be used with a staggered structure to avoid dead regions and inter-calibrate the chambers.

Electromagnetic Calorimeter The Electromagnetic Calorimeter (ECAL) has to perform electron, photon and pion identification, measure the energy of electrons and photons in the range 0.3-70 GeV with a resolution better than 10%, provide π^0 reconstruction in the 0.6-100 GeV range and provide timing information on signals at the ns level for signal-event association and background rejection.

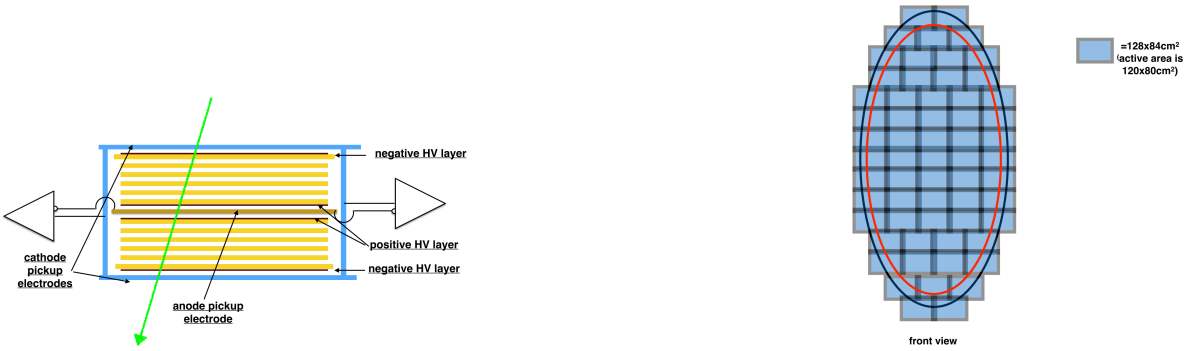

(a) (b)

Figure 3.14: MRPC chamber layout with glass plates in yellow (a) and spectrometer timing detector structure with the MRPCs (b).

The dimensions of the calorimeter system have been decided by studying the acceptance for the decay HNL→ $e^-(\rho^+ \to \pi^+\pi^0)$. Both the π^0 reconstruction efficiency and the electron identification efficiency saturate above the vertical semi-axis size of ~ 500 cm, therefore the ECAL was chosen to have an elliptical shape of 504×1008 cm^2. These dimensions exactly match those of the decay vessel and cover practically the full acceptance of the tracking system.

The shashlik technique, consisting of a sampling scintillator-lead structure read out by plastic WLS fibers, is used, combining good energy resolution, fast response time and relatively low cost-to-performance. Using a sampling structure of 1 mm lead sheets interspersed with 2 mm thick scintillator plates and an accurate design of the light collection by the WLS fibers a resolution on electromagnetic shower energies of $\sigma(E)/E \approx 6\%/\sqrt{E}$ (E in GeV) can be achieved. A photo of a shashlik module is shown in fig. 3.15 (a), while a Geant4 simulation of the module is shown in fig. 3.15 (b). Each module has a transverse dimension of 12×12 cm^2. The complete ECAL structure is represented in fig. 3.15 (c).

Hadronic Calorimeter The Hadronic Calorimeter (HCAL) is necessary to identify pions, discriminating them from muons when the particle momentum is below 5 GeV/c. It also has to tag neutral particles like K_L which are not seen by other detectors and it has to provide timing information on signals at the ns level for signal-event association and background rejection.

The performances of the HCAL depend more on the choice of the active and of the converting material rather than on the technology chosen for it. Up to now, the HCAL makes use of the same technology of the ECAL, it is therefore composed of several sampling modules placed behind ECAL with the same acceptance. Each module is composed by several layers 15 mm thick of converting material alternated with layers 5-mm thick of active material.

The HCAL longitudinal sampling has been optimised using a detailed simulation. It is important to maximize the π/μ discrimination at different momenta while keeping the overall amount of material at a minimum in order not to spoil the π/μ separation performed in the

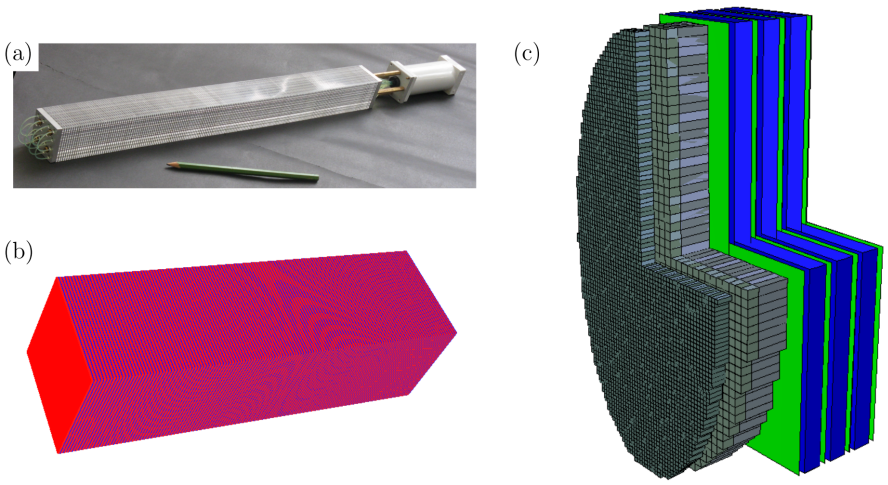

Figure 3.15: (a) Shashlik calorimeter cell, (b) Geant4 view of a shashlik ECAL module, and (c) 5x10 m^2 elliptic electromagnetic calorimeter system and its position with respect to the MUON system.

muon detector. Therefore, the HCAL is made of 1512 single-cell modules of 24×24 cm^2, arranged longitudinally in 2 independently read-out stations. The total length of the HCAL corresponds to ~6.2 λ_I. As for the ECAL, also in this case the light is collected by WLS fibers penetrating from the front and from the rear of each module, bundled together and coupled to the same ECAL photodetectors.

Muon detector In fig. 3.16, the layout of the muon detector can be seen: green thick layers are the passive iron filters, grey thin layers are the active modules. Each active module is defined by two layers (horizontal and vertical) of scintillating bars and the support aluminum structure. The four stations are 6 m wide, 12 m high and are placed downstream of the calorimeter system. The passive iron filters are 60 cm thick walls, corresponding to 3.4 interaction lengths each. To reach the last muon station, the muons must have a momentum of at least 5.3 GeV/c. From simulation studies, it has been seen that a readout granularity of 5-10 cm in the transverse directions is adequate for the interesting momentum range.

The active layers are made of plastic scintillator strips 5(10) cm wide, 3 m long and 2(1) cm thick with WLS fibres and opto-electronic readout. The plastic scintillator technology was chosen because it does not have substantial ageing problems, it has high efficiency and a good time resolution. It also allows simple transverse segmentation, simple and robust construction, potential for distributed production, long-term stability, low maintenance, high reliability and cost effectiveness. In total 3840 strips are foreseen to instrument the entire system in both the x-y view. Therefore 7680 photodetectors are needed to perform the readout at both their ends.

The identification of a charged track provided by the tracking system as a muon or a pion results from a detailed analysis of the hit patterns in the active muon detector and energy

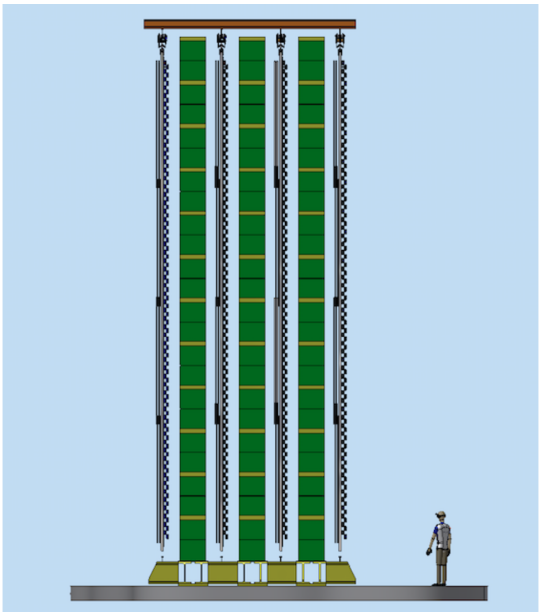

Figure 3.16: Muon detector layout.

deposited in the calorimeters. Charged tracks not releasing any hit in the muon system are tagged as pions. A muon efficiency close to 99% and a pion misidentification probability of < 0.1% can be reached for tracks with p > 3 GeV/c. On the other hand, a pion identification efficiency of ~ 100% can be reached for a muon misidentification probability of ~ 1%.

3.2.3 Selection strategy in the Hidden Sector search

As already pointed out in the introduction of this chapter, the SHiP experiment looks for very rare events. For this reason, the SHiP experiments aims at being a zero background experiment. The goal is to control the background at a level of 0.1 events in the whole data taking ($2 \times 10^{20} p.o.t.$).

The main sources of background are given by cosmic muons and by muons and neutrinos produced in the beam dump or from short-lived resonances, or from the decay of residual pions and kaons or from charmed hadrons decays. Both muons and neutrinos produced at the beam dump can interact with the materials surrounding the decay vessel, thus generating secondary particles which can enter the fiducial volume mimicking signal events. Random combination of tracks from all the previously described background sources must also be taken into account. It is indeed possible that random tracks combine and together fake decay vertices.

The design of the beam line and of the whole detector is done in such a way to reduce these backgrounds as much as possible. Furthermore, several additional cuts on event reconstruction parameters can also be used to further suppress the background.

Simulation studies have been performed within the FairShip (see section 4.1) framework.

The high muon flux originating at the beam dump is efficiently reduced by the use of the active

muon shield. This is extremely important for the neutrino physics program, too. Muons are in this way efficiently swept out by the magnetic field clearing a horizontal region 5 m wide. Simulation studies have shown that, after being swept away, the subsequent interaction of these muons with the cavern walls does not constitute a serious background. To get rid also of muons which are not sufficiently deflected and which hit material close to the entrance of the decay volume, it is sufficient to require two tracks pointing to each other with a *distance-of-closest-approach (DOCA)* < 1 cm and the reconstructed direction of the parent particle pointing to the proton target with an impact parameter IP < 10 cm. Further rejection power can be achieved by requiring no count in the Veto detectors, the Upstream Veto Tagger, the Straw Veto Tagger and the Surrounding Background Tagger.

Background induced by neutrino interactions can be efficiently reduced (about 99.4%) by requiring two high quality reconstructed tracks of opposite charge in the spectrometer, forming a vertex with a DOCA below 30 cm in the decay volume and pointing to the target with IP < 2.5 m.

The muon combinatorial background is reduced by a factor 10^{-7} by setting a time window of 340 ps (about three times the resolution of the timing detector). Another factor of 10^{-4} is suppressed by using information from the upstream veto detectors and the surrounding background tagger.

The cosmic muon background is drastically reduced by requiring to have no hits released in the SBT of the decay volume, together with setting a cut on the DOCA of the two tracks entering the decay vessel of 10 cm and requiring the two-track vertex to be within the fiducial volume, defined by the interior of the vacuum vessel starting from 5 m downstream of the entrance window and up to the first straw tracker station.

3.2.4 Sensitivity to the Hidden Sector particles

The expected signal yield (n) necessary to determine SHiP sensitivities to the different hidden particles can be computed in the following way:

$$n = N(p.o.t) \times r_{prod} \times \mathscr{P}_{vtx} \times \mathscr{A}_{tot} \tag{3.2}$$

where:

- $N(p.o.t)$ is the number of protons on target: in five years operating at nominal conditions, SHiP is expected to collect 2×10^{20} p.o.t. All of them will interact in the target.
- r_{prod} is the production rate of the considered hidden particle per proton-target interaction
- $\mathscr{P}_{vtx}$ is the probability that the decay vertex of the considered hidden particle is located inside the SHiP fiducial volume.

- $\mathscr{A}_{tot}$ is the fraction of the hidden particle decays in the SHiP fiducial volume and producing a detectable final state. It is a function of the branching ratio and of the final state acceptance of the visible decay channels. Conservatively, only decay channels providing two charged particles in the final state are assumed to be detectable. Estimated reconstruction and selection efficiencies are also taken into account.

In fig. 3.17, the sensitivities of SHiP for the HNL search in five years of operation are presented. The five different plots correspond to different scenarios of the νMSM, with different relative strengths of the HNL couplings (U_e^2,U_μ^2,U_τ^2) to the three SM flavours [30, 31, 97]:

1. $U_e^2 : U_\mu^2 : U_\tau^2 \sim 52 : 1 : 1$, inverted hierarchy [97]
2. $U_e^2 : U_\mu^2 : U_\tau^2 \sim 1 : 16 : 3.8$, normal hierarchy [97]
3. $U_e^2 : U_\mu^2 : U_\tau^2 \sim 0.061 : 1 : 4.3$, normal hierarchy [97]
4. $U_e^2 : U_\mu^2 : U_\tau^2 \sim 48 : 1 : 1$, inverted hierarchy [30]
5. $U_e^2 : U_\mu^2 : U_\tau^2 \sim 1 : 11 : 11$, normal hierarchy [30]

The grey region with BAU is ruled out because a HNL with large mass and large coupling could not explain the level of baryon asymmetry in the Universe. The region with low couplings (seesaw) is also excluded because such an HNL would not generate the SM neutrino masses through the seesaw mechanism. Similarly the region on the left of the BBN curve is excluded: an HNL with those parameter could not explain the observations on Big Bang Nucleosynthesis. As it can be inferred from fig. 3.17, the SHiP experiment is able to exceed the sensitivity of previous experiments for the neutrino portal by several orders of magnitude.

In fig. 3.18, the sensitivity of SHiP to the dark photon is presented. The three lines have to be read as exclusion limits at 90% C.L. in case no signal is found. The red line is for dark photons produced in proton bremsstrahlung, while the blue line is for dark photons produced by meson decays; in both cases the sensitivity extends up to ≈ 1 GeV. The sensitivity extends to ~ 10 GeV for dark photons produced in parton-level QCD interactions. As for the HNL case, the grey region represents the parameter region excluded by the constraints from supernovae cooling and Big Bang nucleosynthesis, as well as the constraints coming from previous experiments as of July 2014. The sensitivity goes well beyond existing limits.

Fig. 3.19(a) shows the currently excluded parameter space for a light scalar with Yukawa-like couplings, while fig. 3.19(b) shows the projected exclusion region (together with the current bounds, grey region) achievable by the SHiP experiment. The main production mechanism for light scalars with Yukawa-like couplings at SHiP comes from B-meson and kaon decays. However, the contribution of light scalar from kaon decays is reduced being the experiment designed to absorb kaons in the target before they decay. To define the sensitivity at SHiP, the following S decay modes e^+e^-, $\mu^+\mu^-$,$\pi\pi$ and KK have been considered. The peculiar shape of the exclusion

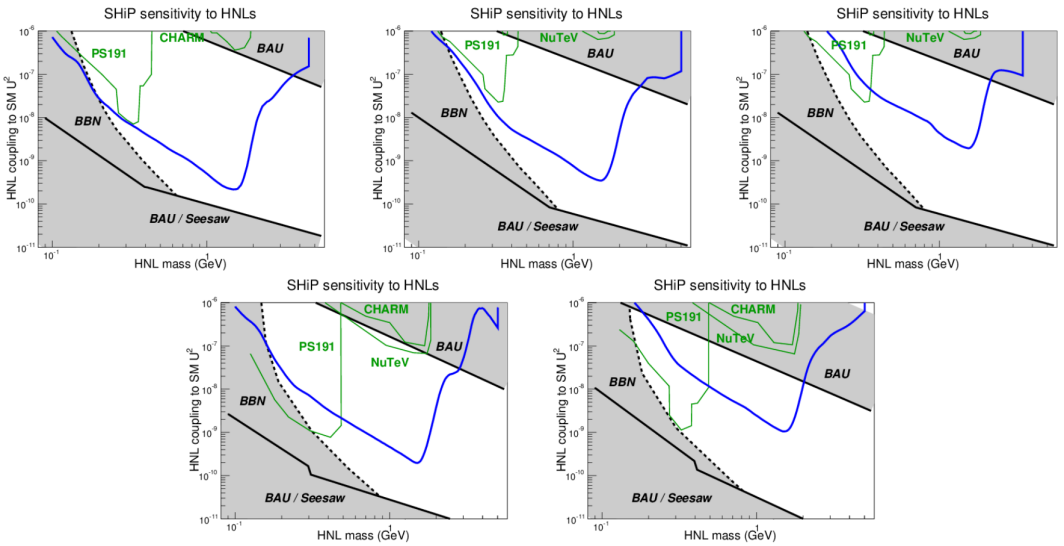

Figure 3.17: Sensitivity contours in the parameter space of the νMSM for scenarios 1-5. They can be interpreted as 90% C.L. exclusion limits if no event will be observed with a level of background of 0.1 events in 5 years, and as 3σ discovery potential if two events would be observed.

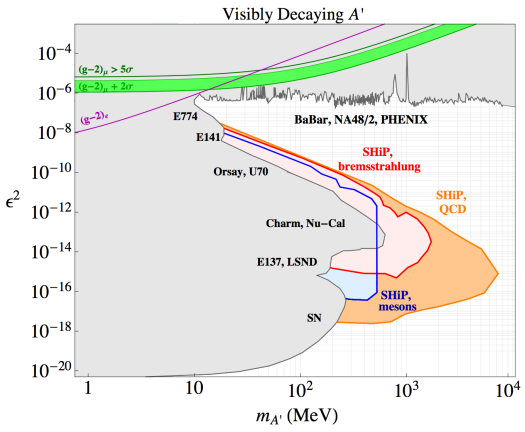

Figure 3.18: Projected SHiP sensitivity to dark photons derived using three modes of production: by meson decays (blue line), proton bremsstrahlung (red line) and parton-level QCD interactions (orange line).

region comes from the requirement that the scalar is detectable if it does not decay too quickly nor too slowly.

3.3 Project schedule

The project time line of the SHiP experiment has been drown up taking into account the operating schedule of the CERN accelerator complex, as well as the technical and financial constraints and

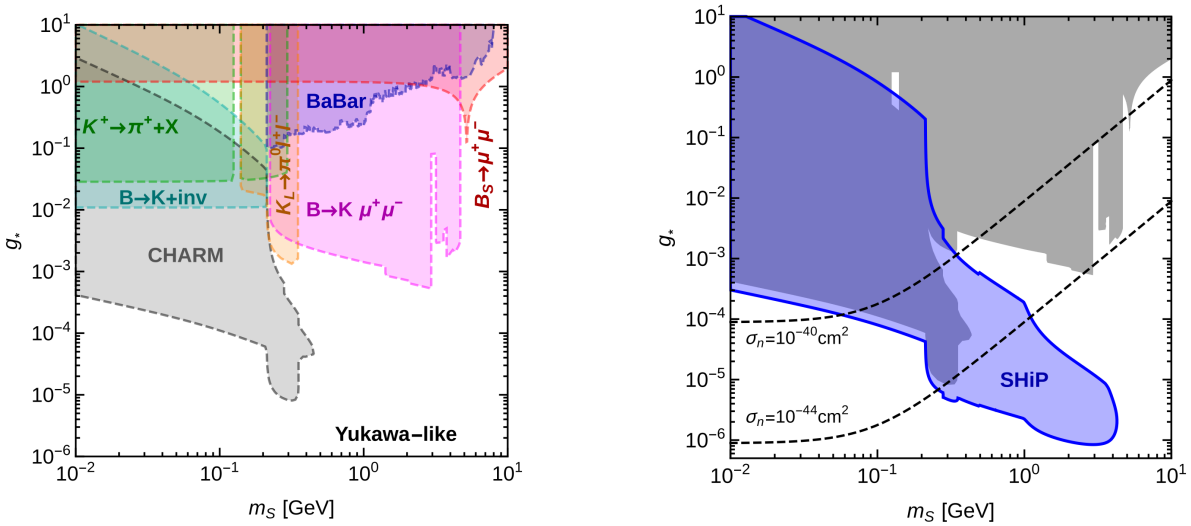

(a) (b)

Figure 3.19: Current constraints on a light scalar particle with Yukawa-like couplings to SM particles (left) and the projected SHiP sensitivity (right).

has been constantly evolving since the submission of the TP in April 2015. The basic idea is in any case that of taking as much advantage as possible of the upcoming Long Shutdowns. The start of data taking at the SHiP facility is planned for 2027, a few months later the start of the LHC high luminosity phase in Run 4.

The schedule with the major milestones to be achieved by the SHiP experiment are reported in the table in fig. 3.20: the Commissioning Design Report (CDR), on the path towards the Technical Design Report (TDR), is foreseen to be completed by 2018, while the TDR has to be prepared by 2019.

Accelerator Schedule	2015	2016	2017	2018	2019	2020	2021	2022	2023	2024	2025	2026	2027
LHC		Run 2			LS2			Run 3			LS3		Run 4
SPS										NA stop	SPS stop		
Detector		R&D, design and prototyping				Production			Installation				
Milestones		TP		CDR	TDR	PRR						CwB	Data taking
Facility			Integration									CwB	
Civil engineering				Pre-construction			Target – Detector hall – Beamline - Junction (WP1)						
Infrastructure								Installation		Installation	Inst		
Beam Line		R&D, design and CDR				Production			Installation				
Target complex		R&D, design and CDR				Production			Installation				
Target		R&D, design and CDR + prototyping						Production		Installation			

Figure 3.20: Project schedule for the SHiP facility and detector.

As it can be inferred by fig. 3.20, the project is mainly driven by the relatively extensive civil engineering required.

The preparation for the civil engineering work will take place during the 21 months of the Long Shutdown 2 with the installation of a splitter/switch and of the SHiP bending magnets as well as of the services and of the sufficient shielding to work downstream when the operations in the North Area resume. The rest of the construction works may be performed during LHC Run 3 with the aim of commissioning with beam (CwB) by 2026 and starting operation of the SHiP facility in 2027.

CHAPTER 4

PHYSICS WITH THE NEUTRINO DETECTOR

4.1 Simulation software

The official SHiP computing framework is made of three packages:

- *FairSoft*: it contains all the packages needed for the installation of FairRoot (ROOT [98], GEANT [99], Pythia [100, 101]);
- *FairRoot*: the FairRoot [102] framework;
- *FairShip*: the proper SHiP simulation framework based on the FairRoot classes.

The complete simulation is done within the FairRoot framework and the detector geometry is implemented using the ROOT package TGEO.

To simulate 400 GeV/c proton interactions on the SHiP target, PYTHIAv8 [100] is used. Then, long-lived particles, like kaons or pions, are given to Geant4 [99] which lets pion/kaon decay or interact in the simulated target material and in the immediately downstream hadron absorber, producing more pion/kaons, and eventually muons and neutrinos. In this phase, the heavy flavour cascade production, which cannot be neglected in a ten interaction length target, is also taken into account [103].

Both the transportation of particles produced in the interaction and the detector response are simulated in the Geant4 framework. The simulation of inelastic neutrino interactions makes use of GENIE [104] and that of inelastic muon interactions make use of PYTHIA6 [101].

For some specific studies on neutrino charged current interactions, the OpNuage [105] generator was used. OpNuage is a standalone NOMAD [106] event generation package, from which also the OPERA event generator "NEGN" was derived [107]. This generator was tuned with a large sample of charged current neutrino interactions from the NOMAD experiment. In

these events the final state had been reconstructed at the level of single particles allowing to tune especially the simulation of the hadronic system including K^0 and other strange particles, which is based on fragmentation parameters and on the inclusion of nuclear re-scattering effects.

I took care of implementing the whole Neutrino Detector geometry, as described in sec. 3.1 within the FairShip framework, also implementing in the software the possibility of placing and propagating in the detector neutrino interactions previously generated with the OpNuage generator.

We now describe the perfomance of the Neutrino Detector as obtained in the conceptual design.

4.2 Estimation of signal yield

Tau neutrinos are copiously produced via $D_s \to \tau\nu_\tau$ and in the subsequent $\tau \to \nu_\tau$ decay.

If $\sigma_{c\bar{c}} = 18.1 \pm 1.7$ μbarn [108] represents the associated charm production per nucleon, while $\sigma_{pN} = 10.7$ mbarn is the hadronic cross-section per nucleon in a Mo target, knowing that the hadronisation fraction in D_s mesons is $f_{D_s} = (8.8 \pm 0.6^{+0.2\ +0.5}_{-0.7\ -0.5})\%$ [109], it is possible to estimate the number of D_s produced in 2×10^{20} proton interactions on the Molybdenum target:

$$N_{D_s^\pm} = 2N_p \frac{\sigma_{c\bar{c}}}{\sigma_{pN}} f_{D_s} \tag{4.1}$$

Here the factor 2, takes into account the production of charm pairs.

Starting from this and knowing that the branching ratio of $D_s \to \tau\nu_\tau$ is $Br(D_s \to \tau) = (5.54 \pm 0.24)\%$ [76], the number of $\nu_\tau + \bar{\nu}_\tau$ produced in the interaction of protons with the Molybdenum target can be estimated as follows:

$$N_{\nu_\tau+\bar{\nu}_\tau} = 2N_{D_s^\pm} Br(D_s \to \tau) = 2.85 \times 10^{-5} N_p = 6.6 \times 10^{15} \tag{4.2}$$

In equation 4.2, the factor 2 is introduced because one ν_τ is produced by the D_s decay and another one by the τ lepton decay. The computed number of $\nu_\tau + \bar{\nu}_\tau$ was used to normalise the simulated Pythia flux at the beam dump. The full kinematics of the D_s decay was included in the simulation. The differences in the kinematics of D_s and τ decays reflects in the different momentum distribution of the produced neutrinos: being the D_S and τ close in mass, ν_τ coming from the meson decay are indeed softer than those coming from the τ decay, as it can be seen in fig. 4.1.

Together with the expected copious production of tau neutrinos, a high rate of ν_e and ν_μ is foreseen. They are induced both from charmed hadrons and from soft pions and kaons decay.

The spectra and the neutrino yield at the beam dump for the three different neutrino flavours are reported in fig. 4.2(a) and in the left column of tab. 4.1, respectively. With respect to the

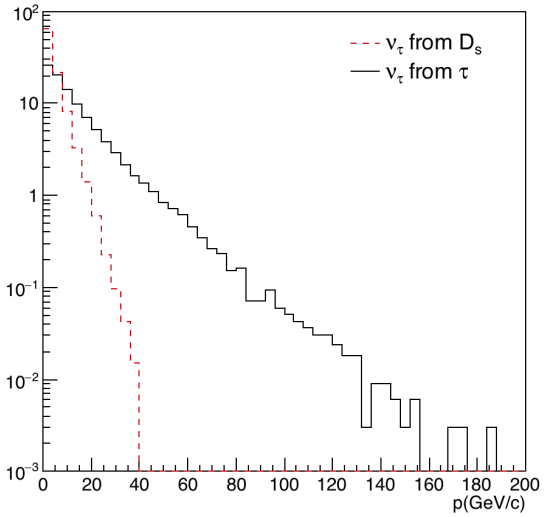

Figure 4.1: Momentum distribution of ν_τ coming from the decay of D_s (red) or from the D_s originated τ lepton (black). The spectrum of D_s originated neutrinos is softer, being different the kinematics of the decay.

Neutrino flavour	< E > GeV	Beam Dump	< E > GeV	Neutrino Detector
ν_μ	1.5	3.4×10^{18}	10.7	4.4×10^{16}
ν_e	4.1	2.2×10^{17}	29.5	5.7×10^{15}
ν_τ	7.4	1.1×10^{16}	22.3	4.7×10^{14}
$\bar{\nu}_\mu$	1.6	2.1×10^{18}	8.6	3.5×10^{16}
$\bar{\nu}_e$	4.7	1.8×10^{17}	21.6	5.2×10^{15}
$\bar{\nu}_\tau$	8.1	1.1×10^{16}	30.7	4.7×10^{14}

Table 4.1: Integrated neutrino yield for 2×10^{20} p.o.t. for the different neutrino flavours at the beam dump (left column) and at the Neutrino Detector (right column).

expected fluxes presented in the TP (see tab. 5.13 in the TP [84]), this simulation also includes the contribution of the heavy flavour cascade production which is not negligible in the ten interaction lengths of the proton target. This leads to gain a factor of about 3 on the tau neutrino fluxes expected by considering only the primary charm production showed in eq. 4.2.

The Neutrino Detector is placed 55.5 m downstream of the proton target. It has a transversal area of ~ 1.4 m^2. Projecting the neutrino flux at the z of the Neutrino Detector, I have estimated that the geometrical acceptance is 1.3% for the total neutrino flux, but increases to 5% for ν_τ and $\bar{\nu}_\tau$ having their fluxes a smaller angular divergence with respect to the fluxes of other neutrino flavours. Spectra and yields are reported in fig. 4.2(b) and in the right column of tab. 4.1, respectively.

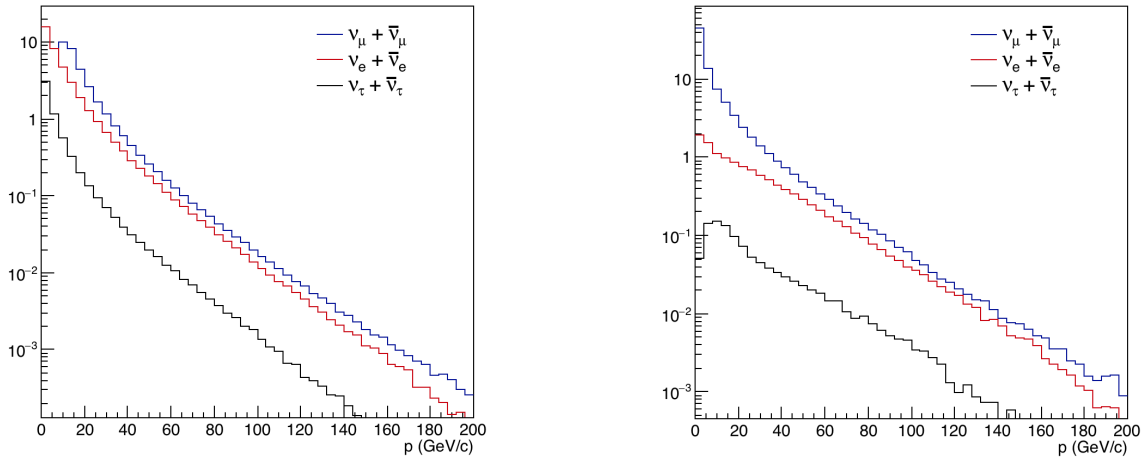

(a) (b)

Figure 4.2: Energy spectra of the three neutrino flavours at the beam dump (a) and at the Neutrino Detector (b). The total number of neutrinos is normalised to 100 and a 0.5 GeV cut is applied.

To estimate the expected yield of neutrino charged current deep inelastic scatterings (CC-DIS), I convoluted the neutrino fluxes at the Neutrino Detector with the CC cross-sections. The CC-DIS cross-section for ν_μ and ν_e is $\sigma_\nu^{CC} = (6.75 \pm 0.09) \times 10^{-39} E(\text{GeV})$ cm^2/nucleon [76], while for $\bar{\nu}_\mu$ and $\bar{\nu}_e$ is one half of the neutrino one ($\sigma_{\bar{\nu}}^{CC} = \sigma_\nu^{CC}/2$). The CC-DIS cross-sections used for ν_τ and $\bar{\nu}_\tau$ is instead represented in fig. 4.3 [74] which however do not include corrections for a non-isoscalar lead target, thus leading to an overestimation of anti-neutrino interactions and, correspondingly, to an underestimation of neutrino ones.

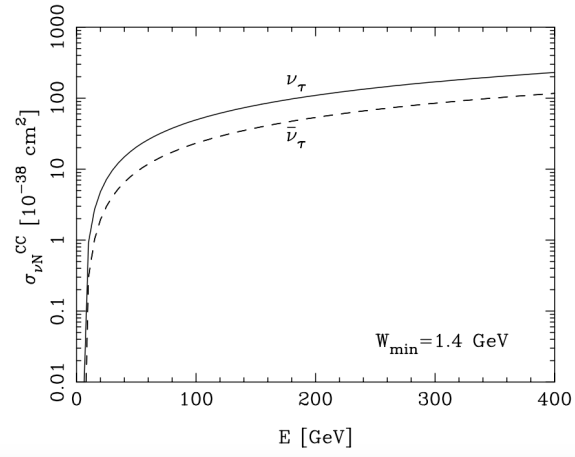

Figure 4.3: Charged-current deep inelastic ν_τ and $\bar{\nu}_\tau$ cross sections [74].

Neutrino flavour	< E > GeV	CC DIS	CC QE
ν_μ	35	1.1×10^6	1.4×10^5
ν_e	54	3.1×10^5	2.2×10^4
ν_τ	47	1.2×10^4	600
$\bar{\nu}_\mu$	29	4.2×10^5	5.5×10^4
$\bar{\nu}_e$	42	1.0×10^5	7.5×10^3
$\bar{\nu}_\tau$	62	8.8×10^3	440

Table 4.2: Expected number of CC-DIS and CC-QE interactions for the different neutrino flavours in 2×10^{20} p.o.t..

The results of the convolution are reported in the CC-DIS labelled column in tab. 4.2 and the corresponding spectra for the different neutrino flavours are shown in fig. 4.4. Muon neutrinos and anti-neutrinos account for almost 78 % of the total CC neutrino interactions, another ~ 21% is due to interactions of $\nu_e + \bar{\nu}_e$ in the target. The fraction of $\nu_\tau + \bar{\nu}_\tau$ interactions represents only 1% of the total. In fig. 4.4 it is interesting to observe how the spectra of interacting muon and electron neutrinos tends to the same value. This can be explained by recalling that, at very high energies, neutrinos come mainly from charmed hadrons decays and the branching fraction of charmed hadrons decaying in ν_μ production is comparable to those decaying in ν_e. The number of Quasi-Elastic (QE) interactions is also reported in the right column of tab. 4.2: they are 13%, 7% and 5% of the number of CC-DIS interactions for ν_μ, for ν_e and ν_τ respectively.

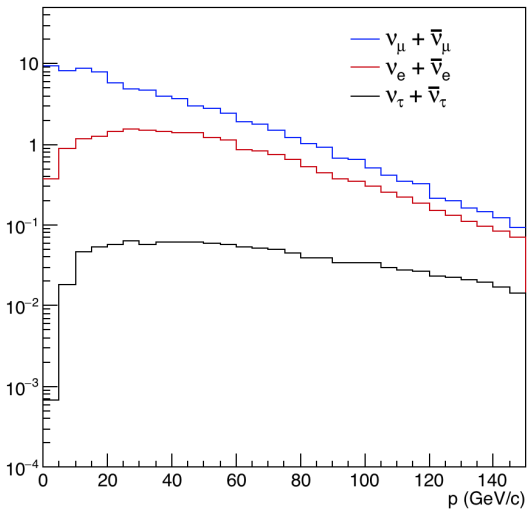

Figure 4.4: Energy spectra of neutrinos produced CC interactions in the Neutrino Detector. The total number of neutrinos is normalized to 100.

Neutrino flavour	$\epsilon_{loc}(\%)$
ν_μ	91 ± 9
ν_e	95 ± 9
ν_τ	80 ± 9

Table 4.3: Location efficiency of a neutrino vertex for the different neutrino flavours.

4.3 Neutrino interaction detection and neutrino flavour identification

Each brick can be considered as a standalone detector. After being developed, all the 57 emulsion films in a brick are analysed and tracks are reconstructed in the whole brick volume.

Once tracks have been reconstructed within one brick of the Neutrino Detector, it is possible to search for neutrino interaction vertices in the brick.

Neutrino interactions are searched for in the brick in a fiducial volume that, in a conservative way, excluded the regions placed at 1 mm from the transverse edges of the brick and the one distant less than 5 mm from the downstream edge of the brick. This results in a geometrical efficiency ϵ_{geom} of approximately 96% in the assumption that the neutrino interactions are uniformly distributed within the volume of the brick.

The location of a neutrino interaction consists of reconstructing the neutrino interaction vertex and its three-dimensional position with micrometric accuracy. To identify a neutrino interaction vertex (I will also refer to it as *primary vertex*), the presence of at least two tracks with a momentum above 1 GeV/c and a slope $\tan\theta < 1$, having an impact parameter (IP) lower than 10 μm, is required. Tracks having an impact parameter larger than 10 μm from the reconstructed neutrino vertex are considered as a hint of the presence of a secondary vertex. I recall that in an emulsion film only charged particles having a momentum $p > 0.1$ GeV/c and a slope in both the $x-z$ and $y-z$ projection below 1 are reconstructed as tracks.

The location efficiency for the different neutrino flavours is reported in table 4.3. The discrepancy between the location efficiencies of ν_μ and ν_e is mainly due to the different momentum spectra of the two neutrino flavours being electron neutrinos on average more energetic than muon neutrinos. Indeed the lower hadronic energy corresponds to a lower multiplicity at the primary neutrino vertex. The lower location efficiency for ν_τ with respect to the other two flavours can be instead explained by the different requirements set for ν_τ identification where the τ lepton track being produced by a short lived particle cannot be used in the vertex reconstruction process.

The identification of the neutrino flavour is performed through the identification of the flavour of the charged lepton produced in the charged current interaction with the passive material of the emulsion cloud chamber (ECC). The lepton flavour identification is also important to classify the daughter tracks produced τ decay, thus identifying the τ decay channel, as well as to identify charmed hadrons induced by neutrino interactions to study the strange quark content of the

nucleon.

Muon neutrinos are identified through the identification of the muon at the primary vertex. The muon identification is performed by the Target Trackers (TT), the Drift Tubes Tracker (DTT) and the Muon Spectrometer (MMS) placed immediately downstream of the Neutrino Detector. A track entering the MMS is classified as muon if:

1. the track must cross at least 3 RPC layers in the first arm of the MMS

2. if the track crosses the Goliath Iron, it must reach at least the first Drift Tube Tracker (DTT) plane.

A muon not entering the MMS can still be properly identified if the track has a momentum smaller than 2 GeV/c and the product of its length in the neutrino target and the density along its path is larger than 300 g/cm^2. Muon identification at the primary vertex is crucial for background rejection. As a matter of fact, the main source of background to all τ decay channels is given by the charged charmed particles (D^+, D_s^+, Λ_c) that have a flight length similar to that of the τ and decay into similar channels. They can be produced both in $\nu_\mu(\bar{\nu}_\mu)$ CC interactions with a muon attached to primary vertex, therefore they do not constitute background unless the primary muon is not identified, and in $\nu_e(\bar{\nu}_e)$ CC interactions with non identified primary lepton.

The identification of the electron neutrinos is performed thanks to the electron identification in the brick, hence searching for particle showers. However, if the electron has not sufficient energy to produce a detectable shower (below 1 GeV) it can still be properly identified by looking at the longitudinal profiles of the angular deviations along the track [110, 111]. In high density material, in the considered energy range, the electron experience a much more relevant energy loss with respect to pions, whose energy remains approximately constant. This originates the differences in the longitudinal profiles. Exploiting the high granularity of the emulsion films we have indeed the possibility to separate electrons from pions, given the different behaviour in the ECC.

Electromagnetic showers can be originated also by photons. Once again, it is possible to distinguish the different origin of the shower by identifying the gamma conversion point. Tracks originated in an electron induced electromagnetic shower converge all towards the electron track that can be followed backward up to the production point. Instead, in a γ induced shower the electron pairs are revealed rather than a single electron track.

The selection of the τ lepton candidates is based on purely topological criteria.

Once the primary neutrino interaction vertex has been defined, possible secondary vertices, sign of possible short lived particle decays, are searched for. This is done by a decay search procedure: tracks are defined as belonging to a secondary vertex if the kink angle and the impact parameter of the daughter track with respect to the primary vertex are larger than 20 mrad and 10 μm respectively.

decay channel	ϵ_{ds} (%)	ϵ_{tot} (%)
$\tau \to \mu$	72 ± 7	60 ± 6
$\tau \to h$	74 ± 7	62 ± 6
$\tau \to 3h$	76 ± 8	63 ± 6
$\tau \to e$	67 ± 7	56 ± 6

Table 4.4: Decay search and overall efficiencies for the different τ decay channels

The decay search efficiency ϵ_{ds} ranges from 67% to 76% for the different channels as it is summarized in tab. 4.4. The electron identification, amounting to $\sim 90\%$, is responsible of the lower efficiency in the $\tau \to e$ decay channel. The total efficiency ϵ_{tot} for the different τ decay channels also reported in tab. 4.4 is the combination of the geometrical acceptance efficiency, of the location efficiency and of the decay search efficiency: $\epsilon_{tot} = \epsilon_{geom} \cdot \epsilon_{loc} \cdot \epsilon_{ds}$ and ranges from 56% in the $\tau \to e$ decay channel up to 63% in the $\tau \to 3h$ decay channel.

4.3.1 Neutrino/anti-neutrino discrimination

To establish if an event was generated from the interaction of a neutrino or of an anti-neutrino, it is necessary to measure the charge of the lepton produced in the charged current interaction.

The muon charge is measured with the MMS. The muon is deflected by the two arms of the magnet with opposite magnetic field direction. Measuring the muon track slopes in the horizontal plane at the entrance and at the exit of the spectrometer arms with the DTT plane, it is possible to determine the charge sign and the momentum of the muon.

To discriminate ν_τ from $\bar{\nu}_\tau$, the charge of the τ lepton decay products is measured.

About 75% of the hadrons produced in the τ decay reaches the Compact Emulsion Spectrometer (CES). There their charge is determined by the track curvature in the magnetic field. The other hadrons either re-interact in the brick, or they are out of the CES geometrical acceptance.

To assess the efficiency in charge reconstruction for both muons and hadrons, a Monte Carlo simulation was performed.

For charge reconstruction in the CES, a smearing of one micrometer was assumed on the track coordinates measured in the emulsion film. Assuming no misalignment between the emulsion films, the first step foresaw the reconstruction of the sagitta in the direction not affected by the effects of the magnetic field, this gave an estimate of the resolution on the sagitta measurement in the direction affected by the magnetic field which was subsequently estimated.

To evaluate the charge of muons using the slopes in the horizontal plane measured by the DTTs at the entrance and at the exit of the two spectrometer arms, no smearing effects were considered since the MCS experienced by the muon track while crossing the arm of the spectrometer had a more important contribution in spoiling the measurement on the slope of the muon than the resolution on the measurement performed by the DTTs.

The efficiencies for correct charge assignment in the $\tau \to h$ and $\tau \to 3h$ decay channels are of 70% and 49% respectively. On the other hand, the charge misidentification probability is 0.5% ($\tau \to h$) and 1.0% ($\tau \to 3h$). The charge identification efficiency in the one prong decay channel is higher since the τ charge is exactly that of the daughter hadron. In the three prong channel, instead, different scenarios can occur:

1. the charge of all the three hadrons is measured;
2. the charge of two hadrons with the same charge is measured;
3. the charge of two hadrons with opposite charge is measured;
4. the charge of only one hadron is measured.

In scenarios 1 and 2 the charge of the τ lepton can be correctly assigned. The same cannot happen for scenarios 3 and 4.

For the $\tau \to \mu$ channel, the muon charge is measured. In this decay channel, the efficiency of correct charge identification is 94% while the misidentification probability is 1.5%.

4.4 Reconstruction of kinematical variables in neutrino scattering

The energy of an interacting neutrino is estimated by reconstructing the energy at the interaction vertex using the charged particles visible in the emulsion films. I recall that a track is reconstructed (visible) in an emulsion film if it is charged, it has a momentum $p > 0.1$ GeV/c and a slope in both the $x-z$ and $y-z$ projection below 1 mrad.

The energy of charged particles propagating in the brick can be estimated by means of the Multiple Coulomb Scattering (MCS), taking advantage of the emulsion ability to measure with extreme precision the particle trajectories [112]. The brick can also be considered as a calorimeter with a radiation length of 10 X_0, thus allowing the reconstruction of the energy of $e^{\pm}$, π_0 and γ from the reconstruction of the generated shower.

I adopt the following naming convention:

- *True energy (E_{true})*: it is the true Monte Carlo (MC) neutrino energy;
- *Visible energy (E_{vis})*: it is the reconstructed neutrino energy accounting only for visible tracks;
- *Reconstructed energy (E_{rec})*: it is the final reconstructed neutrino energy after the calibration between E_{vis} and E_{true}. This allows to take into account possible missing energy at the neutrino interaction vertex, due to the inability to identify neutral particles both at the production and decay vertices.

The neutrino interactions used in the analysis are generated with OpNuage.
I make the following assumptions:

1. The neutrino has a uniform probability of interacting in the brick.
2. The momentum of the hadrons generated in the neutrino interaction is measured through MCS if they interact within the brick, otherwise it is estimated with the CES, for which a 20% of resolution on the measurement is assumed. The resolution on the momentum estimated using MCS has been parameterized in the MC simulation in terms of the momentum p and track span Npl, using the same algorithm used also for the OPERA experiment [112].
3. The probability for a hadron to interact in the brick is 15%.
4. In a first approximation the muon momentum is measured with infinite precision in the Muon Magnetic Spectrometer.
5. The electron energy is estimated with a 20% resolution (see paragraph 4.4.2).
6. The resolution on the photon energy is assumed to be similar to the resolution estimated on the electron energy measurement.

4.4.1 Muon neutrinos

I consider for the analysis only those events in which the neutrino interaction vertex is located: two visible tracks in the final state are required, of which at least one must have a momentum lager than 1 GeV/c.

I first reconstruct the visible neutrino energy as the sum of the measured energies of all the visible tracks and of the photons produced in the interaction and associated to the neutrino interaction vertex.

I then perform a calibration of E_{vis} with E_{true} (see fig. 4.5(a)) in order to recover the missing information on energy of neutral particles that cannot be detected in the emulsion films.

$$E_{vis} = p_0 + p_1 E_{true}$$

In the end I compute the reconstructed energy E_{rec}. The resolution on the reconstructed neutrino energy is evaluated as:

$$\frac{\Delta E}{E} = \frac{E_{true} - E_{rec}}{E_{true}} \tag{4.3}$$

and it is displayed in fig. 4.5(b).

The fractional resolution, $\sigma_{E_{\nu_\mu}}$, is the sigma of the Gaussian fit of the relative difference distribution:

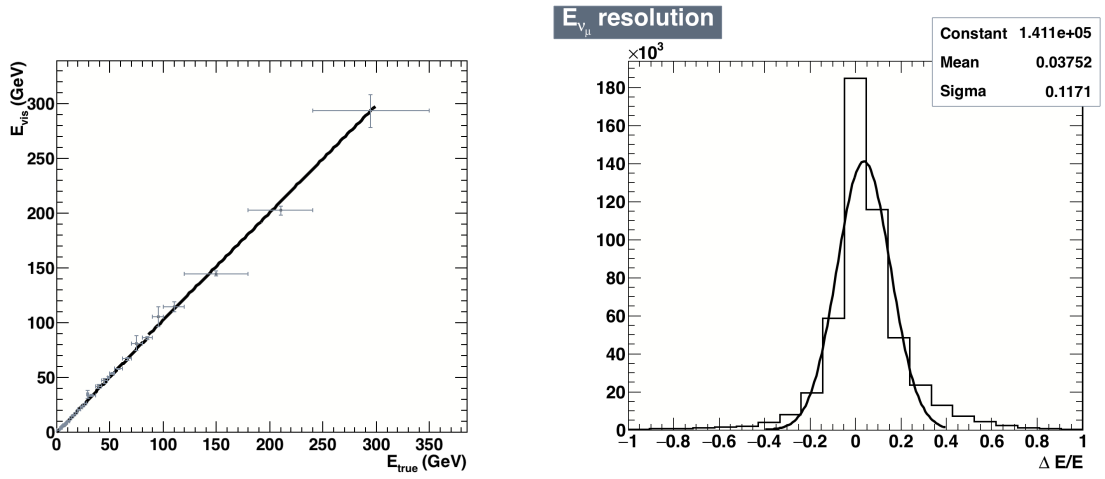

(a) (b)

Figure 4.5: Energy calibration of the visible reconstructed energy as a function of the true MC energy (a) and $\frac{\Delta E}{E}$ distribution (b) for muon neutrinos.

$$\sigma_{E_{\nu_\mu}} = (11.7 \pm 1.2)\%$$

Having assumed the muon momentum to be reconstructed with infinite precision, this value reflects the resolution we expect in the reconstruction of the hadronic energy.

4.4.2 Electron neutrinos

Reconstruction of electron energy The reconstruction of the electron energy is performed using the ECC brick as a calorimeter. The standard shower algorithms used in OPERA [113] cannot be applied straightforward in SHiP. While in the OPERA experiment there was one event per brick, in SHiP, we expect to have on average 233 neutrino interactions (144 ν_μ, 59 $\bar{\nu}_\mu$, 21 ν_e, 8 $\bar{\nu}_e$ and 2 ν_τ and $\bar{\nu}_\tau$ interactions) in 6 months of data taking. With respect to the OPERA case there might be overlapping showers.

To perform this analysis, I used neutrino interactions with lead generated with OpNuage to simulate neutrino interactions in the brick within the FairShip framework: 233 interactions (divided as mentioned above among the different flavours) have been simulated for 15 bricks. In this preliminary analysis, I distributed the interactions in the bricks without accounting for the dependence on the neutrino angle of the energy.

The idea underlying the algorithm is that the electron energy can be reconstructed starting from reconstruction of the associated electromagnetic shower exploiting the relationship between the number of tracks belonging to the electron shower and the electron energy. As it can be seen in fig. 4.6, I open a cone around the primary electron track and I count the number of BaseTracks (BT) selected in the cone.

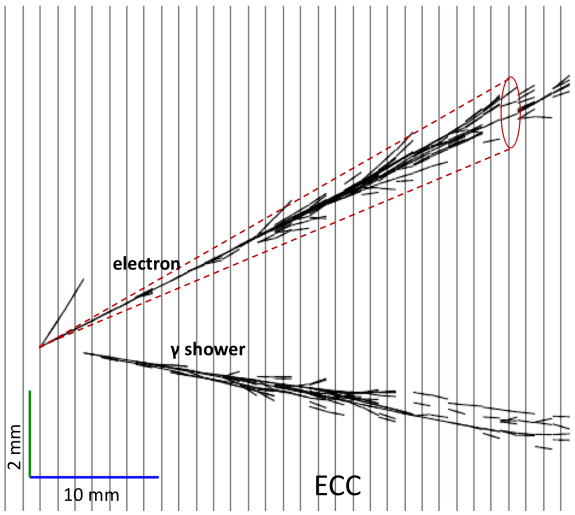

Figure 4.6: Display of a reconstructed electron neutrino event in an OPERA brick. It is clearly visible the difference between the shower originated by a photon and the one originated by an electron.

The main background sources come from physical origin:

- the shower produced by the primary electron in a ν_e interaction overlaps with showers produced by $\pi_0 \rightarrow \gamma\gamma$ either produced in the same interaction or in any other neutrino interaction in the brick;
- passing through muons which I assume to be able to tag with a very high efficiency[1]

I assume that, unlike in OPERA, Compton electrons will be a minor issue due to the short contact with lead.

To estimate the opening angle of the cone, I computed the efficiency and the purity of the track selection for different opening angles. The efficiency is defined as:

$$\epsilon = \frac{\text{number of selected shower tracks}}{\text{total number of shower tracks}}$$

the purity is defined as:

$$P = \frac{\text{number of selected shower tracks}}{\text{total number of selected tracks}}$$

The two curves are shown in fig. 4.7.

I have chosen as opening angle of the cone the one maximizing the estimator constructed as the product of the variables efficiency and purity. The trend of the estimator $\epsilon \cdot P$ is shown in fig. 4.8. The curve has its maximum for an opening angle of 45 mrad.

[1] A passing through track crosses all the 57 emulsion films wich constitute the brick, therefore, even a 10% inefficiency in the reconstruction of base-tracks would still allow to perfectly reconstruct the track of the passing through muon.

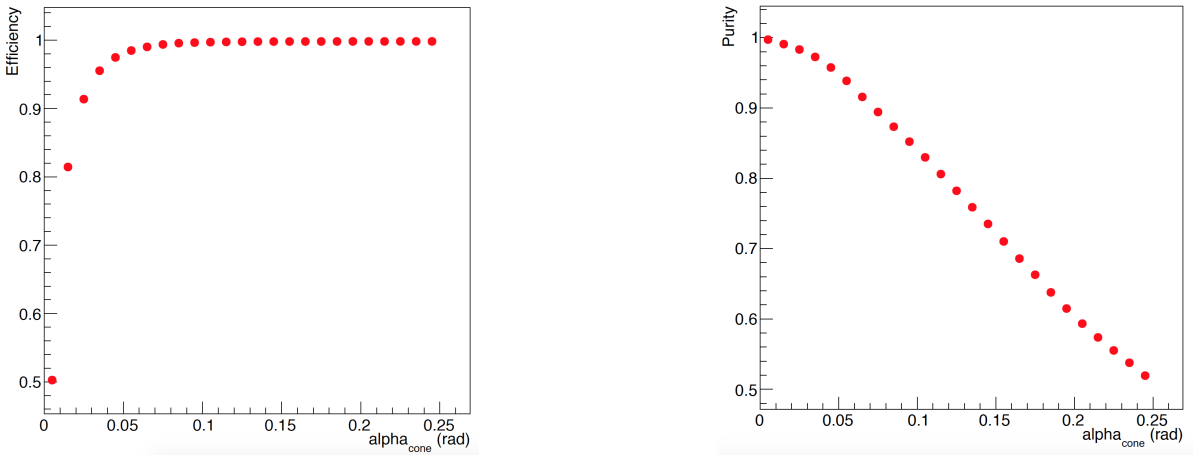

(a) (b)

Figure 4.7: Efficiency (a) and purity (b) as a function of the opening angle of the cone.

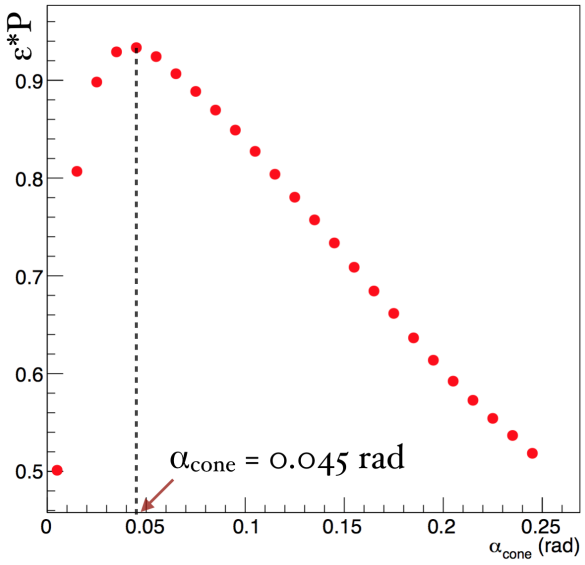

Figure 4.8: Trend of the estimator defined as the product between efficiency and purity as a function of the opening angle of the cone. The angle which maximises this estimator is chosen as opening angle of the cone.

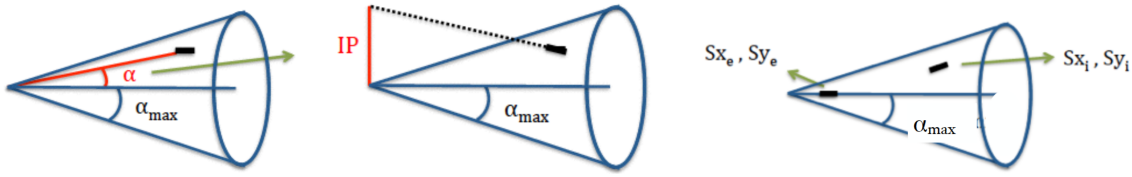

(a) (b) (c)

Figure 4.9: Definition of the variables used to discriminate signal from background tracks: α in (a), the impact parameter in (b) and the angular difference of base-tracks with respect to the first BT of the electron ($\Delta S_{x,y}$) in (c).

Having fixed the opening angle of the cone, I have selected all the tracks entering the cone. To discriminate between signal and background tracks I have used the following variables:

1. *α angle for each BT*: the BT angle with respect to the axis of the cone, computed by connecting the BT position with the cone vertex and subtracting the electron axes (see fig. 4.9(a));

2. *Impact parameter*: it is defined as the distance between the vertex position and the projection of each BT on the vertex plane (fig. 4.9(b));

Other variables that can be used to discriminate signal and background are the angular difference between the slope of each base-track inside the cone (S_{x_i},S_{y_i}) and the slope of the first base-track of electron (S_{x_e},S_{y_e}) for both the X and the Y projection (fig. 4.9(c)):

$$\Delta S_x = S_{x_i} - S_{x_e} \qquad \Delta S_y = S_{y_i} - S_{y_e}$$

To better separate background from signal tracks selected in the cone, I applied the Boosted Decision Tree (BDT) method. This multivariate analysis method uses an algorithm based on a decision tree to determine the best cut values for the different variables. However, not only one decision tree is used, but a "forest" of decision trees (this is why "Boosted" Decision Tree).

The starting sample is divided into training and testing samples. Data taken from the training sample are split by rectangular cuts in *nodes*. For each node, the split is defined by assessing the cut values that for each variable give the best signal (S) / background (B) separation. The final node, called *leaf*, contains events categorised either as signal-like or background-like according to a purity threshold set to 0.5. All misclassified events are then re-weighted and a new decision tree is created to improve the S/B separation. After the training, the BDT is applied to the testing sample. The output is a variable called *BDT response* which can range from -1, which defines the background-like events, up to +1, that defines the signal-like events.

The normalised distributions of the BDT input variables in blue for signal and in red for background tracks are shown in 4.10 and consider only the events from the training sample,which consists of half the background and half the signal sample. The correlation between these

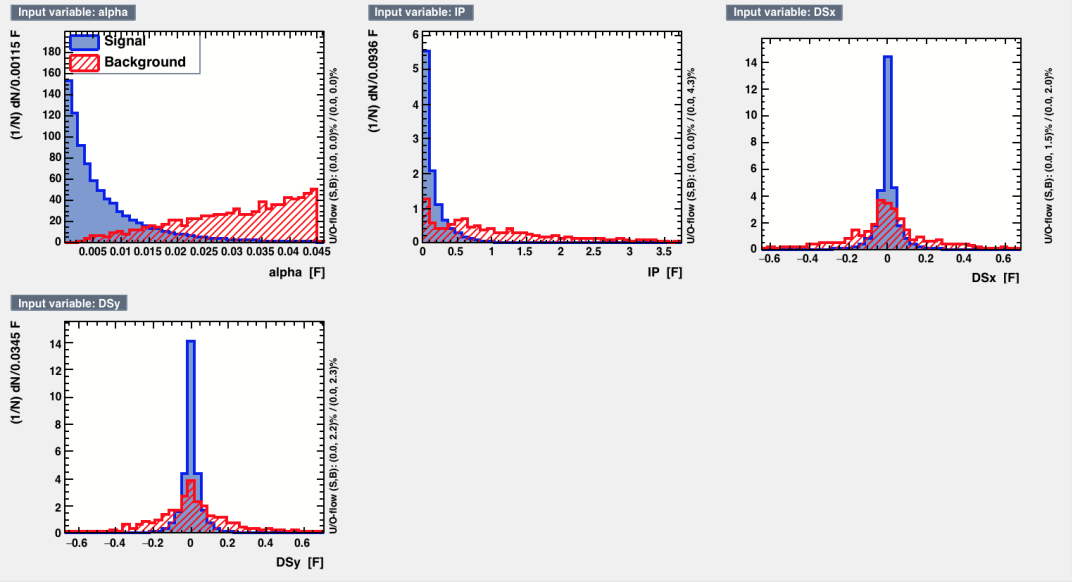

Figure 4.10: Normalised distribution of BDT input variables. Signal distribution is shown in blue and background distribution in red; Top Left: Alpha distribution, TopMiddle: Impact Parameter distribution, Top Right: Angular difference in X projection, Bottom Left: Angular difference in Y projection

variables, which is ideally required to be null, is low, as shown in fig. 4.11(a) for signal and in fig. 4.11(b) for background.

The cut efficiency and the optimal cut value obtained after having applied the BDT method are reported in fig: 4.12. I decided to select as signal tracks only those giving a BDT response larger than 0.2. In this way I reject almost all background tracks while maintaining a signal selection efficiency of ~ 70%.

The number of base-tracks produced in an electromagnetic shower depends not only on electron energy but also on the position of the neutrino interaction vertex inside the brick. The closer the event is to the brick edge the less number of BT of the shower is contained in the brick. To be conservative, I have considered only those events with the ν_e interaction plate in the 26 upstream films in the brick which selects $\approx 42\%$ of the ν_e event sample. For those events the shower originating from the electron is rather well contained in the brick.

The calibration between the number of tracks considered as signal tracks in the cone and the MC true electron energy is shown in 4.13(a). The resolution on the reconstructed electron energy is displayed in 4.13(b) and it is:

$$\sigma_{E_e} = (18.2 \pm 1.8)\%$$

Reconstruction of electron neutrino energy To estimate the resolution on the electron neutrino energy, I applied the same procedure as the one already outlined for the reconstruction

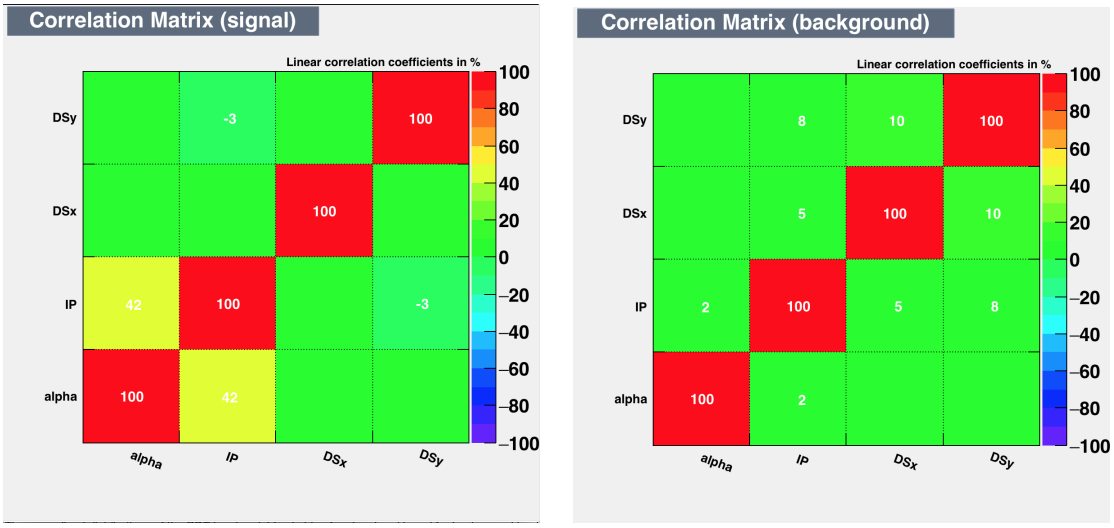

(a) (b)

Figure 4.11: Correlation matrix for signal (left) and for background (right).

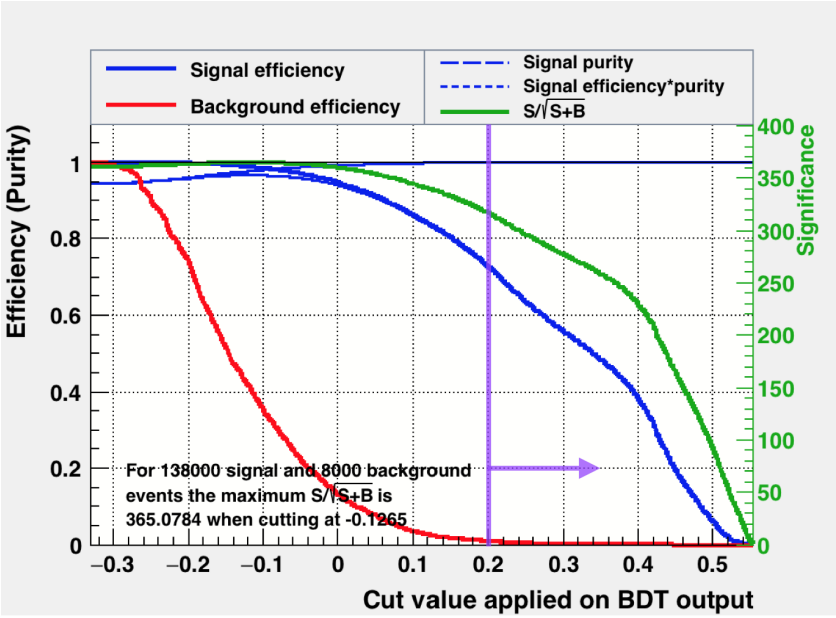

Figure 4.12: Cut efficiencies and optimal cut value obtained with the BDT method. Tracks with a BDT response larger than 0.2 are selected as signal tracks.

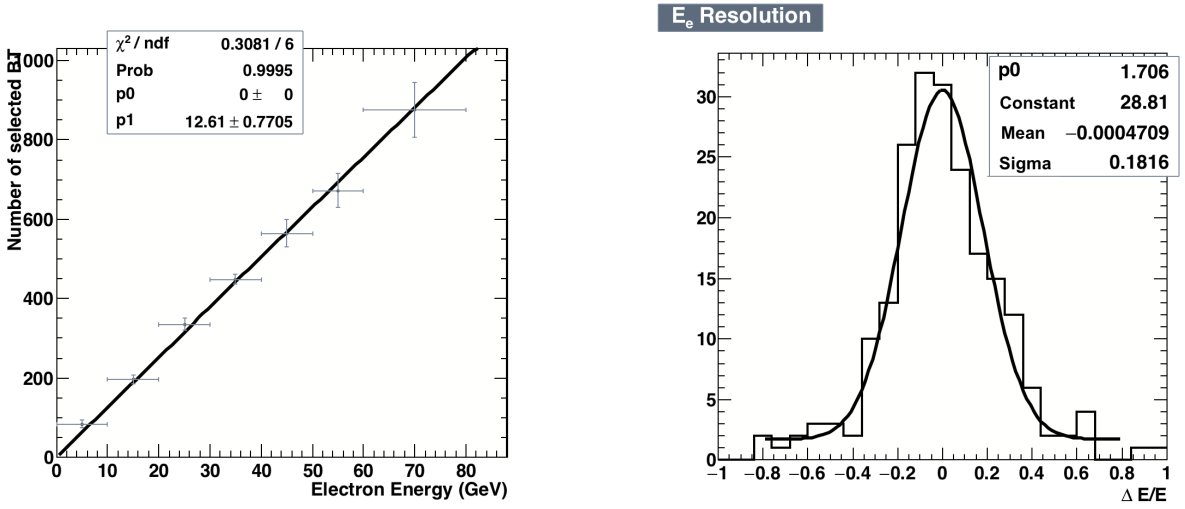

(a) (b)

Figure 4.13: Calibration of the energy as a function of the number of base-tracks (a) and $\Delta E/E$ distribution for electrons (b).

of the muon neutrino energy (calibration between visible and true MC energy is shown in fig. 4.14(a)). The fractional resolution, $\sigma_{E_{\nu_e}}$, given by the σ of the gaussian fit shown in fig. 4.14(b) is:

$$\sigma_{E_{\nu_e}} = (17.1 \pm 1.7)\%$$

In this case, the resolution on the neutrino energy is compatible within errors to the resolution on the electron energy.

4.4.3 Tau neutrinos

Reconstruction of τ lepton energy The τ lepton is identified by disentangling its production and decay vertices. Due to its short lifetime, its energy must be reconstructed starting from its daughter.

For the lepton number conservation, the decay of a τ results in the production of at least one (invisible) neutrino. However, the kinematics of the decay can still be closed if there is only one neutral undetected particle.

A pure one prong decay, i.e. with no emitted neutral particles at the decay vertex, represents 11.5% of the total τ decay probabilities, while the pure three prong decay represents 9.8% of the total branching fractions. In all the other cases, at least one neutral particle is emitted.

When the τ lepton decays into a muon or into an electron, two neutrinos are emitted: these leptonic decay modes have thus been excluded from the following analysis. They account for ~ 35% of the total tau decays.

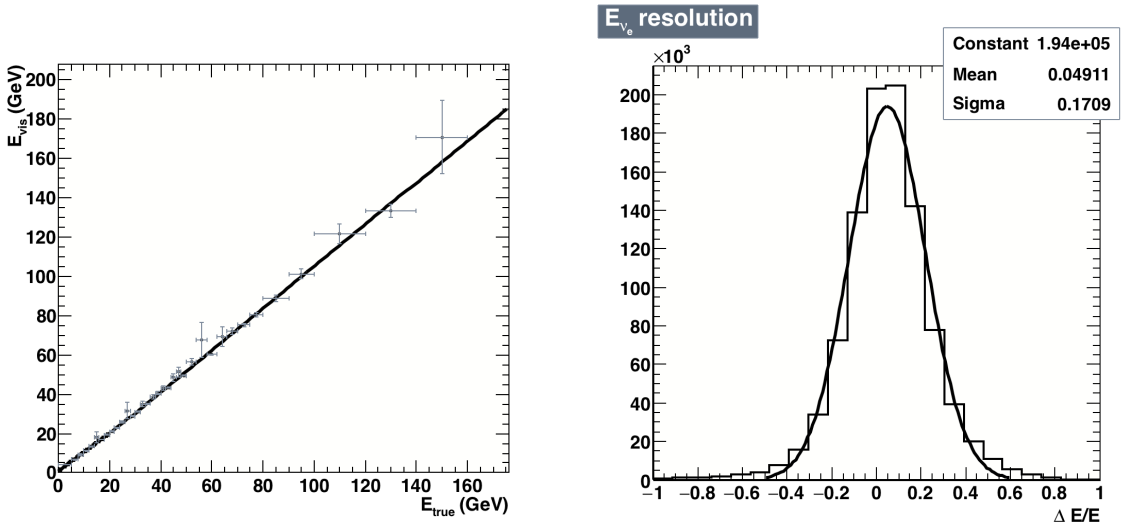

(a) (b)

Figure 4.14: Energy calibration of the visible reconstructed energy as a function of the true MC energy (a) and $\frac{\Delta E}{E}$ distribution (b) for electron neutrinos.

When the τ lepton decays into one or more hadrons it can originate also π^0s and K^0s. If I assume to be able to reconstruct the π^0 starting from the γs produced in its decay, I can close the kinematics and thus correctly evaluate the τ energy. The only hadronic decay modes where I have an unidentified neutral particle are those in which a K^0 is emitted. Since they constitute less than 2% of the total tau lepton branching ratios, I can identify them as pure hadronic events with no other neutral particle emitted than the ν_τ making an error that can be at the moment easily neglected for the following analysis.

Tau decays with only one neutral particle For the previously pointed out reasons, for this analysis I consider only those events where the τ lepton decays into hadrons.

The subscript d refers to variables associated to the τ lepton daughters, while the subscript m (as for "missing") refers to variable associated to the undetected neutrino. Therefore, $\vec{p}_d$ (eq. 4.4) and E_d (eq. 4.5) are respectively the momentum and the energy of the system formed by the τ daughters:

$$\vec{p}_d = \sum_i \vec{p}_i \tag{4.4}$$

$$E_d = \sum_i E_i \tag{4.5}$$

and the mass of the system (m_d) is then:

$$m_d = \sqrt{E_d^2 - (\vec{p_d})^2} = \sqrt{\left(\sum_i E_i\right)^2 - \left(\sum_i \vec{p}_i\right)^2} \tag{4.6}$$

The conservation of the four-momentum at the τ decay vertex gives:

$$\begin{cases} \vec{p}_\tau = \vec{p}_m + \vec{p}_d \\ E_\tau = E_d + E_m \end{cases} \tag{4.7}$$

Recalling that $\vec{p}_\tau$ and E_τ must satisfy the *on shell condition*, i.e. $m_\tau^2 = E_\tau^2 - \vec{p}_\tau^2$.

Using eq. 4.7 and the on shell condition, we get that p_τ is:

$$p_\tau = \frac{-(m_\tau^2 + m_d^2)p_d \cos\theta_k \pm \sqrt{E_d^2[(m_\tau^2 - m_d^2)^2 - 4m_\tau^2 p_d^2 \sin^2\theta_k]}}{2(p_d^2 \cos^2\theta_k - E_d^2)} \tag{4.8}$$

Solving equation 4.8, leads to two possible solutions and, except for some peculiar cases, it is not possible to discard one of them a priori.

Let $p_{\tau,1}$ be the solution of eq. 4.8 with the "+" sign, while $p_{\tau,2}$ is the solution with the "-" sign. I can discard and take $p_{\tau,2}$ as the correct momentum of the τ lepton every time $p_{\tau,1} > 400$ GeV/c, and vice-versa I can consider $p_{\tau,1}$ as the true solution when $p_{\tau,2} < 0$. In all the other cases, I have to take both:

$$p_\tau = \frac{w_1 \cdot p_{\tau,1} + w_2 \cdot p_{\tau,2}}{w_1 + w_2} \tag{4.9}$$

where w_1 is the fraction of cases in which $p_{\tau,1}$ has a lower discrepancy from the true MC value of p_τ and w_2 is the fraction of cases in which it is instead $p_{\tau,2}$ that has a lower discrepancy from the true value. The discrepancy from the MC p_τ value is estimated as:

$$\frac{p_\tau - p_\tau^{MC}}{p_\tau^{MC}}$$

In the decay channel of a τ in one single hadron w_1^{1h} and w_2^{1h} are 52% and 48% respectively. In the decay channel of a τ in three hadrons w_1^{3h} and w_2^{3h} are 48% and 52% respectively. However, when the two solutions differ significantly (e.g: $|p_{\tau,1} - p_{\tau,2}| > 30$ GeV/c), in order to better estimate the momentum of the τ, I used as discriminator the measured τ flight length (Δl):

$$\Delta l_\tau = \frac{p_\tau}{m} c \Delta t_\tau$$

being Δt_τ the mean life time of the τ lepton.

Comparing the one computed using both $p_{\tau,1}$ and $p_{\tau,2}$ to the measured one, I took as better p_τ estimation the solution which gave me the smaller discrepancy between the estimated flight length and the measured one.

The τ lepton reconstructed energy can be obtained by its momentum.

Once again I perform a calibration of the true MC and the visible τ energy, as shown in fig. 4.15 with on the left side the calibration for the $\tau \to 1h$ decay channel and on the right side the one for the $\tau \to 3h$ decay channel.

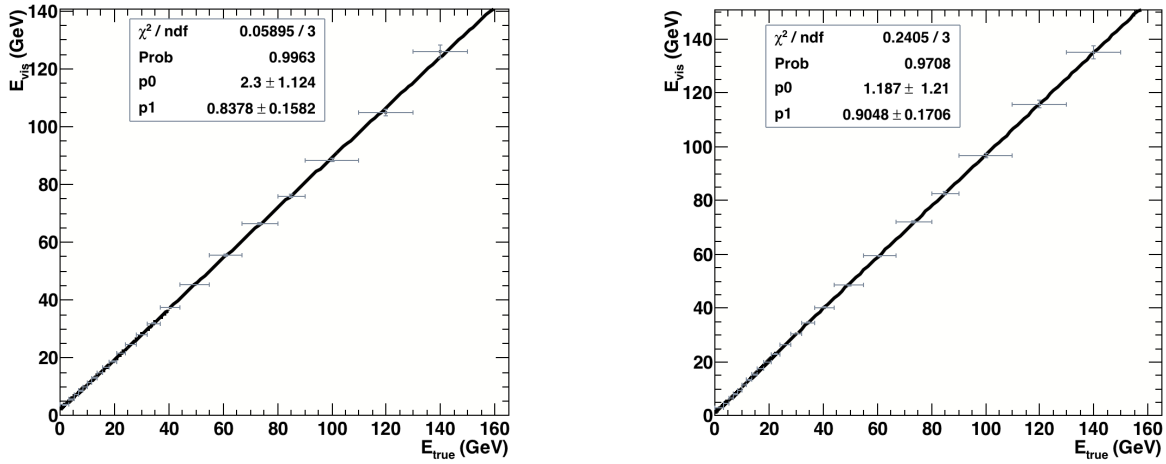

(a) (b)

Figure 4.15: Energy calibration of the visible τ lepton visible energy as a function of E_τ^{MC} for the $\tau \to 1h$ decay channel (a) and for the $\tau \to 3h$ one (b).

In both cases, the visible energy of the τ is parametrized as:

$$E_\tau^{vis} = p_0 + p_1 E_\tau^{MC}$$

With this parametrisation the resolution $\Delta E/E$ (def in eq. 4.3) on the τ lepton reconstructed energy, which is defined as:

$$E_\tau^{rec} = \frac{E_\tau^{vis} - a}{b}$$

In the $\tau \to h$ channel the resolution $\sigma_{E_\tau} = (35 \pm 3)\%$ (see fig. 4.16(a)), while in the $\tau \to 3h$ (see fig. 4.16(b)): $\sigma_{E_\tau} = (22 \pm 2)\%$. In the $\tau \to h$ decay channel, the discrepancy between the solutions $p_{\tau,1}$ and $p_{\tau,2}$ is indeed larger than in the $\tau \to 3h$ case, as it can be seen in fig. 4.4.3.

Reconstruction of neutrino energy Considering only the tau neutrino events with the τ lepton decaying in the hadronic channels and using the previously found resolutions on the τ energy, I followed the same procedure already exploited for the other neutrino flavours to

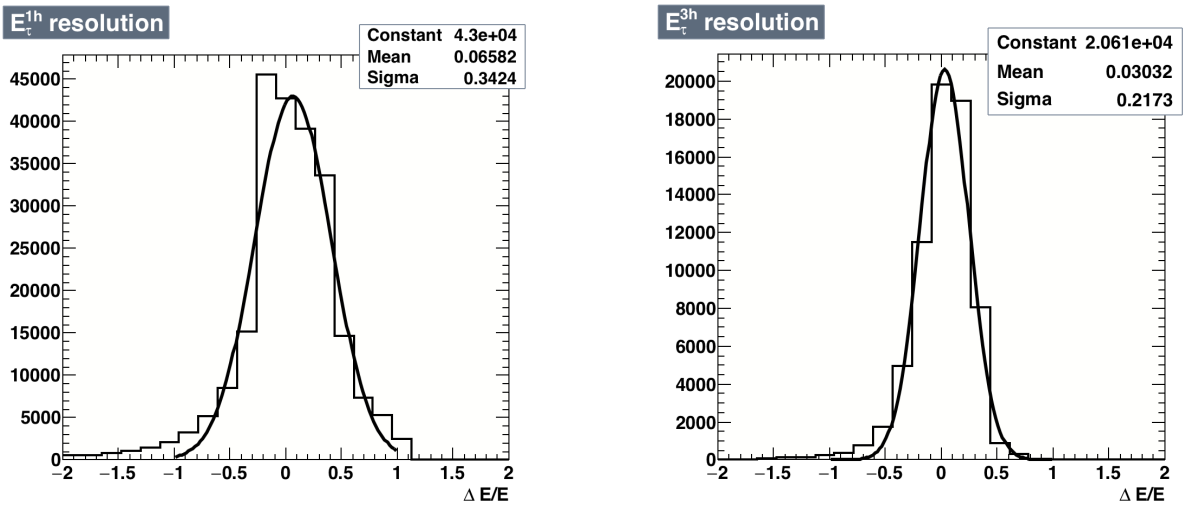

(a) (b)

Figure 4.16: $\Delta E/E$ distribution for the $\tau \to 1h$ decay channel (a) and for the $\tau \to 3h$ one (b).

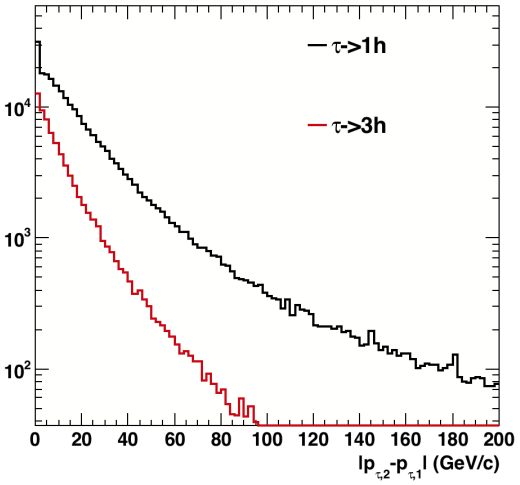

Figure 4.17: Absolute difference between the two solutions of equation 4.8 for the $\tau \to h$ channel in black and for the $\tau \to 3h$ channel in red. On average, the discrepancy between $p_{\tau,1}$ and $p_{\tau,2}$ is larger in the 1-prong channel.

reconstruct the ν_τ energy starting from visible tracks at the neutrino interaction vertex. Results of the calibration between reconstructed and true MC energy are shown in fig. 4.18(a). The resolution on the reconstructed E_{ν_τ} is (see fig. 4.18(b)):

$$\sigma_{E_{\nu_\tau}} = (22 \pm 2)\%$$

As for the ν_e also in this case the resolution on the τ lepton energy is the major component in the total ν_τ energy resolution.

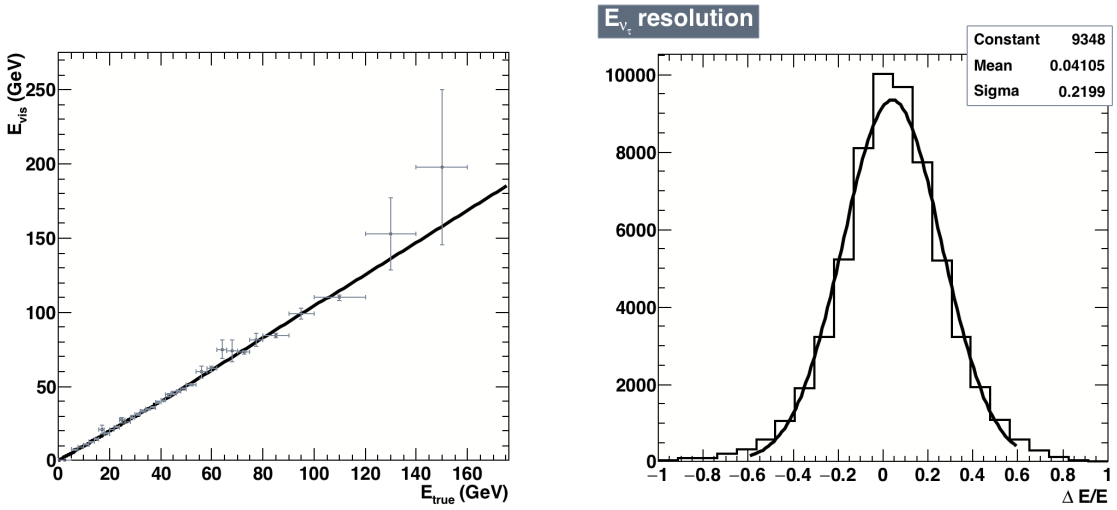

(a) (b)

Figure 4.18: Energy calibration of the visible reconstructed energy as a function of the true MC energy (a) and $\frac{\Delta E}{E}$ distribution (b) for tau neutrinos.

	ν_τ			$\bar{\nu}_\tau$		
decay channel	N^{exp}	N^{bkg}	R	N^{exp}	N^{bkg}	R
$\tau \to \mu$	1031	41	25	756	122	6
$\tau \to h$	1807	108	17	1325	325	4
$\tau \to 3h$	385	43	9	282	124	2
total	3224	192	17	2364	570	4

Table 4.5: Number of expected reconstructed ν_τ and $\bar{\nu}_\tau$ signal (N^{exp}) events together with the expected number of charm background events (N^{bkg}) for the different τ decay channels, except the $\tau \to e$, where the lepton number cannot be determined. The signal to background ratio R is also reported.

4.5 Physics with ν_τ

The number of ν_τ and $\bar{\nu}_\tau$ interactions (tab. 4.5) we expect to collect in five years of data taking can be computed as shown in eq. 4.10 for the muonic τ decay channel and as in eq. 4.11 for the τ decaying in a single hadron or in 3 hadrons.

The charge of the electron cannot be identified, therefore in the $\tau \to e$ decay channel we can only have an inclusive measurement for ν_τ and $\bar{\nu}_\tau$. In this channel we expect to have about 1784 interactions with an overall background of 153 events.

$$N^{exp}_{\nu_\tau(\bar{\nu}_\tau)}(\tau \to \mu) = N_{\nu_\tau(\bar{\nu}_\tau)} Br(\tau \to \mu) \epsilon^{\tau\to\mu}_{tot} \epsilon^{\tau\to\mu}_{kin} \epsilon^{\mu}_{charge} (1 - \eta_\mu) \tag{4.10}$$

$$N^{exp}_{\nu_\tau(\bar{\nu}_\tau)}(\tau \to i) = N_{\nu_\tau(\bar{\nu}_\tau)} Br(\tau \to i) \epsilon^{\tau \to i}_{tot} \epsilon^{i}_{charge} \epsilon^{\tau \to i}_{kin} (1 - \eta_\mu) \tag{4.11}$$

where $i = h, 3h$.

In the previous equations $N_{\nu_\tau(\bar{\nu}_\tau)}$ is the number of $\nu_\tau(\bar{\nu}_\tau)$ interacting in the neutrino target, ϵ_{tot} is the resulting efficiency after applying the geometrical acceptance, primary vertex identification and decay search ($\epsilon_{tot} = \epsilon_{geom} \cdot \epsilon_{loc} \cdot \epsilon_{ds}$), ϵ_{charge} is the efficiency for correct charge assignment, $1 - \eta_\mu$ is the probability that none of the hadrons at the primary vertex is wrongly identified as a muon.

ϵ_{kin} is the efficiency for a selection based on cuts on kinematical variables to discriminate signal from background events.

I have already pointed out that the main background sources to ν_τ selection is given by the charged charmed hadrons when the primary lepton produced at the neutrino interaction vertex is not identified.

In the $\tau \to h$ and the $\tau \to 3h$ decay channels, one of the variables that can be used to discriminate the decays from charmed hadrons or τ leptons is the ϕ angle. It is defined as the angle in the transverse plane between the decaying particle and the hadron jet produced in the decay after removing the particle with the largest ϕ value. As a matter of fact, the τ lepton is usually back to back with respect to the hadronic jet in the plane perpendicular to the neutrino direction, while the charmed hadron tends to be in the middle of it, with the unidentified muon flying in the opposite direction (see fig. 4.19). The background is maximally reduced requiring $\phi > \pi/2$.

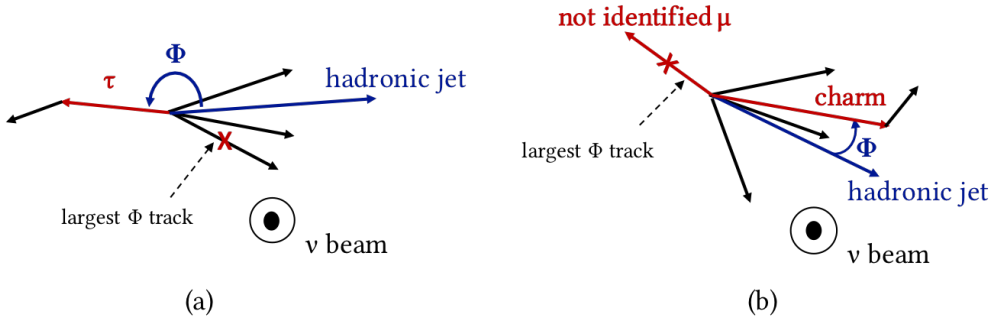

Figure 4.19: ϕ angle defined for the $\tau \to h$ decay channel (a) and for a charmed hadron decay (b).

The kinematical selection efficiency is $70 \pm 7\%$ in both the $\tau \to h$ and $\tau \to 3h$ one. For the background $\epsilon_{kin} = 35 \pm 3\%$ for the charmed hadrons decaying in one prong and $32 \pm 3\%$ for those decaying in 3 prongs.

For the $\tau \to h$ and the $\tau \to 3h$ decay channels, another source of background is represented by the re-interaction of hadrons produced at the primary vertex. To reject background events

originated by the re-interaction of a primary hadron, we require nuclear fragments with angles up to $\tan\theta = 3$ and a transverse momentum at the secondary vertex $p_T > 0.1$ GeV/c. The momentum of the tracks associated to the secondary vertex on the other hand must be above 1 GeV/c.

The number of background events in the $\tau \to h$ and in the $\tau \to 3h$ channels can be computed as:

$$\begin{aligned} N^{bg}_{\nu_\tau}(\tau \to i) = &\sum_{k=\mu,e} N_{\nu_k} \frac{\sigma_{charm}}{\sigma_{\nu_{kCC}}} f_{C^\pm} Br(C \to i) \epsilon_{tot} (1-\epsilon^{charm}_k) \epsilon^i_{charge} \epsilon^{c\to i}_{kin} (1-\eta_\mu) \\ &+ \sum_{k=\mu,e} N_{\bar{\nu}_k} \frac{\sigma_{charm}}{\sigma_{\bar{\nu}_{kCC}}} f_{C^\pm} Br(C \to i) \epsilon_{tot} (1-\epsilon^{charm}_k) \omega^i_{charge} \epsilon^{c\to i}_{kin} (1-\eta_\mu) \end{aligned} \tag{4.12}$$

where: $i = h, 3h$, N_{ν_K} is the number of muon/electron (anti-)neutrinos interactions, $\sigma_{charm}/\sigma_{\nu_{kCC}}$ is the fraction of CC interaction originating charmed hadrons, $f_{C^\pm}$ is the fraction of charmed hadrons produced (56% in neutrino interactions and 28% in anti-neutrino interactions), $Br(C \to i)$ is the branching ratio of charmed hadrons decaying in one or three hadrons, $1-\epsilon^{charm}_k$ is the probability that the primary lepton is not identified and $1-\eta_\mu$ is the probability that none of the primary hadron tracks is identified as a muon.

The main background for the $\tau \to \mu$ decay channel is instead given by charged charmed hadrons decaying in a muon ($Br(C^\pm \to \mu^\pm) = 5.3\%$) and can be suppressed requiring only one muon reconstructed in the MMS and with slopes in agreement with those of the τ decay daughter.

The number of background events in this channel is given by:

$$\begin{aligned} N^{bg}_{\nu_\tau}(\tau \to \mu) = &\sum_{k=\mu,e} N_{\nu_k} \frac{\sigma_{charm}}{\sigma_{\nu_{kCC}}} f_{C^\pm} Br(C \to \mu) \epsilon_{tot} (1-\epsilon^{charm}_k) \epsilon^\mu_{charge} (1-\eta_\mu) \\ &+ \sum_{k=\mu,e} N_{\bar{\nu}_k} \frac{\sigma_{charm}}{\sigma_{\bar{\nu}_{kCC}}} f_{C^\pm} Br(C \to \mu) \epsilon_{tot} (1-\epsilon^{charm}_k) \omega^\mu_{charge} (1-\eta_\mu) \end{aligned} \tag{4.13}$$

4.5.1 Sensitivity studies to F_4 and F_5

The full expression for the neutrino differential Deep Inelastic Scattering (DIS) cross section on a nucleon is:

$$\begin{aligned} \frac{d^2\sigma^{\nu(\bar{\nu})}}{dxdy} = &\frac{G_F^2 M E_\nu}{\pi(1+Q^2/M_W^2)^2} \left\{ \left(y^2 x + \frac{m_\tau^2 y}{2E_\nu M} \right) F_1 + \left[\left(1 - \frac{m_\tau^2}{4E_\nu^2} \right) - \left(1 + \frac{Mx}{2E_\nu} \right) \right] F_2 \right. \\ &\left. \pm \left[xy\left(1 - \frac{y}{2}\right) - \frac{m_\tau^2 y}{4E_\nu M} \right] F_3 + \frac{m_\tau^2 (m_\tau^2 + Q^2)}{4E_\nu^2 M^2 x} F_4 - \frac{m_\tau^2}{E_\nu M} F_5 \right\}, \end{aligned} \tag{4.14}$$

where E_ν is the initial neutrino energy and M and m_τ are the mass of the nucleon and the mass of the τ lepton respectively. It is expressed in terms of five structure functions F_i, $i \in 1,..,5$, which in the Parton Model can be interpreted as a measure of the partonic structure of hadrons. The positive sign multiplying F_3 applies to neutrino scattering while the negative sign applies to antineutrinos.

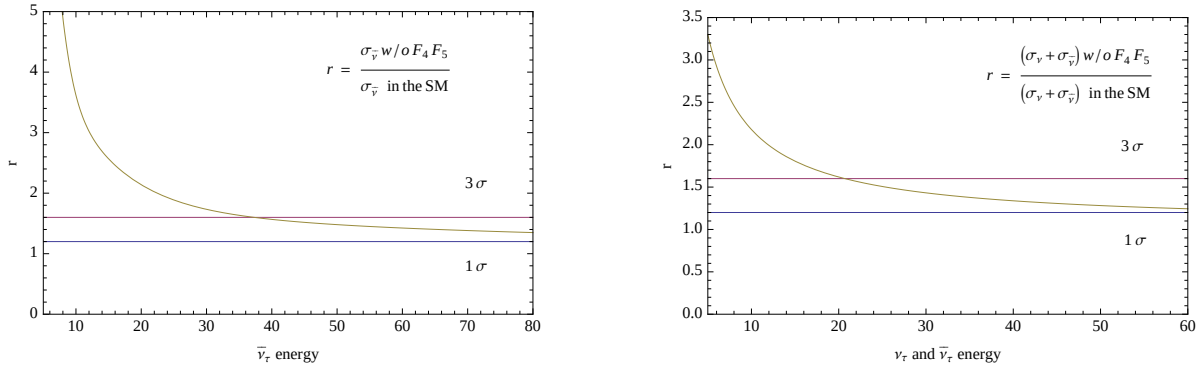

(a) (b)

Figure 4.20: Energy dependence of the ratio r between the DIS cross-section in the $F_4 = F_5 = 0$ hypothesis and in the SM hypothesis, for $\bar{\nu}_\tau$ (left) and for the sum of ν_τ and $\bar{\nu}_\tau$ (right).

In SHiP, the possibility to perform studies of DIS of $\nu_\tau(\bar{\nu}_\tau)$ on nuclei opens the way to the measurement of the structure functions F_4 and F_5, that, unlike the others, are proportional to the ratio m_l^2/E_l, negligible in muon (and electron) neutrino interactions being m_l the associated charged lepton mass.

In section 1.3.1, I have presented the Albright-Jarlskog relations [73]: $F_4 = 0$ and $2xF_5 = F_2$, valid at leading order (LO), in the limit of massless quarks and target hadrons (x is the Bjorken-x variable). However, calculations at next to leading order (NLO) show that the F_4 contribution to this cross-section is about 1% of the one by F_5 [74].

I have also already discussed how a non null value of F_4 and F_5 affects the DIS cross-section with the different behaviour when calculating the cross-section in the LO or NLO hypothesis shown in fig. 1.10. The variable r, defined as the ratio between the cross section in the NLO and LO hypothesis, reflects these discrepancies. As it can be seen in fig. 4.20 they are larger at lower energies and decrease, when $r \to 1$, at higher energies where the contribution of F_4 and F_5 becomes negligible. In 4.20(a) the variable r as a function of the neutrino energy is displayed for $\bar{\nu}_\tau$, while in 4.20(b) it is displayed for the sum of ν_τ and $\bar{\nu}_\tau$.

In both 4.20(a) and 4.20(b) the red line crosses the $r(E)$ function at the energy under which the discrepancy between the NLO and the LO cross-section is bigger than 3σ (σ is the 20% uncertainty on the incoming neutrino flux), hence giving evidence for a non-zero value of F_4 and F_5. For $\bar{\nu}_\tau$ the two curves intersect at $E_x = 38$ GeV: for $E < E_x$ we expect to observe about 300 $\bar{\nu}_\tau$ interactions. For the sum of ν_τ and $\bar{\nu}_\tau$, $E_x = 20$ GeV and the number of expected events at $E < E_x$ is about 420.

4.5.2 ν_τ magnetic moment

The collection of more than 10 thousand ν_τ CC interactions in the neutrino target allows the SHiP experiment to improve the upper limit on a non-zero magnetic moment of the tau neutrino.

As already discussed in section 1.3.2, when a neutrino scatters elastically on an electron, kinematic constraints limit the electron scattering angle in the laboratory frame and the relation 1.12 $\left(\theta_{\nu-e}^2 < 2m_e/E_e\right)$ has to be satisfied: for an electron energy above 1 GeV, $\theta_{\nu-e}$ must be below 30 mrad.

The main sources of background for this analysis are:

- neutrino elastic scattering (ES) with electrons of the target
- electron neutrino and anti-neutrino quasi elastic scattering (QE) with nucleons of the target with non detected outgoing nucleons
- charged current deep-inelastic interactions (DIS) of electron neutrinos and anti-neutrinos with nucleons in the neutrino target with no revealed hadrons in the final state
- electron neutrino and anti-neutrino resonant processes.

In order to take into account the uncertainty on the neutrino interaction position in the neutrino target, a smearing of 1 mrad to the electron angle was introduced although the angular uncertainty is dominated by the measurement accuracy.

Using the GENIE generator to simulate electron neutrino interactions in lead with the proper SHiP energy spectrum, I estimated the number of expected background events due to the above-described sources and the upper limit that the SHiP experiment can hence put on the ν_τ magnetic moment.

I selected as background only the events which had:

- only the electron as reconstructed particle in the final state;
- an electron energy (E_e) above 1 GeV;
- an electron scattering angle $\theta_{\nu-e}$ below 30 mrad.

For deep-inelastic processes, the correlation between the electron scattering angle and its energy can be seen in fig. 4.21. As it can be inferred, the cuts on energy and scattering angles discard a major fraction of the events (92.3% for ν_e and 86.5% of $\bar{\nu}_e$). Adding also the requirement on the number of visible particles in the final state selects only 8.4×10^{-4} of the overall ν_e deep-inelastic scattering events and 5.8×10^{-3} for the $\bar{\nu}_e$ DIS events. The different rejection power between neutrinos and anti-neutrinos can be explained when considering that neutrinos mostly interact with neutrons while anti-neutrinos mostly interact with protons. Therefore, in the final state of an interacting neutrino there is a larger probability to find a proton together with the electron, thus making the identification of background events easier.

Table 4.6 summarizes all the contributions from the different background processes.

The total background yield is:

$$N_{bkg} = 3570 \pm 60_{stat} \pm 180_{sys}$$

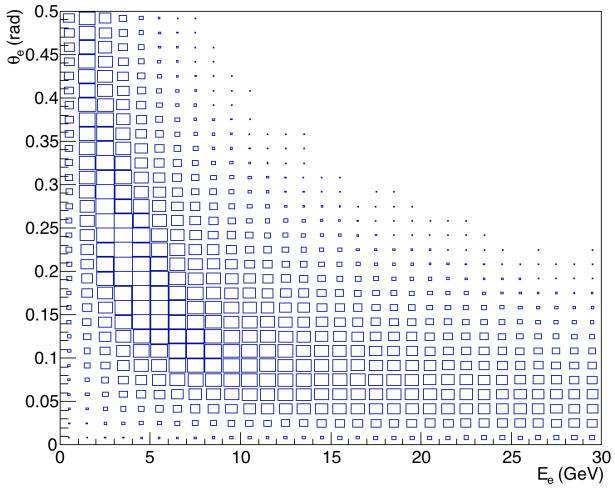

Figure 4.21: Correlation between the electron scattering angle and the electron energy for ν_e deep-inelastic scattering processes.

	$E_e > 1$ GeV
DIS	730
ES	390
QE	1800
RES	650
TOT	3570

Table 4.6: Summary of the contributions of the different sources to the background for the observation of the anomalous magnetic moment of the tau neutrino.

where I have assumed a systematic uncertainty of 5% that is mainly due to the knowledge on the neutrino flux.

Denoting with Φ_{ν_τ} the incoming tau neutrino flux on the detector, with $N_{nucleons}$ the number of nucleons in the neutrino target with σ^μ the contribution of the non-zero magnetic moment to the cross-section and with $\mu_B = 5.8 \times 10^{-5}$ eV T^{-1} the Bohr magneton, the number of expected events for a magnetic moment μ_ν is given by:

$$n_{evt} = \frac{\mu_\nu^2}{\mu_B^2} \times \int \Phi_{\nu_\tau}^{Target} \sigma^\mu N_{nucleons} dE \tag{4.15}$$

Observing an excess of 540 events over the background would allow the SHiP experiment to explore a region down to a magnetic moment of $\mu_\nu = 8.5 \times 10^{-8}$.

4.6 Neutrino induced charm events

As already pointed out in 1.3.3, several experiments , such has CDHS [114], CCFR [115], CHARM [116], CHARM-II [117], NuTeV [71], BEBC [118], NOMAD [106], E531 [119] and CHORUS [120], have proved that charmed hadrons are produced at a level of a few percent in high energy neutrino and anti-neutrino charged-current interactions. Therefore, neutrinos can be considered as a powerful tool to perform charm physics studies.

Being most of the previously cited experiments based on a calorimetric technology, the charmed hadrons produced in neutrino interactions were identified only in the dimuonic decay channel (which has a branching ratio lower than 10%), where two opposite charged muons are expected in the final state. An additional 5 GeV cut on the minimum momentum of the muons was also required to reduce the background. Both these requests drastically reduced the available statistics. As a matter of fact, the NuTeV/CCFR experiment collected more than 1.280.000 ν_μ and 270.000 $\bar{\nu}_\mu$ CC events, but only 5102 ν_μ and 1458 $\bar{\nu}_\mu$ events were classified as neutrino induced charm events.

The choice of the nuclear emulsion technique, instead, allows to identify the charmed hadrons on topological basis. In an emulsion based detector it is indeed possible to distinguish both the neutrino interaction vertex and the vertex produced by the charmed hadron decay, occurring after about one millimetre. Therefore, all the decay channels of the charmed hadrons turn out to be accessible without any kinematical cut.

The CHORUS experiment used the emulsion technique to study neutrino induced charm production. Out of a sample of 143742 located charged-current interaction vertices, 2013 charm candidates coming from ν_μ and 32 coming from $\bar{\nu}_\mu$ interactions were selected [121]. However, no charm candidate from electron neutrino interactions was found.

4.6.1 Expected neutrino induced charm yield

Using the energy dependence of the relative inclusive charm production cross-section ratio as reported in [121] and plotted in fig. 4.22, I computed the relative charm production yield for neutrino and anti-neutrino charged-current interactions expected at SHiP energies.

The results are presented in table 4.7 together with the mean energy of the resulting spectrum. The SHiP experiment will collect more than 1.5×10^5 neutrino induced charmed hadron events, increasing by more than one order of magnitude the statistics collected by the previous experiments. This will not only allow to improve the accuracy of all previous studies results, but also to explore channels not accessible in the past.

In tab. 4.7 the relative charm production yield per neutrino CC interactions is also reported for electron and muon neutrinos and anti-neutrinos. This has been evaluated as:

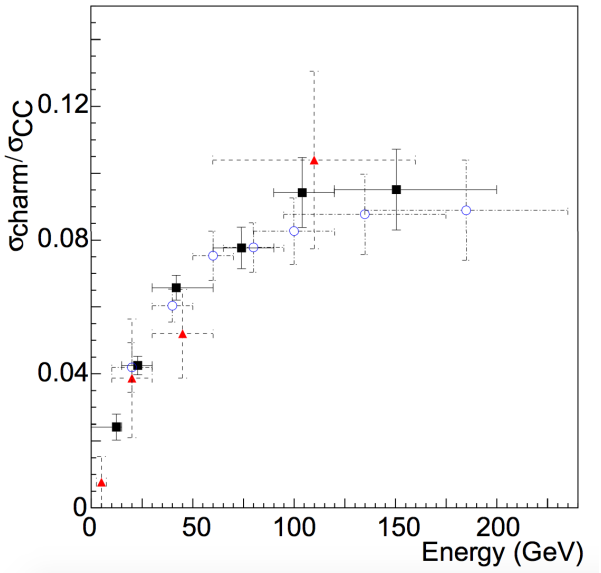

Figure 4.22: Energy dependence of the relative inclusive charm production cross-section ratio [121].

	Expected events	⟨E(GeV)⟩	charm/CC (%)
ν_μ	8.1×10^4	48	4.1
ν_e	3.1×10^4	59	6.2
$\bar{\nu}_\mu$	2.9×10^4	41	3.8
$\bar{\nu}_e$	9.6×10^3	49	5.3
total	1.5×10^5		x

Table 4.7: Summary of the contributions of the different neutrino species to neutrino induced charm events.

$$f(charm) = \frac{\int \Phi_{\nu_l} \sigma^{CC}_{\nu_l} \frac{\sigma_{charm}}{\sigma^{CC}_{\nu_l}} dE}{\int \Phi_{\nu_l} \sigma^{CC}_{\nu_l} dE} \tag{4.16}$$

where $l = e, \mu$.

4.6.2 Sensitivity to s-quark

Charmed hadrons produced in neutrino interactions are important to investigate the strange quark content of the nucleon.

Together with the valence quarks (q_v) that define their quantum numbers, nucleons contain virtual quark-antiquark pairs known as sea quarks (q_s) that are originated by the splitting of a gluon of the nucleons' color field.

To assess the potential impact of the SHiP experiment on the knowledge of the nucleon strangeness, simulated charm data were added to the NNPDF3.0 NNLO [122] fit using the Bayesian reweighing technique introduced and described in [123, 124].

To estimate how ν_μ CC interactions with subsequent charm production were distributed in the E, y, x space, I divided the events of a simulated SHiP data sample produced with the NuAge generator in five bins for the x variable, three for the y variable and three for the neutrino energies. The bin boundaries were chosen in such a way to have almost the same number of entries in each bin. To be conservative, I assumed that the systematic uncertainty for all the bins was of 5% and that this uncertainty was uncorrelated.

In fig.4.23, the uncertainty on the knowledge of parton distribution functions of $s + \bar{s}$ is shown. The blue areas represent the current NNLO estimates [7], while the red areas take into account the information obtained in 5 year run of SHiP, leading to an improvement in the knowledge of parton densities.

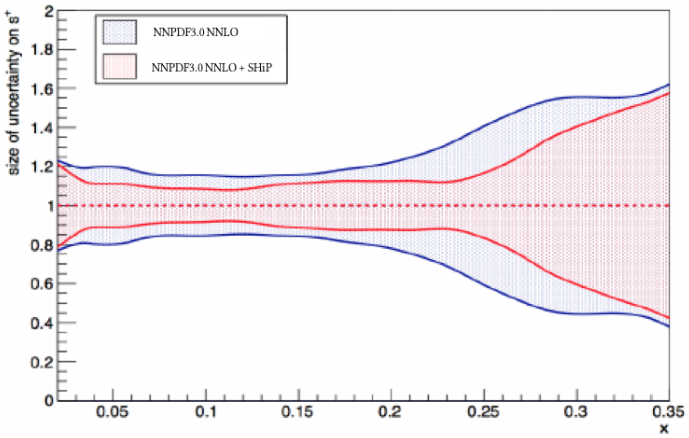

Figure 4.23: Present (in blue) and future (in red) knowledge of parton distribution functions of $s + \bar{s}$ for x spanning from 0 to 0.35.

4.7 Direct Dark Matter searches

Due to the peculiar configuration of the Neutrino Detector, the SHiP experiment is also well suited to search for Light Dark Matter (LDM) particles χ produced by the decay of the dark photon, as explained in sec. 1.2.1, and scattering off electrons and nuclei.

My work has focussed mainly on the study of the background yield in the identification of LDM when scattering off electrons. In this case, the sources of background are, as for the ν_τ magnetic moment searches, neutrinos performing elastic scatterings on electrons, as well as charged current elastic, resonant and deep inelastic scatterings of electron neutrinos off nuclei.

Once again, the GENIE generator was used to generate the background events. I selected as background for LDM searches those events which had only a visible electron in the final state. Based on the correlation between the electron energy and the angle for signal candidates for the two models displayed in fig. 4.24, I further selected only those events which had an electron energy below 20 GeV and a scattering angle in the range 10-20 mrad. The results for the different background yields are reported in table 4.7. The correlation between the electron energy and the scattering angle for elastic scattering of electron neutrinos on electrons (fig. 4.25(a)) and for quasi elastic scattering of electron neutrinos on nuclei (fig. 4.25(b)).

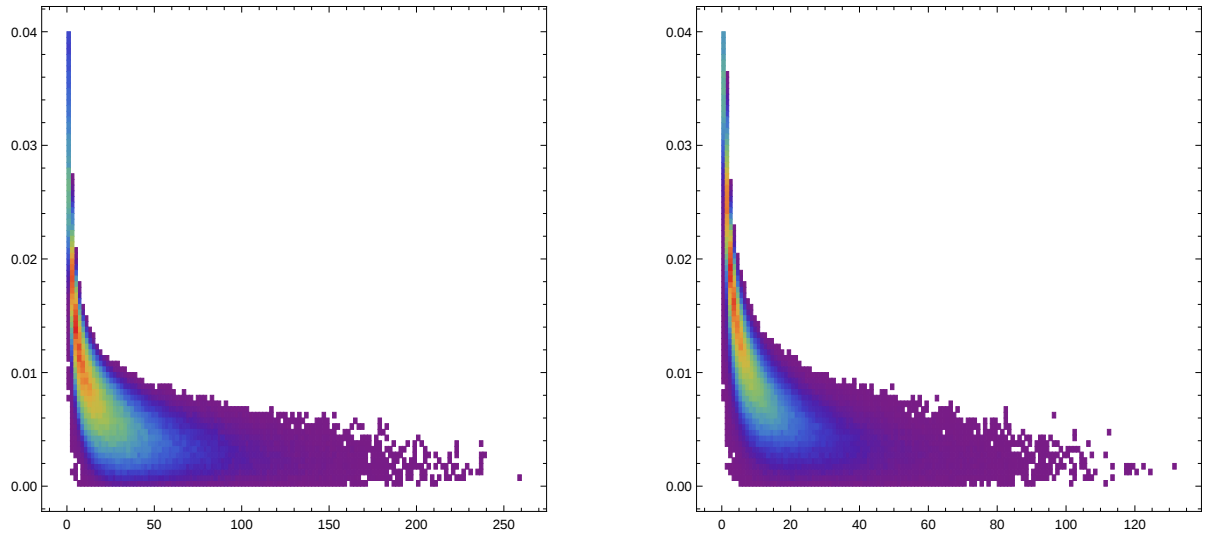

(a) (b)

Figure 4.24: Electron scattering angle (mrad) vs. electron energy (GeV) for signal candidates, (a) in a model with the dark photon of 800 MeV of mass and the dark matter particle of 200 MeV of mass and (b) with the dark photon of 405 MeV of mass and the dark matter particle of 200 MeV of mass.

	ν_e	$\bar{\nu}_e$	ν_μ	$\bar{\nu}_\mu$	all
elastic scattering on e^-	16	2	20	18	56
quasi - elastic scattering	105	73			178
resonant scattering	13	27			40
deep inelastic scattering	3	7			10
total	137	109	20	18	284

Table 4.8: Number of background events to the dark matter search after cuts, from neutrino interactions, as described in the text, with 2×10^{20} p.o.t.

However, since we have considered only two models with specific assumptions on the combination between the dark photon and the dark matter masses, it is better to consider the background

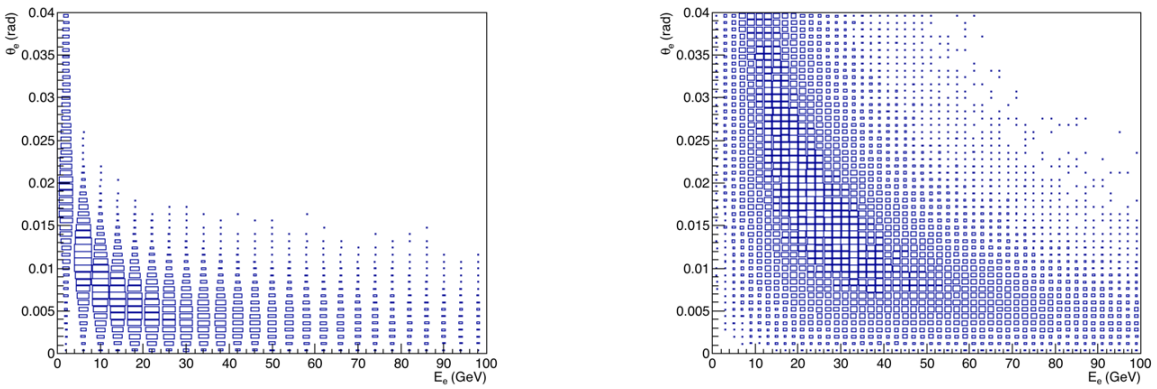

(a) (b)

Figure 4.25: Scattering angle of the electron versus the electron energy for elastic scattering of electron neutrinos on electrons (a) and for quasi elastic scattering of electron neutrinos on nuclei with no other visible particles in the final state (b).

yields only as an order of magnitude calculation.

An analysis performed by P. deNiverville has shown that 50 LDM events would be observed, assuming a LDM target of 2.5 tons of lead[2] with a cylindrical shape with a radius of 0.52 m and a length of 2.1 m and a selection efficiency on the signal events of 50%. Even with only 50 signal events SHiP would be sensitive beyond the relic DM density in minimal hidden-photon model, as shown in fig. 4.26.

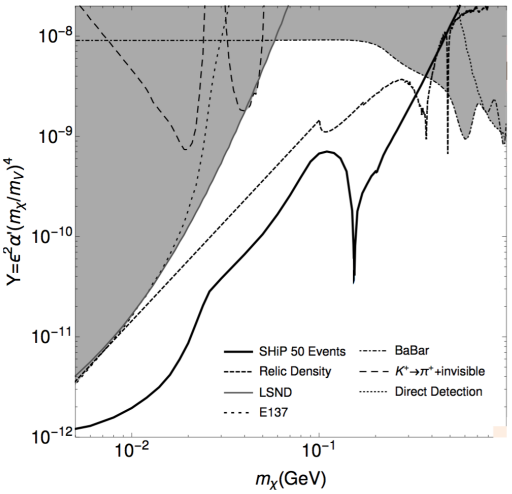

Figure 4.26: SHiP yield for LDM scattering off electrons for a variable LDM mass (courtesy of P. deNiverville).

[2]The Neutrino and LDM Detector is ~ 9.6 tons of lead

CHAPTER 5

OPTIMIZATION STUDIES

5.1 New experimental layout

In section 2.3 I described the layout of the active muon shield needed to clear a 5 m wide region from muons up to 350 GeV, as presented in the Technical Proposal (TP). We recall that in the TP option, the muon shield was 48 m long and it started after ~5 m of proximity shielding placed downstream of the target. Therefore, the first magnets of the muon shield had to have a large aperture to guarantee, at the z corresponding to the start of the 5 m wide cylindrical decay volume, a deflection of the background muons sufficient to avoid their entrance in the vessel.

In preparation for the Technical Design Report, the idea to gain in acceptances for Hidden Particle searches by placing the decay volume closer to the beam dump has been explored.

Simulation studies have indeed shown that, as expected, moving the vessel closer to the proton target while keeping its length fixed increases the acceptance on detected Hidden Particles. Being produced by the decay of heavy hadrons, they show a high transverse momentum and it is their angular divergence that dominates their acceptance rather than the long $c\tau$. Figure 5.1 shows the number of detected HNLs originated either by charmed hadrons (green line) or by beauty hadrons (blue line) as a function of the distance of the vessel from the proton target. In this figure, the relative normalisation of beauty and charm production is arbitrary. In the TP configuration the decay vessel is placed 60 m far from the proton target. Moving it at a distance of 35 m increases by approximately 30% the number of possible identified HNLs.

To move the vessel closer to the proton target, a preliminary step is studying the feasibility of a frustum decay vessel, with a shape reproducing the development of the muon free region along the beam axis. The studies, confirming this possibility, have been performed by the engineers in Naples and have thus allowed to proceed with the design of a shorter muon shield. Shortening

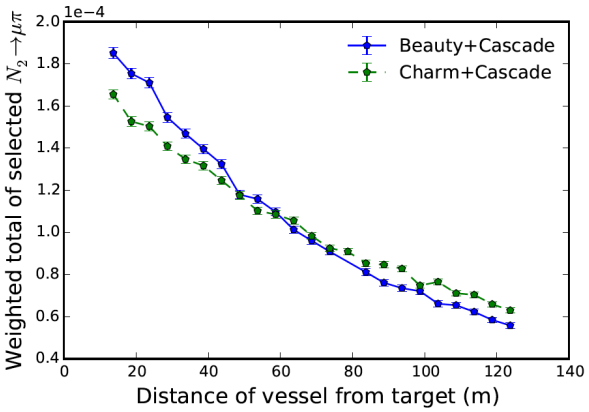

Figure 5.1: Number of detected HNLs in the $\pi\mu$ decay channel as a function of the distance of the vessel from the proton target.

the muon shield also substantially reduces its weight and hence its cost.

Two-dimensional simulation studies, used to define a preliminary geometry of the muon shield and to have a hint on both its length and its weight, have shown that to guarantee at least a 2 m wide region along the horizontal axis at the entrance of the decay volume, the muon shield has to be at least 34.2 m long. To gain more in terms of distance between beam dump and decay volume, the idea of magnetising also elements of the target bunker has been considered. The SHiP target bunker can be split into 3 sections:

- *Target*: 60 cm of Mo, 60 cm of W.
- *Stop-1*: water cooled Fe shielding, 1.4 m long.
- *Stop-2*: fixed Fe shielding, 3.4 m long.[1]

Different magnetisation options for the different elements of the target bunker have been implemented in the 2D simulation. The results of this 2D study are reported in table 5.1.

Target	Stop-1	Stop-2	Tot. length (m)	Weight (ton)
0T	0T	0T	34.2	4116
0T	0T	1.8T	32.9	2098
0T	1.8T	1.8T	29.5	1458
1.0T	1.8T	1.8T	26.0	1161
1.8T	1.8T	1.8T	25.2	1032

Table 5.1: Table showing the possible field options for the different components of the target bunker and the resulting muon shield length and iron content.

[1]Stop-1and Stop-2 make up the Hadron Stopper.

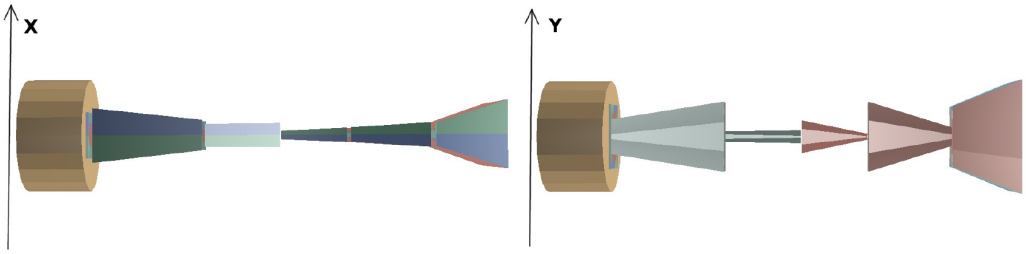

Figure 5.2: New muon shield layout implemented in FairShip. Left: top view. Right: side view. Different colours illustrate the different magnetic field orientation in the different magnets of the muon shield.

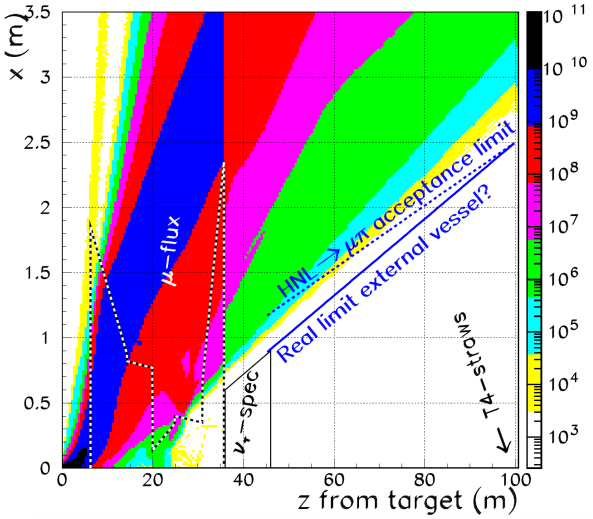

Figure 5.3: Amount of background muons in the different regions of the $x-z$ plane.

The magnetisation of the target has been ruled out by target experts. Therefore, the only possible options is to magnetise either only *Stop-2* or *Stop-1 + Stop-2*.

The option considered for further optimisation foresees the magnetisation of both the elements of the hadron stopper. This option has been implemented in the official software of the experiment (FairShip) and is shown in fig. 5.2. The deflection of the muon flux at different distances from the target can be seen in fig. 5.3.

Assuming the decay vessel to be placed at ≈40 m from the proton target, the position in the $y-z$ plane of the decay vertices of reconstructed HNLs events is reported in fig. 5.4.

As it can be seen, the decay vertices are all distributed within a cone. Thus, no losses come from the assumption of a decay volume shaped as an elliptical frustum. The entrance window of the vessel is an ellipse with a major axis of 4 m and a minor axis of 2 m. The rear window of the vessel is again an ellipse, but this time the major axis is 10 m long and the minor axis is 5 m long. The length of the decay volume is left invariant, since it has also been shown that the HP

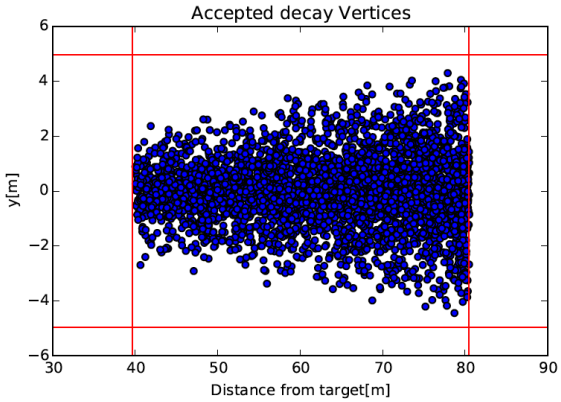

Figure 5.4: Number of detected HNLs in the $\pi\mu$ decay channel as a function of the distance of the vessel from the proton target.

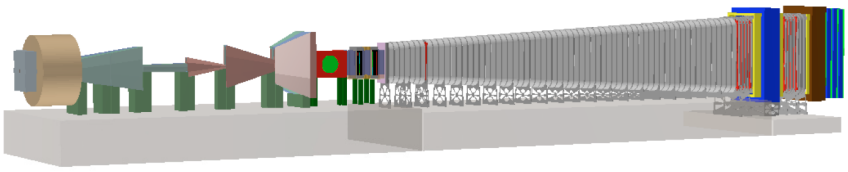

Figure 5.5: New layout of the SHiP experiment with a shorter muon shield and an elliptical frustum shaped decay vessel.

acceptance as a function of this parameter is approximately independent on the distance from the proton target. The choice of an elliptical frustum is also suitable with the muon-free region obtained with the new muon shield design. The new setup is shown in fig. 5.5 and a closeup view on the Neutrino Detector is shown in fig. 5.6.

5.2 A new configuration for the Neutrino Detector

With the new muon shield layout, also the Neutrino Detector moves closer to the target being placed upstream with respect to the hidden sector detector. Therefore, to remain in the region cleared from the huge background muon flux, its transversal dimensions must be reduced. This automatically rules out the Goliath magnet, identified in the TP phase as the magnet to host the Neutrino Detector.

To estimate the new transversal dimensions of the Neutrino Detector in such a way that no

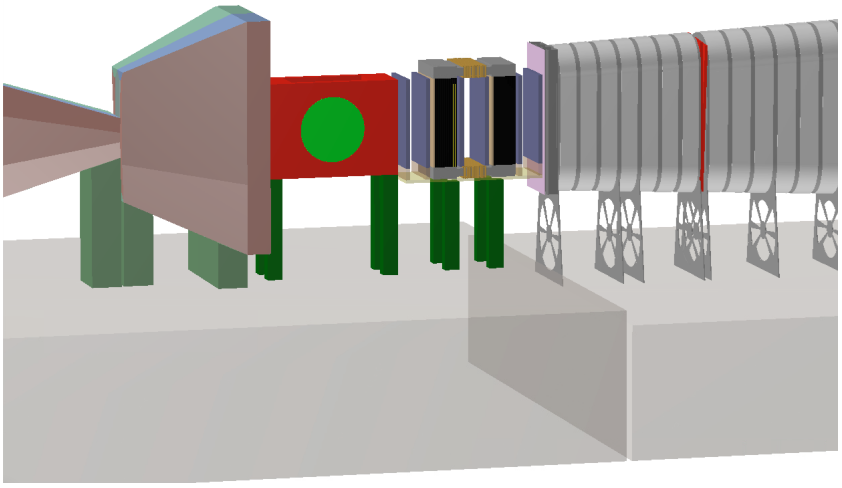

Figure 5.6: Close up view on the new layout for the Neutrino Detector.

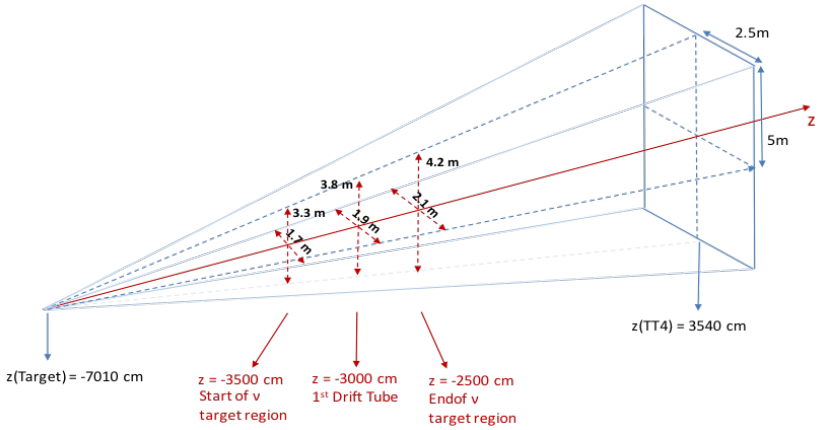

Figure 5.7: Region identified by connecting the extremes of the last straw station (TT4) with the beam dump. In the so identified region potential background tracks entering the decay vessel can be identified and discarded.

tracks originating inside the system constitute a background to the hidden sector searches, I have ideally traced a line connecting the beam dump to the edges of the last straw station (TT4). Within this region the potential background tracks produced which enter the decay vessel can indeed be identified and discarded (fig. 5.7).

The maximum possible sizes of the Neutrino Detector in the transverse plane at the z immediately downstream of the muon shield, at the z of the first drift tube tracker and at the end of the region allocated for the Neutrino Detector are reported in tab. 5.2. The first column of the table (ΔZ_{BD}) represents the distance from the proton target. A further optimisation of both the muon shield and the Neutrino Detector is currently ongoing to match the dimensions reported in tab. 5.2 used to design the new Neutrino Detector with the muon free region shown in fig. 5.3.

ΔZ_{BD} (m)	Δx (m)	Δy (m)
35.1	1.7	3.3
40.1	1.9	4.8
45.1	2.1	4.2

Table 5.2: Maximum sizes of the Neutrino Detector in the transverse plane at the beginning of the Neutrino Detector dedicated region, at its centre and at the end.

Being closer to the proton target is an advantage in terms of the incoming neutrino flux, however the constraints previously identified on the sizes of the Neutrino Detector are pretty harsh. The dimensions of the emulsion target have been optimised in such a way to have approximately the same number of neutrino interactions as quoted in the TP.

The Goliath magnet is not suitable anymore for hosting the Neutrino Detector being too wide in both x and y dimension. Therefore two new possible options for a magnet to host the emulsion target are being considered at the moment. One is displayed in fig.5.8(a) (option A), the other one is shown in fig. 5.8(b) (option B).

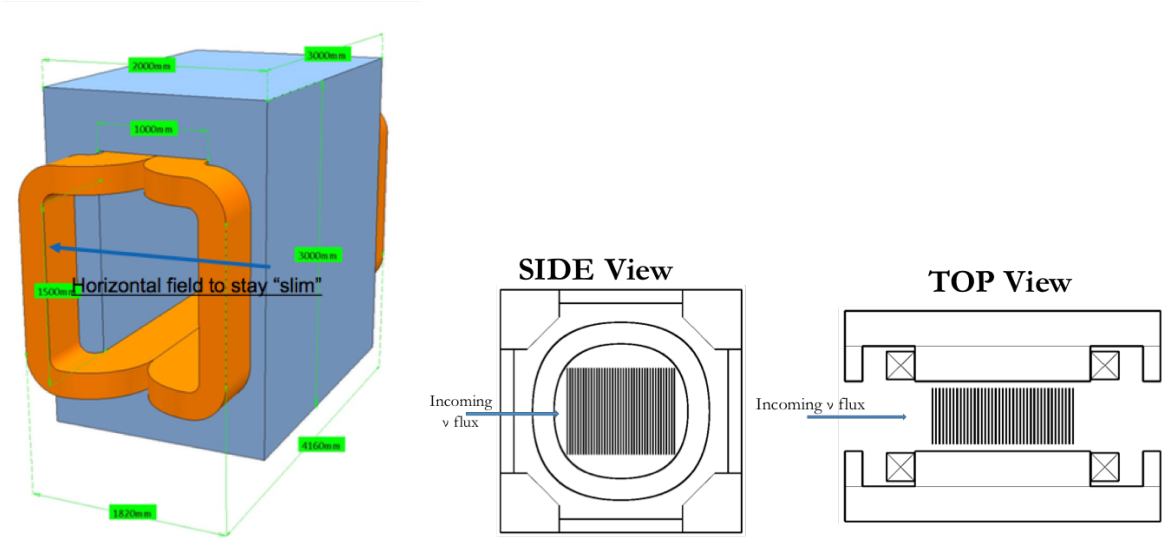

(a) Option A (b) Option B

Figure 5.8: Two options for the magnet of the neutrino target.

The option A is compatible with the allowed region for the emulsion spectrometer, however it is not comfortable for replacing the emulsion target because it would require splitting the iron part into two pieces. The option B, on the other hand, allows the extraction of the emulsion target from the top side of the magnet. However the dimensions of this magnet are still too big to fit in the allowed region, being $4.5 \times 4.5 \times 3$ m^2. Both the designs foresee a horizontal magnetic field with a strength of about 1T and are being optimised.

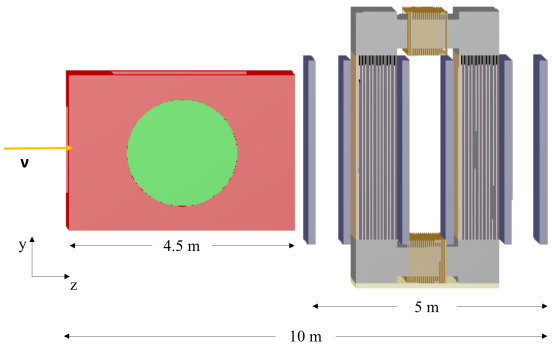

(a) Lateral view.

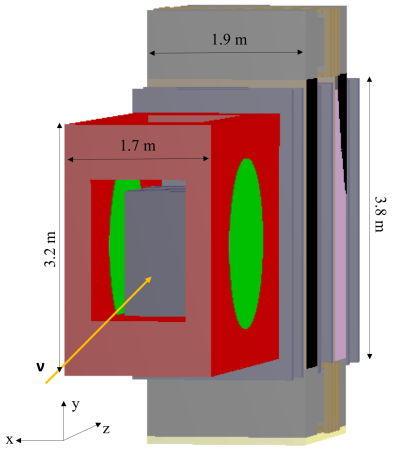

(b) Frontal view.

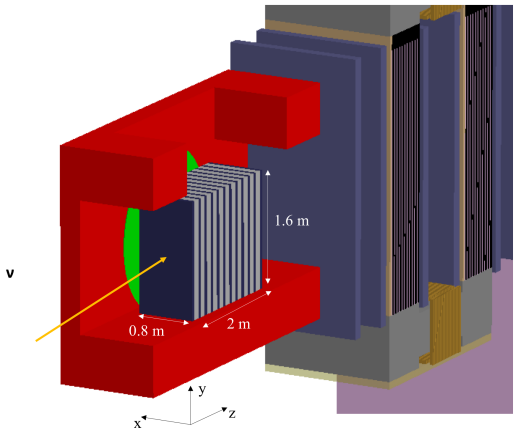

(c) Close up on emulsion target.

Figure 5.9: New layout of the Neutrino Detector.

I used the design in fig. 5.8(b) as a starting point to delineate the new Neutrino Detector layout. The new layout, as I have implemented in the FairShip software, is shown in fig. 5.9. The new emulsion target is placed in a horizontal magnetic field. Its volume is $0.8 \times 1.6 \times 2$ m^3 and it is made of 924 bricks arranged in 6 columns (along the x direction), 14 rows (along the y direction) and 11 walls (along the z direction).

As it can be seen from fig. 5.9 (a) the muon magnetic spectrometer has the same layout as in fig. 3.8, however its dimensions have been shrinked to fit in the region with lower muon rate.

In the meantime an option to improve SHiP sensitivity in LDM searches is also being explored. This option considers an increment of the detector mass obtained by removing the magnet surrounding the Neutrino Detector, together with the optimisation of the structure and of the material of the ECC bricks to improve the electron identification efficiency and to enhance the performances for the reconstruction of the electron energy.

Neutrino flavour	< E > GeV	Neutrino Detector	< E > GeV	CC DIS
ν_μ	9	8.1×10^{16}	31	2.3×10^6
ν_e	26	1.0×10^{15}	50	6.3×10^5
ν_τ	21	8.4×10^{14}	45	2.6×10^4
$\bar{\nu}_\mu$	7	6.7×10^{16}	26	8.6×10^5
$\bar{\nu}_e$	19	9.6×10^{15}	38	2.2×10^5
$\bar{\nu}_\tau$	29	8.8×10^{14}	58	1.9×10^4

Table 5.3: Integrated neutrino yield for 2×10^{20} p.o.t. and corresponding mean energies for the different neutrino flavours at the Neutrino Detector (left column) and their charged current interactions (right column).

Neutrino	< E > (Gev)	Expected events	charm/CC (%)
ν_μ	45	1.3×10^5	3.9
ν_e	57	4.9×10^4	5.9
$\bar{\nu}_\mu$	39	4.9×10^4	3.6
$\bar{\nu}_e$	46	1.6×10^4	5.1
total		2.4×10^5	

Table 5.4: Induced charm events from muon and electron (anti-)neutrinos.

5.2.1 Expected event yield

With the new detector layout, I estimated the number of expected neutrino interactions in the emulsion target. The results are reported in tab. 5.3. From a comparison with the rates presented in section 4.2, it can be seen that the incoming neutrino flux on the Neutrino Detector in the new configuration is almost doubled with respect to the TP expected flux. Being closer to the target results in a larger angular acceptance and therefore a slightly decreased mean energy of the incoming neutrino fluxes with respect to that of the previous layout. As a matter of fact, in the TP layout, only the most collimated component of the neutrino flux, i.e. the most energetic one, was selected.

This trend reflects also in the number of expected interactions, again almost twice the amount expected in the TP configuration.

The increment in the number of neutrino interactions leads also to an increasing number of charmed hadrons induced events, as reported in tab. 5.4 to be compared with tab. 4.7.

5.2.2 Evaluation of overall detector performances

A detailed study was performed in order to assess what is the efficiency of muon identification in ν_μ ($\bar{\nu}_\mu$) events with induced charm production.

Muon neutrino events originating from charmed hadrons have been distributed uniformly in

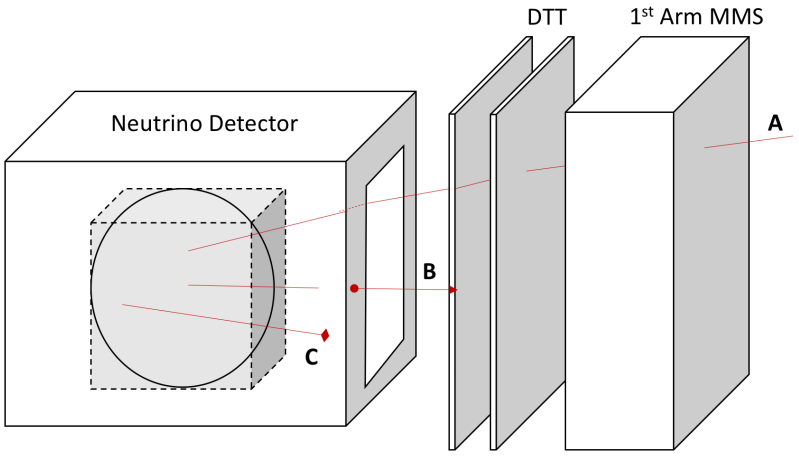

Figure 5.10: Schematic drawing of the different muon topologies.

the neutrino target and the fraction of muons entering either the walls of the target magnet or the MMS has been evaluated. The possible muon topologies are presented in fig. 5.10:

- 73% of the muons reach the Spectrometer without entering the target Magnet (option A).
- 1% of the muons stop inside the neutrino target and 3% exits laterally from the neutrino target
- The remaining 23% of the muons enters the target Magnet. Among them 17% exit the magnet and reach the first DTT plane (option B), 1% is absorbed inside the magnet (option C) and 5% exits but does not reach the first DTT plane due to the acceptance.

Recalling the criteria for muon identification listed in sec. 4.3, an identification efficiency $\epsilon_{\mu ID}^{1ry} = 90\%$ has been estimated for muons produced in a muon neutrino interaction with induced charm production, in agreement with that found in the TP configuration. This efficiency is instead $\epsilon_{\mu ID}^{2ry} = 89\%$ for muons produced in τ lepton decays.

The efficiency of correct charge identification is left unchanged (94%).

The number of ν_τ and $\bar{\nu}_\tau$ interactions we expect to collect in five years of data taking in this new configuration is reported in tab. 5.5. These numbers have been obtained by using eq. 4.10 for the muonic τ decay channel and eq. 4.11 for the τ decaying in a single hadron or in 3 hadrons. In the $\tau \rightarrow e$ decay channel, we conservatively assume to not perform lepton number identification, therefore the total number of expected events is 4067 over a background of 281 and a resulting signal to noise ratio of 14.

	ν_τ			$\bar{\nu}_\tau$		
decay channel	N^{exp}	N^{bkg}	R	N^{exp}	N^{bkg}	R
$\tau \to \mu$	2212	73	30	161	210	8
$\tau \to h$	3788	185	20	2768	547	5
$\tau \to 3h$	894	81	11	653	231	3
total	6893	339	20	5037	988	5

Table 5.5: Number of expected reconstructed ν_τ and $\bar{\nu}_\tau$ signal (N^{exp}) events together with the expected number of charm background events (N^{bkg}) and the resulting signal to noise ratio (R).

5.3 Muon Background studies

The propagation within the FairShip framework of $\approx 2\times10^7$ muons produced by pion/kaon/charmed hadron decays at the beam dump, gives, after proper re-weighting to one spill, an estimate of the background rates we expect in the different sub-detectors of the Neutrino Detector.

The muon background rates are particularly important for the Neutrino Detector because they define the rate of emulsion film replacement during the data taking. As a matter of fact, in the emulsion films, tracks are integrated over the whole exposure time: if the track density exceeds $10^3/\text{mm}^2$, it becomes difficult to reconstruct tracks without ambiguity.

Estimating the rates of background particles is also important for the definition of the technology to use in the Muon Magnetic Spectrometer (e.g. using the RPCs in streamer or avalanche mode) and the operation conditions of the drift tubes.

5.3.1 Background in the sensitive layers of the MMS

I have studied the background particles entering the MMS. In particular, I have focussed my attention on the hits produced in the 22 RPC layers in the two arms of the spectrometer.

The rates of muons entering the MMS ranges from ~ 2.5 Hz/cm^2 in the first RPC layer (closer to the beam dump) down to ~ 0.1 Hz/cm^2 in the most downstream layer (number 22) as shown in fig. 5.11(b). Approximately 45% of the muons have a momentum larger than 200 GeV (see fig. 5.11(a)).

The majority of hits in the RPCs is produced by $e^\pm$. This electromagnetic component comes mainly from photons produced by muon bremsstrahlung in the most downstream part of the muon shield. Only 8% of these electrons is a δ-ray associated to the passage of muons in the iron slabs interleaving the RPCs and these electrons do not constitute a problem being in time with background muons and within the RPC spatial resolution. Their only contribution is thus to enhance the signal of the muon. The electron rates (fig. 5.12(b)) are higher in the first layer ($\sim$ 65 Hz/cm^2), then they decrease to $O(10)$ Hz/cm^2 at the end of the first arm and slightly increase again in the first RPC of the second arm ($\sim$ 20 Hz/cm^2) and keep decreasing until the last RPC

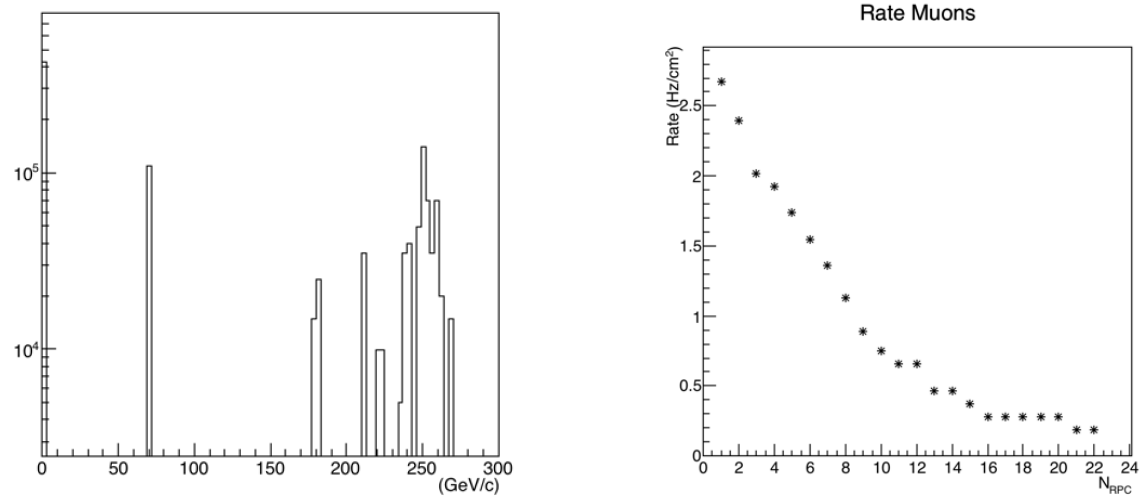

(a) (b)

Figure 5.11: Momentum distribution of muons hitting the RPC layers (left). Rates of muons per cm^2 entering each RPC layer (right).

layer. The momentum distribution of this electromagnetic component is instead shown in fig. 5.12(a).

The position distribution of all the hits generated in the RPCs and integrated over all the RPC layers is shown in fig. 5.13(a). As it can be expected, the majority of the hits is concentrated at both sides of the active MMS region. The same trend can be observed also for the muon hits as it can be seen in fig. 5.13(b) where the structure of consecutive points represent the trajectories of muons crossing several RPC layers, more evident in the right plot of fig. 5.13. The position distribution of the hits I have found on the RPC layers is due to the deflecting power of the muon shield which, so far, has been optimised only requiring that no muons enter the last straw-tube station tracker placed at the end of the HP decay volume. This defines a very narrow region free from high muon rates which is slightly overstepped by the MMS dimensions.

If the expected particle rates can still be afforded by RPC detectors, provided that the RPCs operate in avalanche mode, the same cannot be said for the Drift Tube Trackers (DTT). To reduce the rates of electrons/positrons hitting the sensitive layers of the MMS, I simulated a lead shield attached laterally to the MMS system (see fig. 5.14). Given the spectrum of the $e^{\pm}$ (see fig. 5.12(a)), I considered two different thickness options: a 7 mm thick shield and a 15 mm thick one.

The ratio between the $e^{\pm}$ rates without and with the shield is reported for the different RPC layers in fig. 5.15(a) and in fig. 5.15(b) for the two options, respectively. The rates in the two different configurations are also displayed in fig. 5.16.

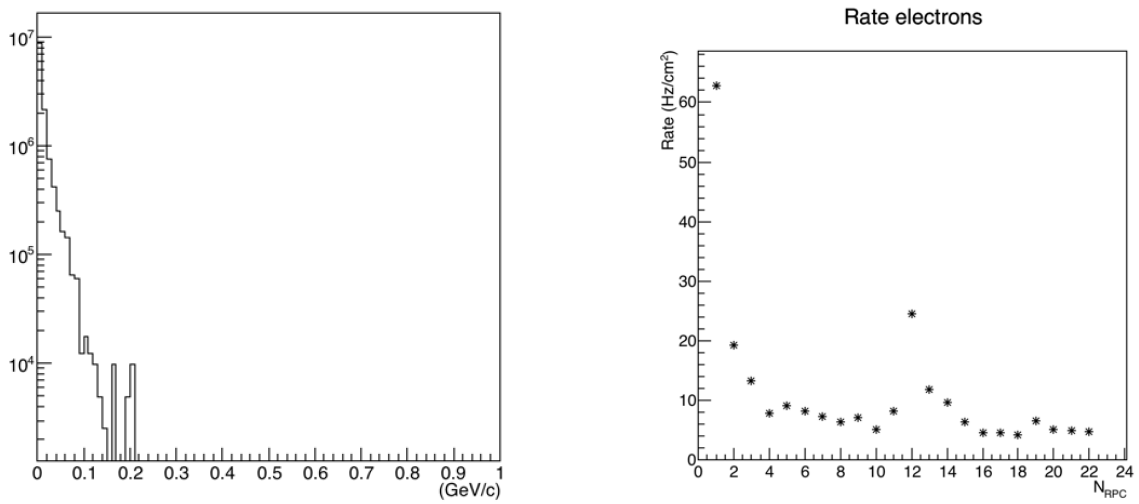

(a) (b)

Figure 5.12: Momentum distribution of the electromagnetic component hitting the RPC layers (left) and the corresponding rates in each RPC layer (right).

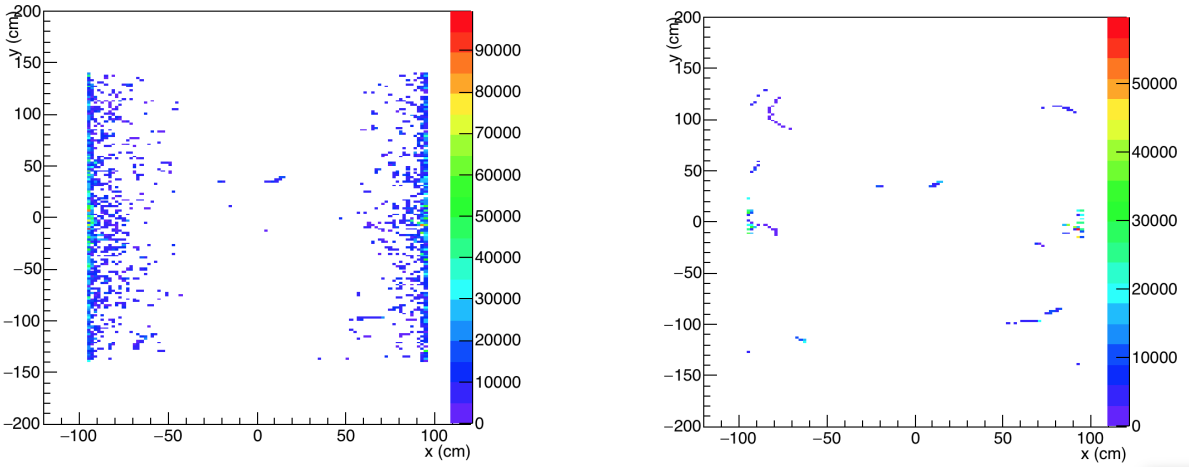

(a) (b)

Figure 5.13: Spatial distribution of hits integrated on all the RPC layers. On the left, spatial distribution of all particles, on the right spatial distributions of muon hits only .

5.3.2 Background in the Target Tracker (TT) planes

I performed a similar study also for the Target Trackers (TT) which interleave the brick walls in the Neutrino Detector. In this case I estimated the rates collected in 2×10^{19} p.o.t.s, corresponding approximately to six months of data taking, assuming that we replace the emulsions ten times during the whole data taking.

I found that only $\sim 40\%$ of the muons hitting the Neutrino Detector have a momentum larger

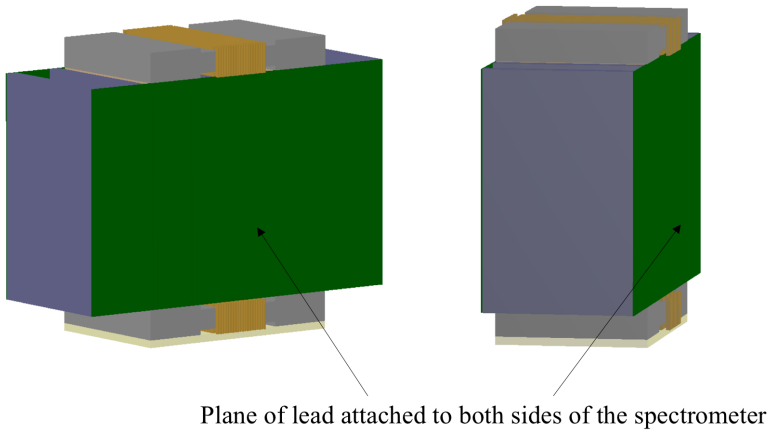

Figure 5.14: Implementation of a lead shield on both sides of the MMS to study the effect on the $e^{\pm}$ rates in the RPCs.

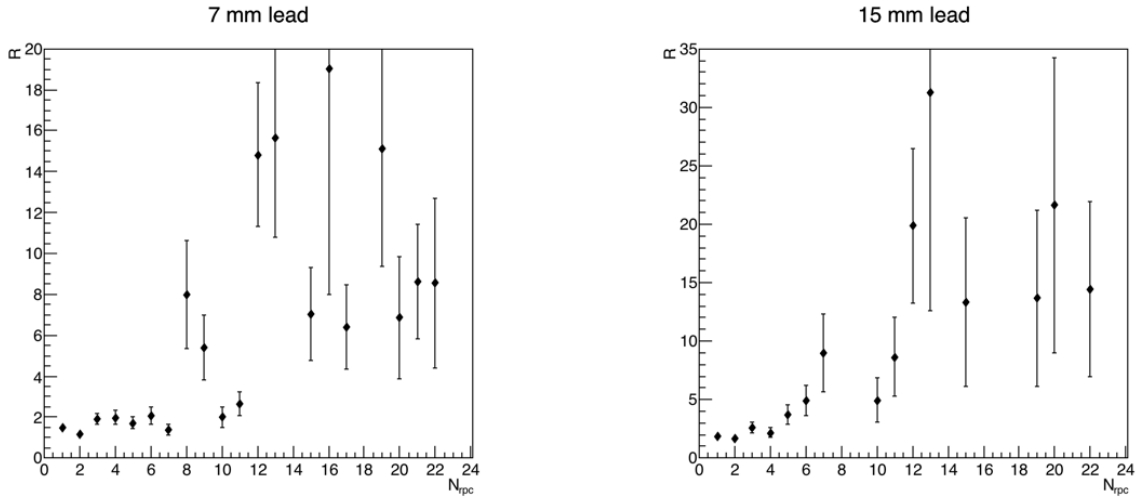

(a) (b)

Figure 5.15: Ratio between the $e^{\pm}$ rates without and with the shield for 7 mm (left) and 15 mm (right) shield.

than 1 GeV/c as shown in fig. 5.17(a). These less energetic muons traverse only a few planes and suffer from a large bending in magnetic field, as well as a large scattering when they traverse the lead plates in the ECC bricks. Therefore they are not easy to reject. Instead, high momentum muons suffer less from both bending and scattering. They can be reconstructed as penetrating tracks, used for emulsion alignment and then virtually erased and thus excluded from the event analysis. Optimisation of the muon shield is ongoing to reduce the rates of muons entering the Neutrino Detector.

Also in this case the electromagnetic component is mainly given by $e^{\pm}$ originated by muon

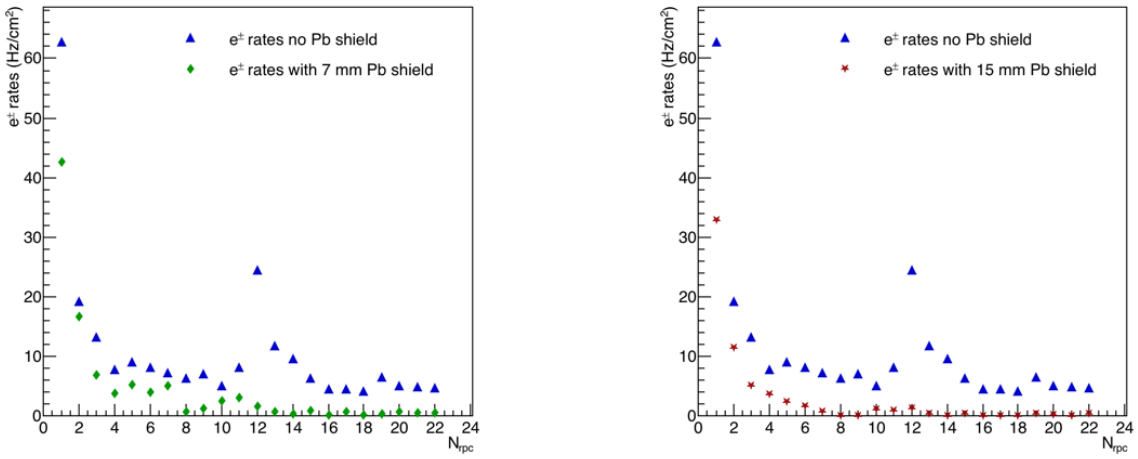

(a) (b)

Figure 5.16: $e^{\pm}$ rates without and with a shield with a thickness of 7 mm (left) and 15 mm (right).

bremsstrahlung in the muon shield. The rates of the few MeV electrons and positrons (fig. 5.17(b)) hitting the TT planes are more than double with respect to the muon ones, hence a solution with a lead shielding surrounding the Neutrino Detector, as already for the MMS, has to be considered.

The spatial distribution of all hits integrated on all the TT planes is shown in fig. 5.18(a), while that of the muons alone is shown in fig. 5.18(b). Once again, in fig. 5.18(b) the structures with consecutive hits are more evident and represent the trajectories of muons crossing several active planes. Differently from the spatial distribution observed for the electromagnetic component on the RPC layers, hits are placed also on the upper region of the TT planes being the magnet hosting the Neutrino Detector open on the top to allow the neutrino target extraction.

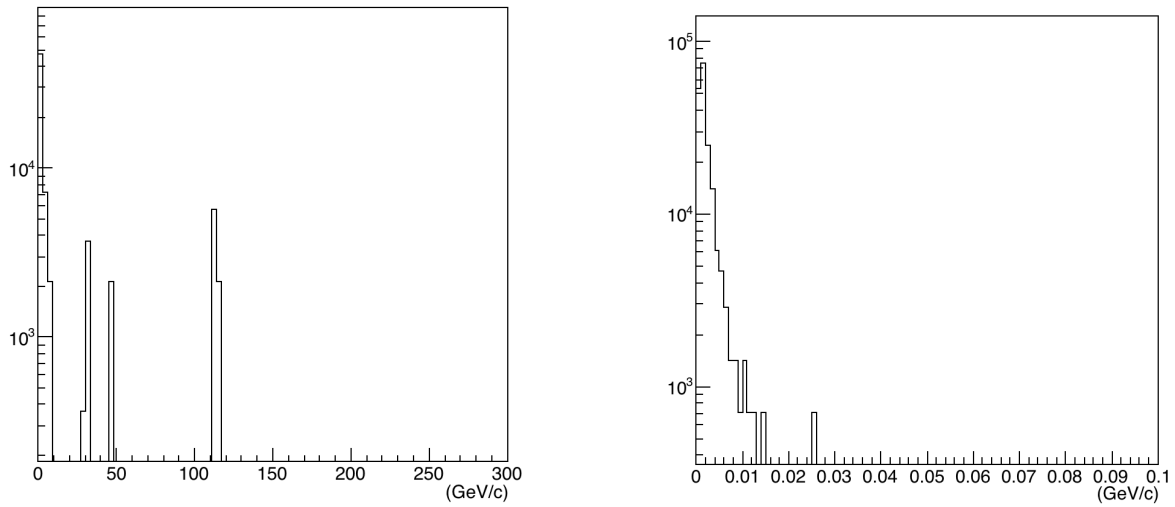

(a) (b)

Figure 5.17: Momentum of muons (left) and $e^{\pm}$ (right) hitting the electronic detectors in the Neutrino Detector.

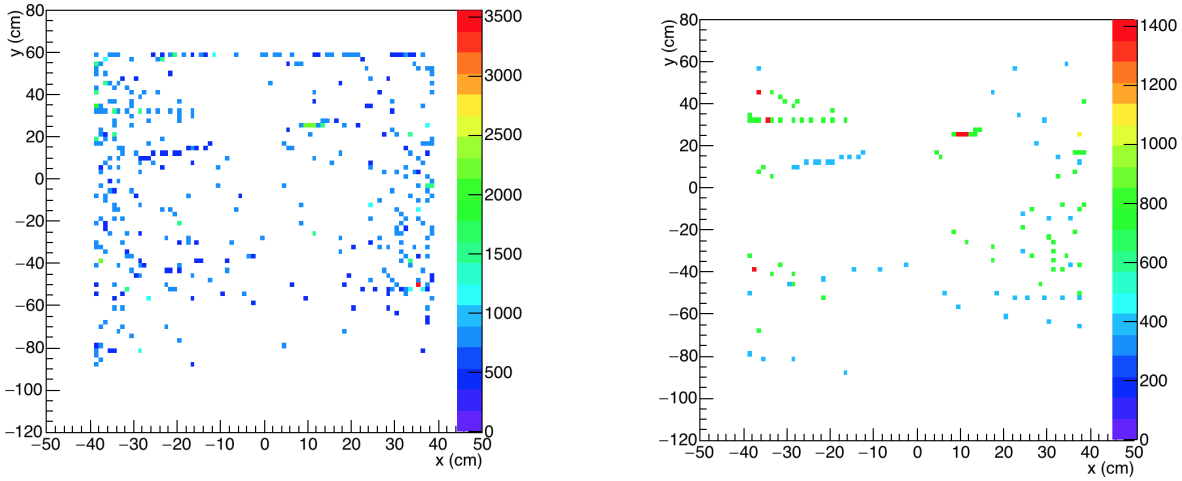

(a) (b)

Figure 5.18: Position distribution on the TT surface of hits released by all particles (left) and only by muons (right).

CHAPTER 6

DETECTOR STUDIES WITH PARTICLE BEAMS

6.1 Design and implementation of the test for the emulsion detector

In view of the Technical Design Report to be submitted in 2018, it is important to test the innovative technological solutions foreseen for the neutrino detector. We have tested the Compact Emulsion Spectrometer (CES) and the matching between emulsion films and gaseous detectors, GEM.

With the ECC technique in magnetic field it is possible to determine the electric charge and the momentum of the charged particles by measuring the track curvature. It is thus important to separate the consecutive films in order to create a sufficient lever arm and to minimize the effects of multiple Coulomb scattering on the measurement of the magnetic deflection.

The Emulsion Cloud Chamber technique in a magnetic field was tested in 2008 with a pion test beam performed at the KEK facility in Japan [94]. The spectrometer prototype was composed of three OPERA-like emulsion sheets interleaved with two vinyl chloride plates with a 4×4 cm^2 hole in the center, thus limiting the sensitive detector area. The two spacers were used to produce a 1.5 cm air gap each. Two 200 μm thick Plexiglas plates were also placed on both sides of the spacers to prevent the emulsion films from bending. The momentum was determined for charged pions of 0.5, 1.0 and 2.0 GeV/c with a resolution of 13%. Results showed that, in this momentum range, the electric charge could be determined with a significance level better than the three standard deviations. With that setup, a Geant4 simulation, performed assuming 1 μm accuracy on the alignment of the emulsion films, showed a good agreement with the data. Using the simulation results, it was seen (see paragraph in sec. 3.1.1) that it was possible to distinguish the charge and to measure the momenta up to 10 GeV/c.

In SHiP, the challenge is designing a detector with a larger sensitive area with respect to the Japanese prototype, while still maintaining the emulsion films perfectly equidistant and with an overall thickness of a few centimetres. The idea is to fill the gaps between the emulsion sheets with materials of very low density instead of using air gaps. Rohacell spacers, with a density of 57 mg/cm^3, satisfy this requirement: they allow the necessary spacing between two consecutive emulsion films while minimising the effects of multiple coulomb scattering on the measurement of the magnetic deflection.

I have actively taken part to a test beam performed in September 2015 to evaluate the performances of the so-designed CES at different impinging angles and momenta of the tracks and thus either validate or discard the possibility of using Rohacell as spacer.

Testing the matching between emulsion films and gaseous detectors is necessary to choose which technology to use for the electronic tracking chambers that are foreseen to interleave the walls of ECC bricks. As already mentioned in the paragraph on Target Trackers in sec. 3.1.1, at the moment the options under study consider, among the gaseous detectors, either the GEM or the MicroMegas. In October 2015, I took part to the first exposure of detector obtained by coupling GEM and emulsion films.

All the tests have been performed at CERN, using the test beam facilities at both the PS and the SPS. I performed the analysis of emulsion films in the emulsion laboratory at the University of Naples. Results are presented in sec. 6.4.

6.1.1 Compact Emulsion Spectrometer

The first prototype of Compact Emulsion Spectrometer made with Rohacell as spacer between emulsion films was tested at the CERN PS East Area on the T9 beam line.

The test beam was performed in collaboration with the Nagoya group that also provided the emulsions used for the test. The films were prepared in the middle of August 2015 in Nagoya using a new gel produced at the University of Nagoya with a grain density of 50 grains/100 μm, thus higher than that of the OPERA films (30 grains/100 μm). The gel was poured on both sides of a 170 μm-thick polystyrene base, then cut with a 125×100 mm^2 size. Each emulsion layer was 60 μm thick for a total emulsion thickness of 290 μm. The so produced films were shipped from Japan to CERN by plane.

The target unit used for the test was made of four 1.5 cm thick rohacell layers each interleaved with an emulsion film, for a total of five emulsion films. A sketch and a picture of the target unit is shown in fig. 6.1. The ensemble of rohacell layers and emulsions was placed in a plastic box closed at both ends by covers held in place by screws, needed to apply a small pressure on the whole system to prevent the displacement of emulsion films during the exposure. To ensure light tightness and to prevent any damage to the emulsion films, the plastic box was wrapped in an aluminium-laminated film (100 μm thick) package.

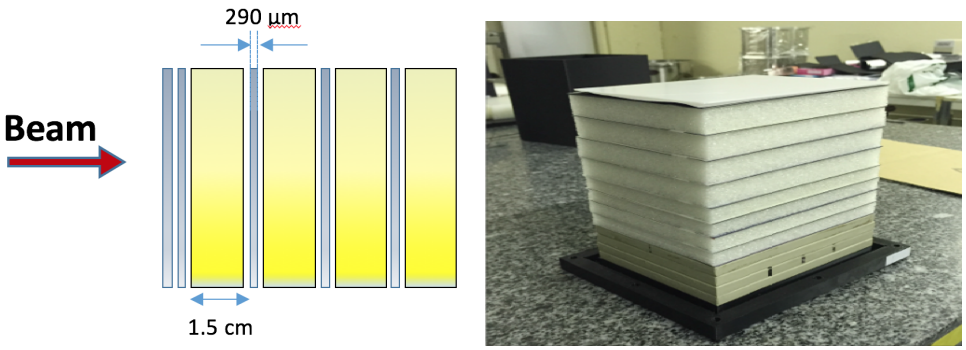

(a) (b)

Figure 6.1: Sketch (left) and picture (rigth) of the CES target unit.

The aim of the test was to check the capability to measure the charge and the momentum of tracks though their bending in a magnetic field. To this purpose, the magnet MNP17 (see fig. 6.2) was used, providing a magnetic field up to 1 T and the possibility to invert the field polarity.

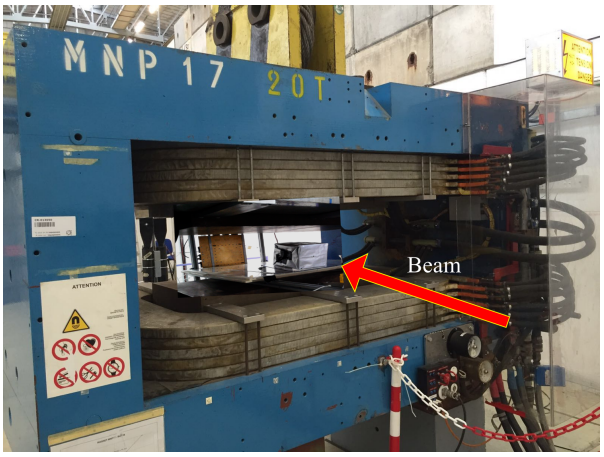

Figure 6.2: Photograph of the experimental setup at the PS-T9 beam line.

The test was performed exposing the CES to pion beams of different momenta. Since emulsion films do not have any time information, different impinging particle angles have been used to distinguish the different runs. A schematic representation of the pion exposures at different momenta in the $\theta_x - \theta_y$ plane is shown in fig. 6.3. The runs performed at different θ_y but identical θ_x have the same impinging particle momentum. With a positive inclination ($\theta_y \approx 5°$) along the y axis and a positive polarisation of the magnetic field, 8 exposures were performed at different angles along the x axis (θ_x) ranging from -20° up to 30°, each with a different value of the particle momentum (1, 2, 4, 8 and 10 GeV). The same approach was followed for the opposite field orientation, using this time a negative inclination along the y axis so to be able to distinguish the tracks having the same θ_x. On average, 700 - 1500 tracks were collected per cm^2 and per angle.

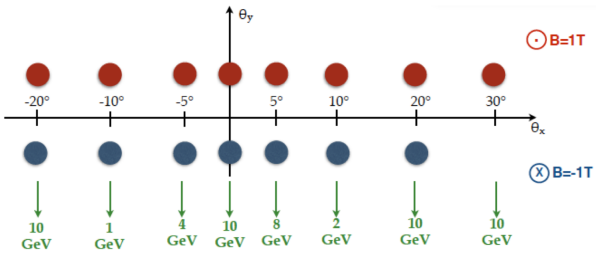

Figure 6.3: Schematic plot in the θ_x-θ_y plane of the pion exposures at different momenta.

6.1.2 Matching between emulsion films and target tracker system

The test of the detector made of emulsion films and GEM was performed in October 2015 at the CERN SPS on the H4 beam line. It was the first coupled exposure between a GEM and an emulsion detector, necessary to choose the electronic tracking chambers for the SHiP experiment. The aim of the test was to measure the position resolution of the GEM chamber as a function of the track inclination and of the magnetic field polarisation.

The required field of 1 T strength was provided by the Goliath Magnet described in chapter 3.

Scintillators with SiPM and PMT readout (T1 and T2) were placed in front and behind the magnet cavity assuring a triggered active area of ~ 4 cm^2. Two tracking stations (C1 and C3), each consisting of 20-cm-spaced XY triple-GEM chambers, were placed one 3.5 m upstream and one 3.5 m downstream of the GEM-Emulsion detector. A triple GEM (C2) was placed inside the magnet cavity on a rotating platform to perform exposures at different angles. The layout of the setup is displayed in fig. 6.4.

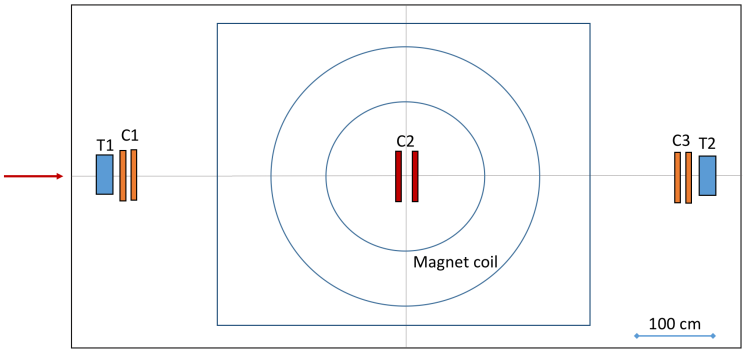

Figure 6.4: Sketch of the experimental setup: in blue the two scintillators (T1 and T2) used for trigger, in orange the two pairs of triple GEM chambers (C1 and C3) acting as forward and backward tracking stations; in the center of the setup, in red, the GEM-Emulsion detector (C2) with emulsion films.

On the GEM upstream surface, an emulsion doublet called Changeable Sheet (CS) was attached, as shown in fig. 6.5. A CS is a couple of emulsion films vacuum packed together in an

aluminium-laminated package (fig. 6.6). The GEM-Emulsion detector was exposed to 150 GeV/c muons.

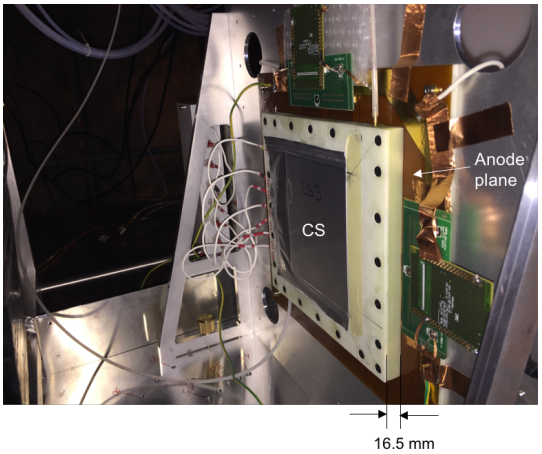

Figure 6.5: Changeable Sheet (CS) envelope attached to the upstream side of the GEM detector.

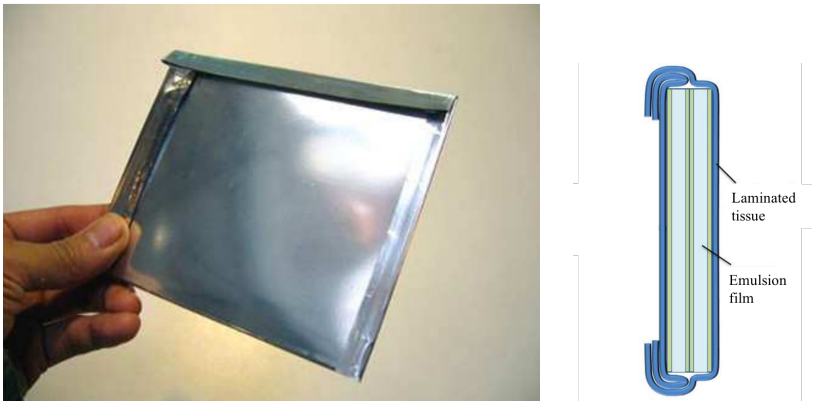

(a) (b)

Figure 6.6: Packed CS (left) and schematic drawing of the cross-section (right).

Given the micrometric accuracy of the emulsion detector, the resolution of the GEM-Emulsion detector is fully dominated by that of the GEM. Being the expected GEM accuracy always better than 400 μm, the exposure was planned in order to have an average distance of adjacent tracks of $\sim 3\sigma = 1.2$ mm. This set an upper limit of 50 tracks/cm^2 to the track density for each angular exposure and required to displace the setup by about 10 cm with respect to the beam axis. In total three sets of exposures were performed: at 0 T, 1 T and -1 T, respectively. In each exposure the GEM-Emulsion detector was rotated in oder to have 0°, 7.5°, 15° impinging angles. With the positively polarised field two additional exposures at 30° and 45° were performed. An exposure at 30° was also done in absence of magnetic field.

6.2 Activity in the emulsion facility

The preparation of the emulsion targets and the subsequent development of the emulsion films was performed in the emulsion laboratory at CERN previously used for both CHORUS and OPERA experiments (fig. 6.7).

Figure 6.7: The emulsion laboratory at CERN

To perform these tests, the facility was renovated. New humidifiers and conditioners were installed in order to guarantee a stable (20 ± 1)°C temperature and a (60 ± 2)% humidity level necessary to handle the emulsion films. Several precautions were also taken in order to make the laboratory an effective dark room equipped with red lights (the emulsion films are not sensible to this wave-length). Two different areas were also created: one room was used for the assembling of the target units and another one was equipped with a thermalized development chain to keep the solutions at the constant temperature of 20°C.

We assembled the target units in the emulsion laboratory just before the exposure to particle beams and we disassembled them immediately after to reduce the accumulation of background tracks from cosmic rays. Then we performed the development.

The development is a process that makes the latent image visible by the reduction of silver ions to metallic silver. It is made of five steps.

1. *Development*: The solution is made with Fuji Developer and Fuji Starter in demineralized water. Chemical agents reduce the crystals containing a latent image center while leaving the remnants unchanged. The emulsions are left in this solution for 25 minutes.

2. *Stop*: To stop immediately the development process and control precisely the time, a bath with acetic acid dissolved in water is used. As a matter of fact, the action of chemical developers is strongly dependent on pH: the less alkaline the environment, the less active the developer is. This step lasts 10 minutes.

3. *Clean*: To clean from any remains of chemicals, emulsions are left in water for 10 minutes.

4. *Fix*: The fixation bath is a solution of Fuji UR-F1 (Acetic Acid, Sodium Thiosulphate, Sodium Acetate, Sodium Sulfite and Ammonium Thiosulfate) in water. It removes all the residual silver halide, leaving the metallic silver to form the image. After one hour in this bath a check of the transparency of the emulsion films is performed. If the check gives a positive result, it is possible to move to the last step of the development chain, otherwise, the emulsions are left in the fixation bath and checked every 20 minutes until the desired transparency is reached.

5. *Washing*: To remove all the silver thiosulphate complexes in the emulsion, which could otherwise obscure the image, the films are washed in circulating water for 80 minutes.

At the end of the development process, the emulsions are left to dry for 24 hours before performing a glycerine treatment. Indeed, after the development process, the emulsion layers reach a thickness of ~30 μm because of the empty spaces left from the removal of the silver halides. This last step is necessary to reinflate the emulsion to their original thickness of 60 μm to avoid the shrinkage effect on track slopes. The emulsion films are left for two hours in a bath of 35% of glycerine and water. In this way the water penetrates the emulsion layer and the glycerine fills the holes left from the silver halides.

In the end, the emulsions are dried at a constant humidity level of (60 ± 2)% for two days.

6.3 Emulsion scanning

6.3.1 The scanning system

Emulsion films are analysed by means of automated microscopes which allow for fast extraction of physical information from emulsion sheets, after they have been exposed to particle radiation. For the OPERA experiment two different scanning systems were developed: one in Japan, the Super Ultra Track Selector (S-UTS) [125], and one by a collaboration of the different european laboratories, the European Scanning System (ESS) [126–129].

The ESS is a microscope equipped with a computer-controlled monitored stage, movable along both X and Y axes and in the Z direction, a dedicate optical system and a CMOS Mega-pixel camera mounted on top of the optical tube. For each field of view, it executes the following steps:

- local tomography;
- cluster recognition;
- grain selection;
- three-dimensional reconstruction of aligned cluster grains;

- parameter extraction for each grain sequence.

The sensor size, the objective magnification (50X) and the setup conditions give a field of view of about 390×310 μm^2 and image pixels of about 0.3×0.3 μm^2. In the Z direction, 15 frames per 44 μm emulsion layer are acquired. The CMOS camera grabs 376 frames per second (fps), therefore an acquisition time of about 55 ms is needed for each field of view. 125 ms are then used to move the stage to the next field of view, a step of ~300 μm. Hence, a typical data taking cycle for each field of view takes ~180 ms. Considering a superimposition between contiguous fields of 30 μm, the whole emulsion surface is scanned with a velocity of 20 cm^2/h.

An upgrade of the ESS system was made by the Naples emulsion scanning group [130]. The use of a faster camera with smaller sensor pixels and a higher number of pixels combined with a lower magnification objective lens, together with a new software LASSO [131] has allowed to increase the scanning speed to 84 cm^2/hour, more than a factor of four larger than before.

The lens of the microscope guarantees a submicron resolution and, having a working distance in Z longer than 300 μm, to scan both sides of the emulsion film. To make the optical path homogeneous in the film, an immersion lens in an oil with the same refraction index of the emulsion is used. A single field of view is 800×600 μm^2; larger areas are scanned by repeating the data acquisition on a grid of adjacent fields of view.

6.3.2 Track reconstruction in emulsion films

The images grabbed by the digital camera with a stop-and-go algorithm are sent to a vision processing board in the control workstation to suppress noise.

Three-dimensional sequences of aligned clusters (grains) are recognised and reconstructed by the CPUs of the host workstation. The track recognition procedure is a quite complex process executed by the LASSO software tracking module. The steps of the algorithm for the microtrack reconstruction are described in [131].

Microtracks are identified by a sequence of grains with a linear grain density higher than that measured in any other direction. This suggests that, for their reconstruction, a 4-dimensional histogram in angular and space coordinates has to be used. The peaks of the histogram are isolated and considered as microtracks candidates. They are composed by all the grains contained in the histogram peak which can be at least 6 or at the most 16. At this point,. coordinate, slopes and the χ^2 of the microtrack are computed, as well as a likelihood score to separate real tracks from fake ones by combinatorial background. The position assigned to a microtrack is its intercept with the nearest plastic base surface.

Once microtracks have been reconstructed, the following steps of the analysis are performed with a dedicated offline software [132]. After development, the thickness of the emulsion layer turns out to be reduced (*shrinkage*) due to the dissolution of silver halides in the fixing phase. The glycerin treatment described in sec. 6.2 corrects this effect, but only on large scales. Therefore, as a first step, a procedure aiming at a finer correction of the shrinkage is applied. Subsequently, the

two corresponding track segments in either emulsion layers are linked forming a so-called base track (BT): this step is called *linking*. This is important to reduce the instrumental background due to fake combinatorial alignments and to increase the precision on the reconstruction of the track angle, minimising distortion effects.

The base tracks are formed linking the closest grains to the plastic base in the two different emulsion layers and are selected on the basis of a χ^2 cut, defined as:

$$\chi^2 = \frac{1}{4}\left[\frac{(\theta_{X_t}-\theta_{X_{BT}})^2}{\sigma_X^2}+\frac{(\theta_{X_b}-\theta_{X_{BT}})^2}{\sigma_X^2}+\frac{(\theta_{Y_t}-\theta_{Y_{BT}})^2}{\sigma_Y^2}+\frac{(\theta_{Y_b}-\theta_{Y_{BT}})^2}{\sigma_Y^2}\right]$$

where: $\theta_{X(Y)_{b(t)}}$ are the X and Y angular projection of the microtracks in the bottom (b) and top (t) emulsion layer, while $\theta_{X(Y)_{BT}}$ are the X and Y angular projection of the basetracks and $\sigma_{X(Y)}$ are the angular resolution of the microtracks.

The full-volume wide reconstruction of particle tracks requires connecting base-tracks in consecutive films. In order to define a global reference system, a set of affine transformations has to be computed to account for the different reference frames used for data taken in different plates. Affine transformations correct also misalignments. An affine transformation is given by:

$$\begin{pmatrix} x_M \\ y_M \end{pmatrix} = \begin{pmatrix} a_{11} & a_{12} \\ a_{21} & a_{22} \end{pmatrix}\begin{pmatrix} x_t \\ y_t \end{pmatrix} + \begin{pmatrix} x_0 \\ y_0 \end{pmatrix} \tag{6.1}$$

where x(y)$_M$ are the measured coordinates of the penetrating tracks, while x(y)$_t$ are the expected ones. The z coordinate is not affected by these misalignments and, consequently, the transformation matrix is a 2×2 matrix and the total number of parameters to be found is six: the four elements of the matrix and x_0 and y_0, the offset parameters, responsible for the translations. These parameters are identified using the least square method maximising the track coincidences between two consecutive films.

6.4 Results

6.4.1 Compact Emulsion Spectrometer

I scanned for each emulsion film an area of 10×8 cm^2 leaving 1 cm from each border where the distortions of the emulsion films are larger and can thus effect the scanning and track reconstruction efficiency.

The angular distribution of the reconstructed base-tracks in one emulsion plate is shown in fig. 6.8.

To align the different emulsion films, I used the peak at 10 GeV with nominal $\tan\theta_x = 0$ and $\tan\theta_y = -0.1$. Indeed, being a peak made of high momentum tracks it suffers less of bending in magnetic fields. Hence we can assume these tracks to be straight and use them to recreate a common reference system for all the emulsion films with the procedure described in 6.3.2.

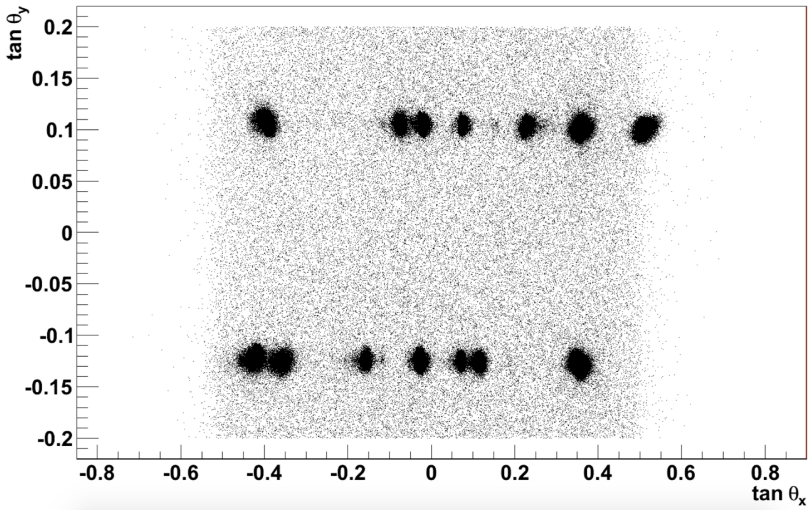

Figure 6.8: Angular distribution of reconstructed base-tracks in one of the scanned emulsion plates.

After having aligned the five films separated by the 1.5 cm of rohacell (fig. 6.1(a)), I have reconstructed the tracks and I have considered for the subsequent analysis only those having at least three consecutive segments in order to estimate the particles' momenta and charge using the sagitta method (fig. 6.9). The sagitta values computed for a baseline of 3 cm and for the different particle momenta are reported in tab. 6.1.

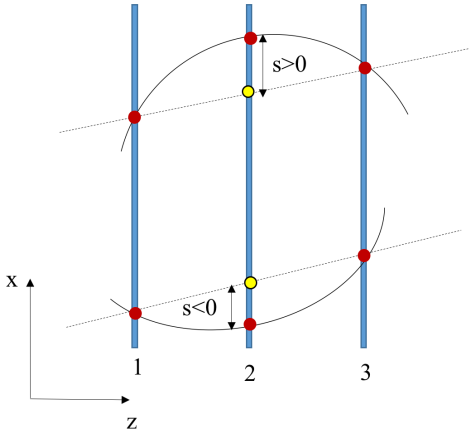

Figure 6.9: Schematic display of the sagitta method used to estimate both the particle momenta and the charge using the sign of the computed sagitta.

I have focused my analysis on the peaks of 2 and 4 GeV/c. The reconstructed sagitta for these two peaks and the corresponding gaussian fit is displayed in fig. 6.10. For the peak at 2 GeV/c, I have measured a central value of the sagitta of (17±2) μm, while for the peak at 4 GeV/c I have measured a central value of (-6.7±1.0) μm.There is a fair agreement between average measured

p (GeV/c)	Sagitta (μm)
1	34
2	17
4	8.5
8	4.3
10	3.4

Table 6.1: Absolute sagitta for different particle momenta and for a baseline of 3 cm.

sagitta values and nominal ones. However the standard deviation (σ) of the two distributions, (15.5±0.5) μm for the 2 GeV/c peak and (21.6±0.4) μm for the 4 GeV/c peak, is much wider than expected, thus spoiling the charge measurement. As a matter of fact, for the 2 GeV/c peak, (83 ± 8)% of the tracks show a positive value of the sagitta and hence their charge is correctly identified. The percentage of tracks with proper charge identification is (64 ± 5)% in the 4 GeV/c peak.

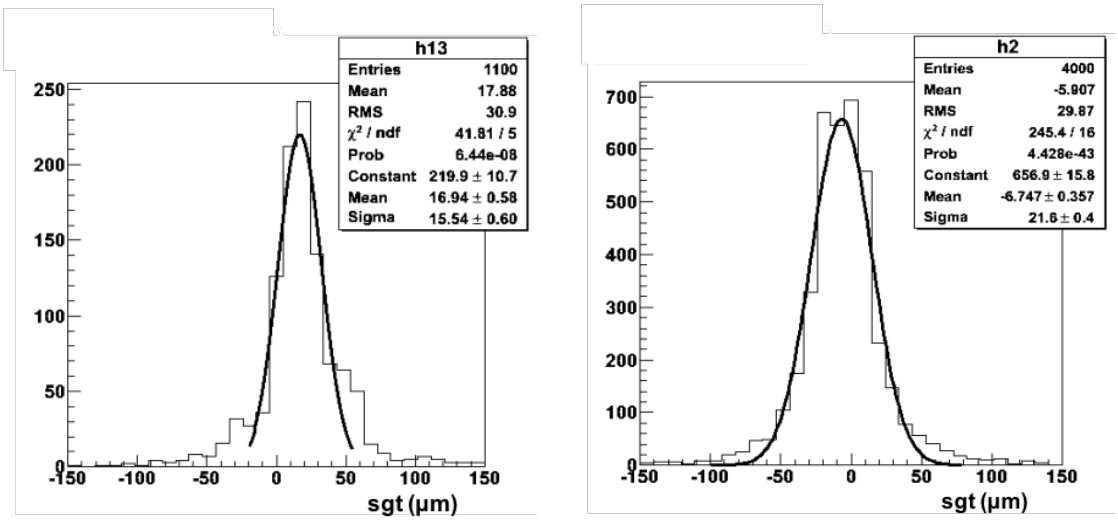

(a) (b)

Figure 6.10: Reconstructed sagitta and corresponding gaussian fit for the peak with momentum 2 GeV/c (left) and 4 GeV/c (right)

The reason for such a wide σ is due to the non perfect planarity of the rohacell layers. I have indeed observed a dependence of the slope of the tracks in the X projection as a function of their position along the x axis, as it can be seen in fig. 6.11 (a). This spoils the track reconstruction being both the alignment and the tracking algorithm optimised for emulsion films perfectly planar as in the OPERA experiment, where emulsions were interleaved with lead.

I performed a first attempt to improve the results by fitting this dependence and trying

to correct the effect. Results of the fit and the $\tan\theta_x$ dependence on x after the correction are displayed in fig. 6.11 (b) and (c). The correction I applied modified only the slope of the reconstructed tracks while leaving unaltered their position on the emulsion plate. Repeating the procedure for both track reconstruction and sagitta evaluation, I obtained no significant improvements on the results: it is necessary to apply a correction which not only corrects the slopes of the tracks but also their position on the emulsion films.

We can conclude saying that the Rohacell solution for the CES shows a fine local resolution, but it is affected by planarity problems on bigger scales being difficult to maintain the gap stability with an accuracy better than 0.2 mm.

A new solution for the realisation of the CES foresees the use of precise 1.5 cm thick rigid frames with a thin film (mylar) stretched over as a mechanical support for the emulsion (see fig. 6.12). This should guarantee the emulsion flatness and it is also more lightweight with respect to Rohacell and will be soon tested.

6.4.2 Matching between emulsion films and GEM

For this analysis, I scanned an area of 8×8 cm^2 on each emulsion layer of each film leaving 1 cm from the border of the GEM chamber (10×10 cm^2) to avoid fiducial volume effects.

To match the pattern of reconstructed tracks in the emulsion and in the GEM detector I used the alignment algorithm described in the following.

First of all the two patterns are rotated around their center of gravity with an angular step $\Delta\phi \sim 1$ mrad. For each step a 2D-histogram is filled with the difference between the x and y coordinates of GEM and emulsion tracks. The bin dimension is chosen to be approximately equal to the resolution of the GEM-Emulsion detector estimated in paragraph 6.1.2: therefore when the two patterns are well matched, the signal is expected to be in one bin. The bin of the histogram with the maximum number of entries is retrieved and plotted in fig. 6.13. The peak of the distribution allows to define the rotation angle ϕ and, from the corresponding histogram, also the x-y offset to be used for aligning the two patterns.

After this first rough alignment, I used a finer alignment algorithm with affine transformations, as those described in paragraph 6.3.2. By applying to one of the two track patterns the affine transformation evaluated as described above, a set of track segments in both the emulsion and in the GEM sub-detectors is defined in a common reference system. Those track segments are used to estimate the tracking accuracy of the whole detector. The track segment reconstructed in the emulsion has been extrapolated to the nominal position of the GEM anode and its position has been compared with the GEM hit as shown in fig. 6.14. The σ of the gaussian fit provides the resolution on the position.

In the configuration with $B = 0$ T and an incident perpendicular angle of the particle, the GEM detector has a position resolution of $\sigma_{B=0,\theta=0} = (54\pm2)$ μm. The resolutions of GEM for configurations with different slopes and intensity of the magnetic field are reported in table 6.2

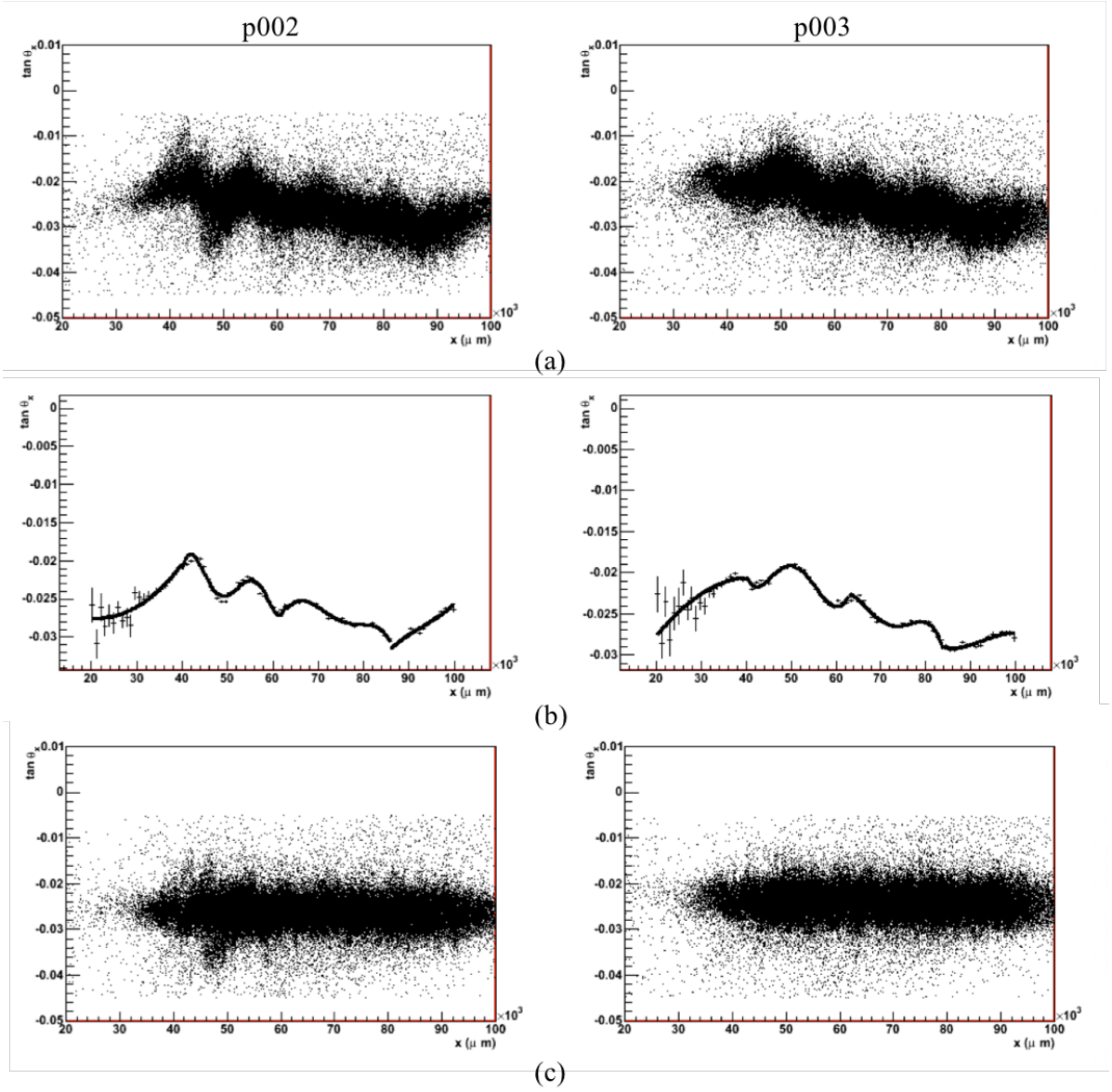

Figure 6.11: (a) As an example, observed dependence of the X slope of the reconstructed base-tracks on their position along the x axis for two different emulsion plates, identified by the labels $p002 \rightarrow p003$. (b) Fit of the dependence of $\tan\theta_x$ from x. (c) $\tan\theta_x$ dependence on x for the different plates after having applied the correction.

and in fig. 6.15. In fig. 6.17 the gaussian fitted variance distributions for $\theta = 0°$ and B = 0 T, $\theta = 7.5°$ and B = +1 T and $\theta = 15°$ and B = -1 T are reported.

As it can be inferred from the reported results, the resolution performances of the GEM detector depend strongly both on the track slope and on the magnetic field. A non-null incident angle of the incoming charged track displaces the electron avalanche associated to the charged crossing track, with a corresponding broadening of the charge distribution on the readout strips,

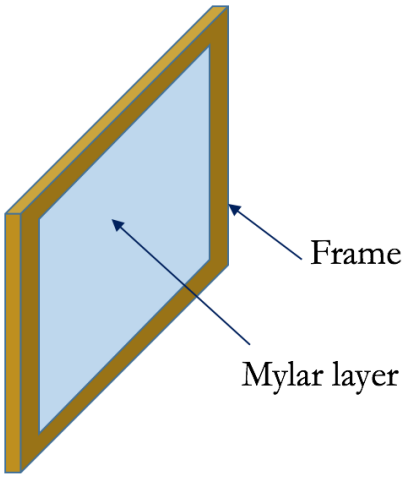

Figure 6.12: New solution for a Compact Emulsion Spectrometer using 1.5 mm thick rigid frames with a thin film (mylar) stretched over as a mechanical support for the emulsion.

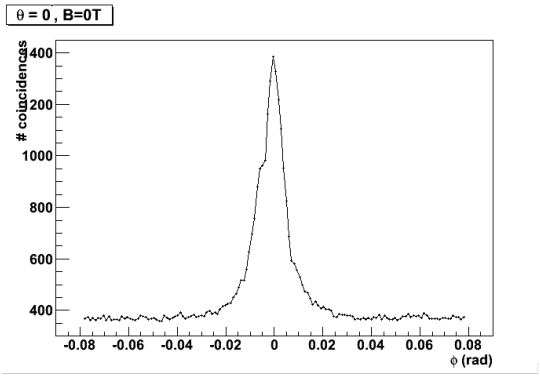

Figure 6.13: Number of coincidences computed at different ϕ rotation angles between the CS tracks and the GEM hits. The distribution is peaked at the ϕ value to be used as a start for the alignment procedure between CS and GEM.

thus worsening the estimate of the position. This effect is amplified for the $B = -1$T magnetic field which contributes to the displacement of the electron avalanches, as it can be seen in fig. 6.16 where a sketch of the avalanche development in the GEM chamber is shown for a straight track both in absence and with magnetic field.

The positive polarisation of the field ($B = +1$T), on the other hand, produced a Lorentz angle opposite to the particle inclination, thus counterbalancing the effect of an increasing incident angle of the track. This is visible already for an inclination of 7.5° where $\sigma = (132 \pm 6)$ μm and it even more evident at 15° where the resolution is $\sigma = (63 \pm 2)$ μm, compatible with the intrinsic resolution in absence of magnetic field. Further increasing the particle incident angle leads to a broader charge distribution on the readout strips and thus to a degradation on the position

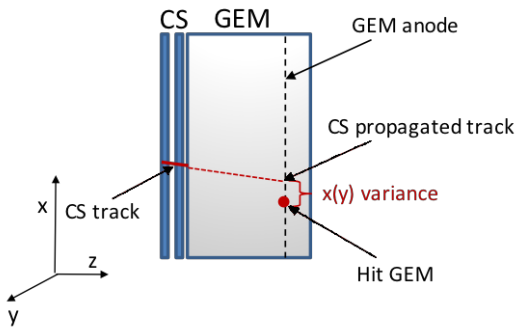

Figure 6.14: Scheme of the GEM-Emulsion detector setup. The axes of the reference frame are taken in such a way that the z axis is parallel to the beam, the x axis is parallel to the direction of the magnetic field.

	$\sigma(\mu m)$		
	B=0T	B= -1T	B=+1T
θ = 7.5°	154±15	221±13	132 ± 6
θ = 15°	218±17	369±36	63±2

Table 6.2: Position resolutions of GEM for different slopes and values of the magnetic field.

resolution: σ = (220±9) μm for θ = 30° and σ = (320±40) μm for θ = 45°. Therefore 15° corresponds to a rather complete compensation of the Lorentz angle. It is indeed possible to note how, within the errors, the two curves in fig. 6.15 for B = 1T and B = 0T are almost parallel for $\theta > 15°$, as expected, being the two configurations shifted of a 15° phase corresponding to the Lorentz angle of the electron avalanche.

The resolution at θ = 0° and B =0 T complies with the needs of the SHiP experiment. The degradation of the resolution for inclined tracks spoils significantly the performances of the GEM detector. Nevertheless the implementation of micro-TPC mode algorithm for the reconstruction of tracks in the GEM detector is expected to improve considerably the position resolution also for inclined tracks and in presence of magnetic field.

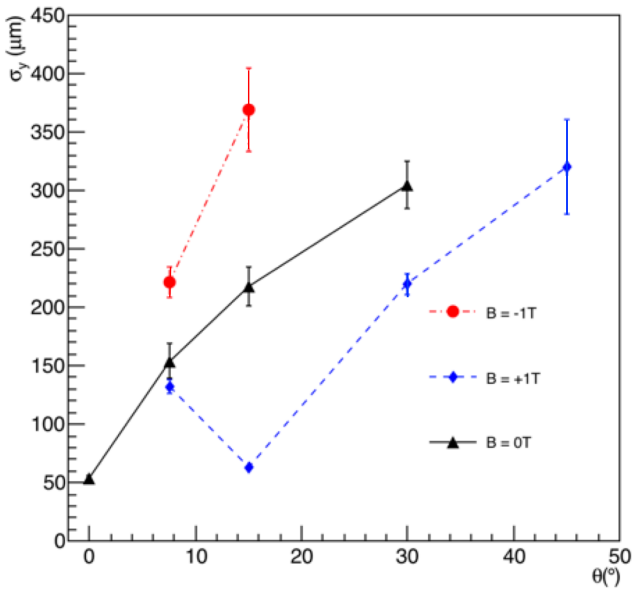

Figure 6.15: Resolution of the GEM as a function of the incident angle and for different values of the magnetic field.

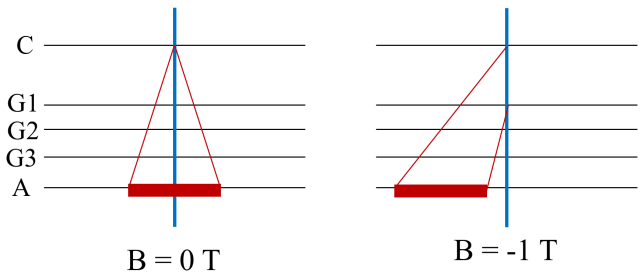

Figure 6.16: Sketch of the avalanche development in a GEM chamber for a straight track in absence of magnetic field (left) and with magnetic field (right).

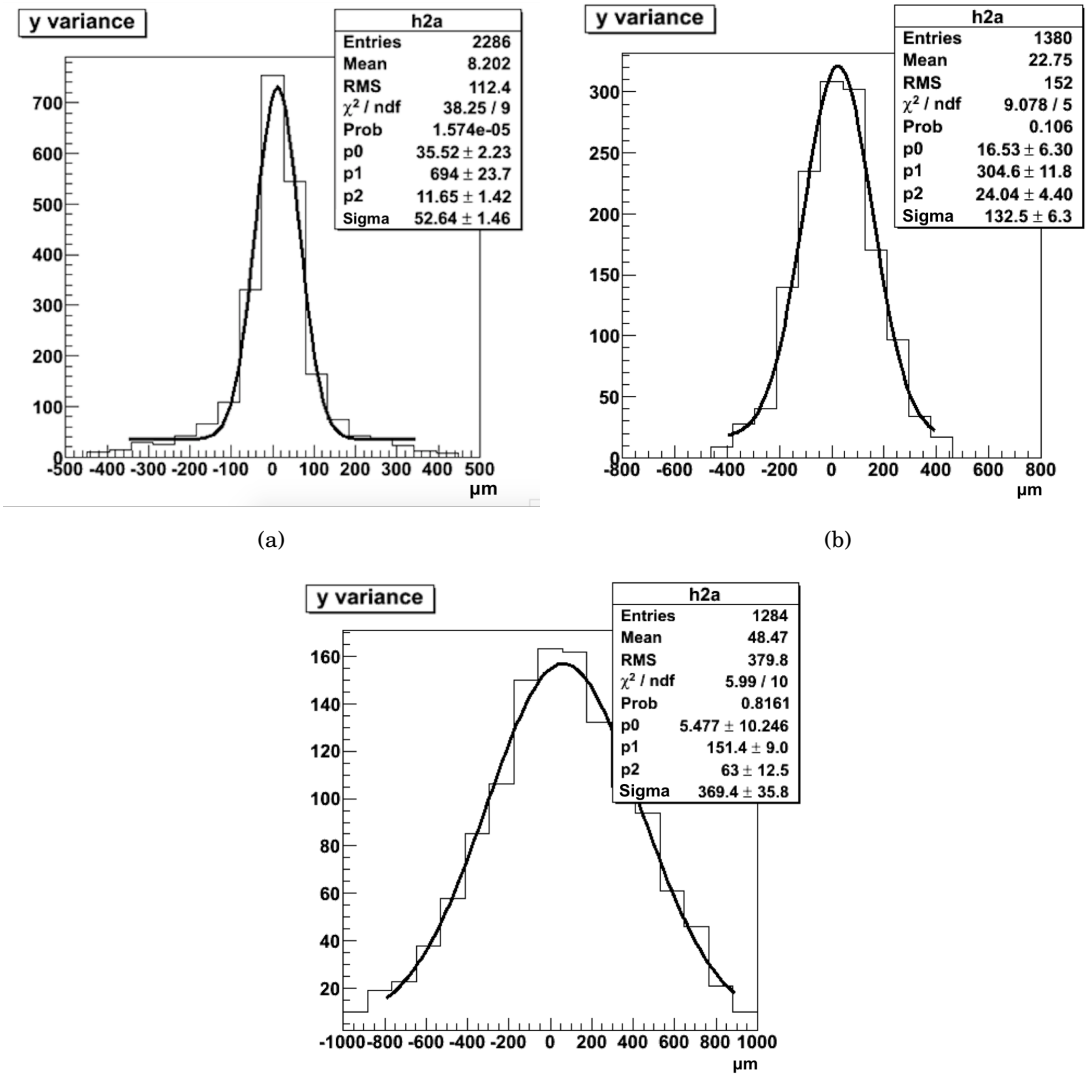

(a) (b)

(c)

Figure 6.17: Variance between y coordinate of GEM hits and CS tracks for $\theta = 0°$ and B = 0 T (a), $\theta = 7.5°$ and B = +1 T (b) and $\theta = 15°$ and B = - 1 T (c).

Conclusions

SHiP (Search for Hidden Particles) is a new general purpose fixed target experiment proposed at the CERN SPS accelerator in April 2015 with the submission of a Technical Proposal (TP) and which has received a strong encouragement by the SPS Committee towards the preparation of a Comprehensive Design Study to be submitted by the end of 2018. During my three years of Ph.D., I first contributed to the preparation of the Technical Proposal. I later started to work on the optimisation of the detector which is still ongoing and on the experimental tests devoted to investigate innovative technological solutions.

SHiP aims at searching for new physics at very weakly couplings and masses in the GeV region, thus presenting a physics program complementary to that of the LHC. The Hidden Particles originate mostly from the decay of charmed hadrons, therefore the target and the beam are optimised in such a way to enhance the production of heavy mesons. This makes the SHiP experiment a Standard Model neutrino factory too, in particular of tau neutrinos produced by the D_s decay chain.

I mainly focused on the design of the neutrino detector and on the evaluation of its performances.

The Neutrino Detector will be based on the Emulsion Cloud Chamber (ECC) technology developed by the OPERA experiment to disentangle the τ lepton production and decay vertices thanks to the the micrometric resolution of the emulsion films. This resolution together with the capability of identifying and measuring electrons makes the detector suitable to look also for Light Dark Matter (LDM) particles produced via the decay of the dark photon and scattering off the electrons in lead. Placing the Neutrino Detector in a magnetic field, there will also be the possibility to reconstruct the charge of the τ lepton daughters and hence discriminate ν_τs from $\bar{\nu}_\tau$s, thus performing the first observation of $\bar{\nu}_\tau$, the last missing tile of the SM. A Compact Emulsion Spectrometer, made of three emulsion films interleaved with 1.5 cm thick light material to reduce the Multiple Coulomb Scattering, will measure the sagitta to estimate the charge and the momentum of the hadrons produced in tau decays. The Neutrino Detector will be complemented by a muon magnetic spectrometer necessary to measure the charge and the momentum of muons produced in charged current muon neutrino interactions or in $\tau \to \mu$ decays.

In the first year of activity I have contributed to most of the analysis for the Neutrino Detector reported in the TP. Starting from a simulation of 400 GeV protons impinging on the SHiP target, I have evaluated the signal and background yield for all the different neutrino

flavours: almost 20 thousand $\nu_\tau + \bar{\nu}_\tau$ charged current interactions are expected with more than 5 thousand reconstructed events over a background of ~ 800. This will allow to study the neutrino nucleon cross-section and measure the contribution of the structure functions F_4 and F_5 which are accessible only in ν_τ interactions because of a suppression factor proportional to the square of the charged lepton mass. At leading order, in the limit of massless quarks and target hadrons, $F_4 = 0$ and $2xF_5 = F_2$, where x is the Bjorken-x variable. Calculations at next to leading order show that the F_4 contribution to this cross-section is about 1%. A non-null value of F_4 and F_5 will result in an increment of the neutrino nucleon cross-section at energies below 20 GeV, where we expect to observe about 420 $\nu_\tau + \bar{\nu}_\tau$ interactions.

I have also evaluated the SHiP performances in the measurement of the ν_τ anomalous magnetic moment. In particular, I have estimated that the background yield for this searches, mainly given by quasi-elastic electron neutrino/anti-neutrino interactions when protons in the final state are not revealed in the Neutrino Detector, $N_{bkg} = 3570 \pm 60_{stat} \pm 180_{sys}$, where I assumed to be able to reduce the systematic uncertainty on the knowledge of neutrino fluxes at a level of 5%. This is possible thanks to the known cross section and to the large expected statistics of electron neutrinos. Therefore, a 3σ evidence for a non-zero tau neutrino anomalous magnetic moment would require the observation of an excess of 540 events over the background thus exploring a region down to a magnetic moment of $\mu_\nu = 8.5 \times 10^{-8}$.

The Neutrino Detector is well suited to search for Light Dark Matter (LDM) produced by the decay of dark photons and undergoing scattering off electrons. Signal events are characterised by a single electron in the final state, as for electron neutrino interactions, which constitute the main source of background. In this study I focused on the characterisation of the background. Following the same approach as for the ν_τ anomalous magnetic moment, I have estimated the order of magnitude of the background events to expect for LDM searches. More detailed studies will be performed with more general assumptions on the dark photon and the dark matter masses.

Thanks to the large flux of ν_e and ν_μ reaching and interacting in the neutrino target, not only studies of ν_τ physics can be performed. The strange-quark content of the nucleon can be measured by means of the charmed hadron production in anti-neutrino interactions. I have estimated that there will be more than 10^5 neutrino induced charmed hadrons in 5 years of data taking. Exploiting the possibility of identifying these hadrons through the decay topology, the available statistics will exceed by more than one order of magnitude that of previous experiments. Using simulated data normalised to the expected statistics I evaluated the distribution of $\nu_\mu(\bar{\nu}_\mu)$ interactions with charm production in the x, y and E variables, providing these data to the NNPDF group. Adding these data to the NNPDF3.0 NNLO fit provided an estimate of the SHiP power in constraining the strange quark content of the nucleon. Defining $s^\pm$ as $s^\pm = s(x) \pm \bar{s}(x)$, almost a factor two gain on the accuracy is achieved in the x range between 0.03 and 0.35 for s^+ and between 0.08 and 0.30 for s^-.

During my second year of activity, I actively participated to test two innovative technological

solutions foreseen for the Neutrino Detector, i.e. the Compact Emulsion Spectrometer and the matching between an emulsion based detector and electronic gaseous detector.

The first test beam was held in September 2015 at the CERN PS to test the resolution in measuring the particles momenta and charge in magnetic field with a cell of 3 emulsion films interleaved with Rohacell as light material. The other test beam was performed in October 2015 at the CERN SPS in collaboration with the GEM Frascati group to test the matching between emulsion films and GEM detectors and to measure the resolution of the GEM in different experimental conditions (tracks incident at different angles and different polarisation of the magnetic field) exploiting the micrometric resolution of the films.

I have also performed the analysis on the emulsions exposed during the test beams using the emulsion scanning facility present at the University of Naples.

The test beam for the CES has led us to discard the option of using the Rohacell as a light material interleaved to the emulsion films. As a matter of fact, it is not able to guarantee the planarity of the emulsion films on a larger scale, which is of major importance to improve the resolution on the momentum and on the charge measurement. I have indeed found a dependence of the X-projection slope of the tracks as a function of their horizontal position as evidence of the Rohacell deformations. A possible solution for this detector is trying to use 1.5 cm thick rigid frames with a thin film (mylar) stretched over as a mechanical support for the emulsion which should guarantee the planarity of the emulsion films over their whole surface. We will soon test this solution.

The test beam with the GEM-emulsion coupled detector has shown that for an incident particle angle $\theta = 0°$ and $B = 0$T, the resolution is $\sigma = (54 \pm 2)\mu$m, thus complying with the needs of the SHiP experiment. I have also studied how the performances of the GEM detector change when dealing with inclined tracks and different polarisations of the magnetic field. I have observed a degradation of the performances for non perpendicular incident tracks due to the displacement of the electron avalanche associated to the charged crossing track, with a corresponding broadening of the charge distribution on the readout strips. The degradation is enhanced in case the polarisation of the magnetic field contributes to the avalanche displacement. Instead, it shows the same behaviour as for $B = 0$T in case of a compensating magnetic field but with a phase-shift of 15° corresponding to the Lorentz angle of the electron avalanche. The results of this test beam are reported in an article for which I am acting as a corresponding author, that is ready to be submitted to a Journal.

Concerning the optimisation studies which I have carried on mainly in the last year of Ph.D., I have designed and implemented in the official software, which during the years I have contributed to develop, a new layout for the Neutrino Detector that complies with the requirements set by the shorter muon shield design necessary to move the decay vessel closer to the proton target and hence gain in acceptance for the Hidden Particles searches and for neutrino studies.

The design of the new layout for the Neutrino Detector has been mainly driven by the

necessity of remaining in the region cleared by the background muon flux and of keeping a mass sufficient to have at least the same statistic for signal events as the one expected in the TP layout. With the current configuration, being closer to the proton target, the incoming neutrino flux is almost doubled with respect to the TP and this trend reflects also in the number of neutrino interactions, with more than 35 thousand $\nu_\tau + \bar{\nu}_\tau$ charged current deep inelastic scattering occurring in the neutrino target. The estimated performances of the Neutrino Detector in terms of muon identification and charge measurement show no significant deviations from those in the TP layout.

In this new experimental layout, I have also studied the rate of muons and electrons on the different elements of the Neutrino Detector. This study is of major importance for the Neutrino Detector because muon background rates define the rate of emulsion film replacement during the data taking and they are also necessary to define the technology to use in the Muon Magnetic Spectrometer (MMS). This analysis has shown how the largest contribution to background hits is due to an electromagnetic component originating from photons produced by muon bremsstrahlung in the most downstream part of the muon shield. Optimisation studies are ongoing to reduce the muon background component, in particular very soft muons ($p < 1$ GeV) entering the neutrino detector. In the meantime I have tested the possibility of reducing the electromagnetic component with a lead shield attached laterally to the MMS system.

All the above studies will be part of the Comprehensive Design Study document to be produced.

BIBLIOGRAPHY

[1] G. Aad et al.,
"Observation of a new particle in the search for the Standard Model Higgs boson with the ATLAS detector at the LHC",
Phys. Lett. Vol. B716, pp. 1–29, 2012,
arXiv: 1207.7214 [hep-ex].

[2] S. Chatrchyan et al.,
"Observation of a new boson at a mass of 125 GeV with the CMS experiment at the LHC",
Phys. Lett. Vol. B716, pp. 30–61, 2012,
arXiv: 1207.7235 [hep-ex].

[3] A. D. Sakharov,
"Violation of CP invariance, C asymmetry, and baryon asymmetry of the universe",
Soviet Physics Uspekhi, vol. 34, p. 392, 1991.

[4] G. Aad et al.,
"The ATLAS Experiment at the CERN Large Hadron Collider",
JINST, vol. 3, S08003, 2008.

[5] S. Chatrchyan et al.,
"The CMS experiment at the CERN LHC",
JINST, vol. 3, S08004, 2008.

[6] A. A. Alves Jr. et al.,
"The LHCb Detector at the LHC",
JINST, vol. 3, S08005, 2008.

[7] S. Alekhin et al.,
"A facility to Search for Hidden Particles at the CERN SPS: the SHiP physics case",
Rept. Prog. Phys. Vol. 79, p. 124201, 2016,
arXiv: 1504.04855 [hep-ph].

[8] G. Aad et al.,
"Search for high-mass dilepton resonances in pp collisions at $\sqrt{s}$ = 8??TeV with the ATLAS detector",
Phys. Rev. Vol. D90, p. 052005, 2014,

arXiv: 1405.4123 [hep-ex].

[9] V. Khachatryan et al.,
"Search for physics beyond the standard model in dilepton mass spectra in proton-proton collisions at $\sqrt{s} = 8$ TeV",
JHEP, vol. 04, p. 025, 2015,
arXiv: 1412.6302 [hep-ex].

[10] R. Essig et al.,
"Working Group Report: New Light Weakly Coupled Particles",
In: *Proceedings, 2013 Community Summer Study on the Future of U.S. Particle Physics: Snowmass on the Mississippi (CSS2013): Minneapolis, MN, USA, July 29-August 6, 2013*, 2013,
arXiv: 1311.0029 [hep-ph].

[11] B. Batell, M. Pospelov, and A. Ritz,
"Exploring Portals to a Hidden Sector Through Fixed Targets",
Phys. Rev. Vol. D80, p. 095024, 2009,
arXiv: 0906.5614 [hep-ph].

[12] J. Bl¸mlein and J. Brunner,
"New Exclusion Limits on Dark Gauge Forces from Proton Bremsstrahlung in Beam-Dump Data",
Phys. Lett. Vol. B731, pp. 320–326, 2014,
arXiv: 1311.3870 [hep-ph].

[13] P. deNiverville, D. McKeen, and A. Ritz,
"Signatures of sub-GeV dark matter beams at neutrino experiments",
Phys. Rev. Vol. D86, p. 035022, 2012,
arXiv: 1205.3499 [hep-ph].

[14] B. Batell, M. Pospelov, and A. Ritz,
"Exploring portals to a hidden sector through fixed targets",
Phys. Rev. D, vol. 80, p. 095024, 2009.

[15] P. deNiverville, M. Pospelov, and A. Ritz,
"Observing a light dark matter beam with neutrino experiments",
Phys. Rev. D, vol. 84, p. 075020, 2011.

[16] M. Pospelov, A. Ritz, and M. Voloshin,
"Secluded {WIMP} dark matter",
Physics Letters B, vol. 662, pp. 53 –61, 2008.

[17] B. Holdom,
"Two U(1)'s and ϵ charge shifts",

Physics Letters B, vol. 166, pp. 196 –198, 1986.

[18] J. E. Hill,
"Results from the LSND neutrino oscillation search for anti-muon-neutrino → anti-electron-neutrino",
Phys. Rev. Lett. Vol. 75, pp. 2654–2657, 1995,
arXiv: hep-ex/9504009 [hep-ex].

[19] L. B. Auerbach et al.,
"Measurement of electron-neutrino electron elastic scattering",
Phys. Rev. D, vol. 63, p. 112001, 2001.

[20] R. Dharmapalan et al.,
"Low Mass WIMP Searches with a Neutrino Experiment: A Proposal for Further MiniBooNE Running"
2012,
arXiv: 1211.2258 [hep-ex].

[21] P. deNiverville, M. Pospelov, and A. Ritz,
"Observing a light dark matter beam with neutrino experiments",
Phys. Rev. Vol. D84, p. 075020, 2011,
arXiv: 1107.4580 [hep-ph].

[22] E. Izaguirre et al.,
"Testing GeV-Scale Dark Matter with Fixed-Target Missing Momentum Experiments",
Phys. Rev. Vol. D91, p. 094026, 2015,
arXiv: 1411.1404 [hep-ph].

[23] B. Batell, R. Essig, and Z. Surujon,
"Strong Constraints on Sub-GeV Dark Sectors from SLAC Beam Dump E137",
Phys. Rev. Lett. Vol. 113, p. 171802, 2014,
arXiv: 1406.2698 [hep-ph].

[24] F. Bezrukov and D. Gorbunov,
"Light inflaton after LHC8 and WMAP9 results",
JHEP, vol. 07, p. 140, 2013,
arXiv: 1303.4395 [hep-ph].

[25] T. Asaka, S. Blanchet, and M. Shaposhnikov,
"The νMSM, dark matter and neutrino masses",
Physics Letters B, vol. 631, pp. 151 –156, 2005.

[26] T. Asaka and M. Shaposhnikov,
"The νMSM, dark matter and baryon asymmetry of the universe",
Physics Letters B, vol. 620, pp. 17 –26, 2005.

[27] E. Bulbul et al.,
"Detection of an Unidentified Emission Line in the Stacked X-Ray Spectrum of Galaxy Clusters",
The Astrophysical Journal, vol. 789, p. 13, 2014.

[28] A. Boyarsky et al.,
"Unidentified Line in X-Ray Spectra of the Andromeda Galaxy and Perseus Galaxy Cluster",
Phys. Rev. Lett. Vol. 113, p. 251301, 2014.

[29] E. K. Akhmedov, V. A. Rubakov, and A. Y. Smirnov,
"Baryogenesis via Neutrino Oscillations",
Phys. Rev. Lett. Vol. 81, pp. 1359–1362, 1998.

[30] L. Canetti and M. Shaposhnikov,
"Baryon asymmetry of the Universe in the νMSM",
Journal of Cosmology and Astroparticle Physics, vol. 2010, p. 001, 2010.

[31] L. Canetti, M. Drewes, and M. Shaposhnikov,
"Matter and antimatter in the universe",
New Journal of Physics, vol. 14, p. 095012, 2012.

[32] R. D. Peccei and H. R. Quinn,
"CP Conservation in the Presence of Instantons",
Phys. Rev. Lett. Vol. 38, pp. 1440–1443, 1977.

[33] R. D. Peccei and H. R. Quinn,
"Constraints Imposed by CP Conservation in the Presence of Instantons",
Phys. Rev. Vol. D16, pp. 1791–1797, 1977.

[34] F. Wilczek,
"Problem of Strong p and t Invariance in the Presence of Instantons",
Phys. Rev. Lett. Vol. 40, pp. 279–282, 1978.

[35] S. Weinberg,
"A New Light Boson?",
Phys. Rev. Lett. Vol. 40, pp. 223–226, 1978.

[36] M. J. Duncan, N. Kaloper, and K. A. Olive,
"Axion hair and dynamical torsion from anomalies",
Nucl. Phys. Vol. B387, pp. 215–235, 1992.

[37] S. Mercuri,
"Peccei-Quinn mechanism in gravity and the nature of the Barbero-Immirzi parameter",
Phys. Rev. Lett. Vol. 103, p. 081302, 2009,
arXiv: 0902.2764 [gr-qc].

[38] O. Castillo-Felisola et al.,
"Axions in gravity with torsion",
Phys. Rev. Vol. D91, p. 085017, 2015,
arXiv: 1502.03694 [hep-ph].

[39] F. Wilczek,
"Axions and Family Symmetry Breaking",
Phys. Rev. Lett. Vol. 49, pp. 1549–1552, 1982.

[40] N. Polonsky,
"Supersymmetry: Structure and phenomena. Extensions of the standard model",
Lect. Notes Phys. Monogr. Vol. 68, pp. 1–169, 2001,
arXiv: hep-ph/0108236 [hep-ph].

[41] P. Fayet,
"Spontaneously Broken Supersymmetric Theories of Weak, Electromagnetic and Strong Interactions",
Phys. Lett. Vol. 69B, p. 489, 1977.

[42] G. R. Farrar and P. Fayet,
"Phenomenology of the Production, Decay, and Detection of New Hadronic States Associated with Supersymmetry",
Phys. Lett. Vol. 76B, pp. 575–579, 1978.

[43] C. Collaboration,
CMS Supersymmetry Physics Results,
2017.

[44] A. Collaboration,
ATLAS exotics public results.
2017.

[45] H. K. Dreiner,
"An Introduction to explicit R-parity violation"
1997,
arXiv: hep-ph/9707435 [hep-ph].

[46] E. J. Chun and H. B. Kim,
"Nonthermal axino as cool dark matter in supersymmetric standard model without R-parity",
Phys. Rev. Vol. D60, p. 095006, 1999,
arXiv: hep-ph/9906392 [hep-ph].

[47] W. Pauli,
"Dear radioactive ladies and gentlemen",

Phys. Today, vol. 31N9, p. 27, 1978.

[48] F. Reines and C. L. Cowan,
"The neutrino",
Nature, vol. 178, pp. 446–449, 1956.

[49] Y. Fukuda et al.,
"Evidence for oscillation of atmospheric neutrinos",
Phys. Rev. Lett. Vol. 81, pp. 1562–1567, 1998,
arXiv: hep-ex/9807003 [hep-ex].

[50] N. Agafonova et al.,
"Discovery of τ Neutrino Appearance in the CNGS Neutrino Beam with the OPERA Experiment",
Phys. Rev. Lett. Vol. 115, p. 121802, 2015,
arXiv: 1507.01417 [hep-ex].

[51] K. Abe et al.,
"Observation of Electron Neutrino Appearance in a Muon Neutrino Beam",
Phys. Rev. Lett. Vol. 112, p. 061802, 2014,
arXiv: 1311.4750 [hep-ex].

[52] X. Guo et al.,
"A Precision measurement of the neutrino mixing angle θ_{13} using reactor antineutrinos at Daya-Bay"
2007,
arXiv: hep-ex/0701029 [hep-ex].

[53] F. P. An et al.,
"Spectral measurement of electron antineutrino oscillation amplitude and frequency at Daya Bay",
Phys. Rev. Lett. Vol. 112, p. 061801, 2014,
arXiv: 1310.6732 [hep-ex].

[54] J. K. Ahn et al.,
"RENO: An Experiment for Neutrino Oscillation Parameter θ_{13} Using Reactor Neutrinos at Yonggwang"
2010,
arXiv: 1003.1391 [hep-ex].

[55] S.-H. Seo,
"New Results from RENO",
PoS, vol. Neutel2013, p. 018, 2014,
arXiv: 1312.4111 [physics.ins-det].

[56] F. Ardellier et al.,
"Double Chooz: A Search for the neutrino mixing angle θ_{13}"
2006,
arXiv: hep-ex/0606025 [hep-ex].

[57] Y. Abe et al.,
"Reactor electron antineutrino disappearance in the Double Chooz experiment",
Phys. Rev. Vol. D86, p. 052008, 2012,
arXiv: 1207.6632 [hep-ex].

[58] K. Abe et al.,
"First combined analysis of neutrino and antineutrino oscillations at T2K"
2017,
arXiv: 1701.00432 [hep-ex].

[59] V. M. Hannen,
"The KATRIN neutrino mass experiment",
PoS, vol. ICHEP2012, p. 374, 2013.

[60] N. Abgrall et al.,
"The Majorana Demonstrator Neutrinoless Double-Beta Decay Experiment",
Adv. High Energy Phys. Vol. 2014, p. 365432, 2014,
arXiv: 1308.1633 [physics.ins-det].

[61] A. Gando et al.,
"Search for Majorana Neutrinos near the Inverted Mass Hierarchy Region with KamLAND-Zen",
Phys. Rev. Lett. Vol. 117, p. 082503, 2016,
arXiv: 1605.02889 [hep-ex].

[62] M. C. Chen,
"The SNO liquid scintillator project",
Nucl. Phys. Proc. Suppl. Vol. 145, pp. 65–68, 2005.

[63] K. Kodama et al.,
"Observation of tau neutrino interactions",
Phys. Lett. Vol. B504, pp. 218–224, 2001,
arXiv: hep-ex/0012035 [hep-ex].

[64] R. Acquafredda et al.,
"The OPERA experiment in the CERN to Gran Sasso neutrino beam",
JINST, vol. 4, P04018, 2009.

[65] N. Agafonova et al.,
"Observation of a first ν_τ candidate in the OPERA experiment in the CNGS beam",

Phys. Lett. Vol. B691, pp. 138–145, 2010,
arXiv: 1006.1623 [hep-ex].

[66] N. Agafonova et al.,
"New results on $\nu_\mu \to \nu_\tau$ appearance with the OPERA experiment in the CNGS beam",
JHEP, vol. 11, p. 036, 2013,
arXiv: 1308.2553 [hep-ex].

[67] N. Agafonova et al.,
"Evidence for $\nu_\mu \to \nu_\tau$ appearance in the CNGS neutrino beam with the OPERA experiment",
Phys. Rev. Vol. D89, p. 051102, 2014,
arXiv: 1401.2079 [hep-ex].

[68] N. Agafonova et al.,
"Observation of tau neutrino appearance in the CNGS beam with the OPERA experiment",
PTEP, vol. 2014, p. 101C01, 2014,
arXiv: 1407.3513 [hep-ex].

[69] J. Miller,
"Recent Results from MINERνA",
Nuclear and Particle Physics Proceedings, vol. 265, pp. 201 –204, 2015.

[70] G. Bozzi, L. Citelli, and A. Vicini,
"Parton density function uncertainties on the W boson mass measurement from the lepton transverse momentum distribution",
Phys. Rev. Vol. D91, p. 113005, 2015,
arXiv: 1501.05587 [hep-ph].

[71] M. Goncharov et al.,
"Precise measurement of dimuon production cross sections in ν_μFe and $\overline{\nu}_\mu$Fe deep inelastic scattering at the Fermilab Tevatron",
Phys. Rev. D, vol. 64, p. 112006, 2001.

[72] K. Kodama et al.,
"Final tau-neutrino results from the DONuT experiment",
Physical Review D - Particles, Fields, Gravitation and Cosmology, vol. 78, pp. 1–20, 2008.

[73] C. Albright and C. Jarlskog,
"Neutrino production of M+ and E+ heavy leptons (I)",
Nuclear Physics B, vol. 84, pp. 467 –492, 1975.

[74] M. H. Reno,
"Electromagnetic structure functions and neutrino-nucleon scattering",
Phys. Rev. D, vol. 74, p. 033001, 2006.

[75] K. Fujikawa and R. E. Shrock,
"Magnetic Moment of a Massive Neutrino and Neutrino-Spin Rotation",
Phys. Rev. Lett. Vol. 45, pp. 963–966, 1980.

[76] C. Patrignani and P. D. Group,
"Review of Particle Physics",
Chinese Physics C, vol. 40, p. 100001, 2016.

[77] R. Schwienhorst et al.,
"A new upper limit for the tau-neutrino magnetic moment",
Physics Letters B, vol. 513, pp. 23 –29, 2001.

[78] G. Radel and R. Beyer,
"Neutrino electron scattering",
Mod. Phys. Lett. Vol. A8, pp. 1067–1088, 1993.

[79] A. Benvenuti et al.,
"Observation of New-Particle Production by High-Energy Neutrinos and Antineutrinos",
Phys. Rev. Lett. Vol. 34, pp. 419–422, 1975.

[80] A. Kayis-Topaksu et al.,
"Measurement of charm production in neutrino charged-current interactions",
New J. Phys. Vol. 13, p. 093002, 2011,
arXiv: 1107.0613 [hep-ex].

[81] P. Abbon et al.,
"The {COMPASS} experiment at {CERN}",
Nuclear Instruments and Methods in Physics Research Section A: Accelerators, Spectrometers, Detectors and Associated Equipment, vol. 577, pp. 455 –518, 2007.

[82] N Abgrall et al.,
"NA61/SHINE facility at the CERN SPS: beams and detector system",
J. Instrum. Vol. 9, P06005. 55 p, 2014.

[83] F Hahn et al.,
NA62: Technical Design Document,
Tech. rep.,
CERN, 2010.

[84] M. Anelli et al.,
"A facility to Search for Hidden Particles (SHiP) at the CERN SPS"
2015,
arXiv: 1504.04956 [physics.ins-det].

[85] G. Acquistapace et al.,
"The CERN neutrino beam to Gran Sasso (NGS)"

1998.

[86] M Gyr,
"Proposal for a new servo-spill system: power requirements for different configurations".

[87] A. F. A. Ferrari P.R. Sala and J. Ranft,
"FLUKA: a multi-particle transport code"
2005.

[88] T. Bohlen et al.,
"The FLUKA Code: Developments and Challenges for High Energy and Medical Applications",
Nuclear Data Sheets, vol. 120, pp. 211 –214, 2014.

[89] M. Gilbert et al.,
"An integrated model for materials in a fusion power plant: transmutation, gas production, and helium embrittlement under neutron irradiation",
Nuclear Fusion, vol. 52, p. 083019, 2012.

[90] T. Asaka and M. Shaposhnikov,
"The *ν*MSM, dark matter and baryon asymmetry of the universe",
Physics Letters B, vol. 620, pp. 17 –26, 2005.

[91] A. E. G. De Lellis and K. Niwa,
"Nuclear Emulsions",
In: *Elementary Particles: Detectors for Particles and Radiation*,
Ed. by C. Fabjan and H. Schopper,
Springer, 2011,
Pp. 216–241.

[92] M. D. Serio et al.,
"Momentum measurement by the angular method in the Emulsion Cloud Chamber",
Nuclear Instruments and Methods in Physics Research Section A: Accelerators, Spectrometers, Detectors and Associated Equipment, vol. 512, pp. 539 –545, 2003.

[93] N. Agafonova et al.,
"Momentum measurement by the Multiple Coulomb Scattering method in the OPERA lead emulsion target",
New J. Phys. Vol. 14, p. 013026, 2012,
arXiv: 1106.6211 [physics.ins-det].

[94] C. Fukushima et al.,
"A thin emulsion spectrometer using a compact permanent magnet",
Nuclear Instruments and Methods in Physics Research A, vol. 592, pp. 56–62, 2008.

[95] A. Akindinov et al.,

"Final test of the MRPC production for the ALICE TOF detector",
Nuclear Instruments and Methods in Physics Research A, vol. 602, pp. 709–712, 2009.

[96] M. Abbrescia et al.,
"Performance of a six gap MRPC built for large area coverage",
Nuclear Instruments and Methods in Physics Research A, vol. 593, pp. 263–268, 2008.

[97] D. Gorbunov and M. Shaposhnikov,
"How to find neutral leptons of the νMSM?",
JHEP, vol. 10, p. 015, 2007,
arXiv: 0705.1729 [hep-ph].

[98] R. Brun and F. Rademakers,
"ROOT: An object oriented data analysis framework",
Nucl. Instrum. Meth. Vol. A389, pp. 81–86, 1997.

[99] S. Agostinelli et al.,
"GEANT4: A Simulation toolkit",
Nucl. Instrum. Meth. Vol. A506, pp. 250–303, 2003.

[100] T. Sjöstrand, S. Mrenna, and P. Skands,
"A brief introduction to PYTHIA 8.1",
Computer Physics Communications, vol. 178, pp. 852–867, 2008,
arXiv: 0710.3820 [hep-ph].

[101] T. Sjöstrand, S. Mrenna, and P. Skands,
"PYTHIA 6.4 physics and manual",
Journal of High Energy Physics, vol. 2006, p. 026, 2006.

[102] M Al-Turany et al.,
"The FairRoot framework",
Journal of Physics: Conference Series, vol. 396, p. 022001, 2012.

[103] "Heavy Flavour Cascade Production in a Beam Dump"
2015.

[104] C. Andreopoulos et al.,
"The GENIE Neutrino Monte Carlo Generator",
Nucl. Instrum. Meth. Vol. A614, pp. 87–104, 2010,
arXiv: 0905.2517 [hep-ph].

[105] A. Chukanoc, R. Petti, and M. Kirsanov,
OpNuage,
URL: http://astronu.jinr.ru/wiki/index.php/OpNuage.

[106] P. Astier et al.,
"Neutrino production of opposite sign dimuons in the NOMAD experiment",

Phys. Lett. Vol. B486, pp. 35–48, 2000.

[107] D. Autiero,
"The OPERA event generator and the data tuning of nuclear re-interactions",
Nucl. Phys. Proc. Suppl. Vol. 139, pp. 253–259, 2005.

[108] C. Lourenco and H. K. Wohri,
"Heavy flavour hadro-production from fixed-target to collider energies",
Phys. Rept. Vol. 433, pp. 127–180, 2006,
arXiv: hep-ph/0609101 [hep-ph].

[109] H. Abramowicz et al.,
"Measurement of charm fragmentation fractions in photoproduction at HERA",
JHEP, vol. 09, p. 058, 2013,
arXiv: 1306.4862 [hep-ex].

[110] L. Arrabito et al.,
"Electron/pion separation with an emulsion cloud chamber by using a neural network",
JINST, vol. 2, P02001, 2007,
arXiv: physics/0701192 [physics].

[111] K. Kodama et al.,
"Study of electron identification in a few-GeV region by an emulsion cloud chamber",
Rev. Sci. Instrum. Vol. 74, pp. 53–56, 2003.

[112] N. Agafonova et al.,
"Momentum measurement by the Multiple Coulomb Scattering method in the OPERA lead emulsion target",
New J. Phys. Vol. 14, p. 013026, 2012,
arXiv: 1106.6211 [physics.ins-det].

[113] B. Hosseini,
"Search for Tau Neutrinos in the $\tau \rightarrow e$ Decay Channel in the OPERA Experiment",
Ph.D. thesis, Università di Napoli Federico II, 2015.

[114] H. Abramowicz et al.,
"Experimental study of opposite-sign dimuons produced in neutrino and antineutrino interactions",
Zeitschrift für Physik C Particles and Fields, vol. 15, pp. 19–31, 1982.

[115] S. A. Rabinowitz et al.,
"Measurement of the strange sea distribution using neutrino charm production",
Phys. Rev. Lett. Vol. 70, pp. 134–137, 1993.

[116] M. Jonker et al.,

"Experimental Study of Opposite Sign and Same Sign Dimuon Events Produced in Wide Band Neutrino and Anti-neutrino Beams",
Phys. Lett. Vol. 107B, p. 241, 1981.

[117] P. Vilain et al.,
"Leading order QCD analysis of neutrino induced dimuon events",
Eur. Phys. J. Vol. C11, pp. 19–34, 1999.

[118] A. E. Asratian et al.,
"Study of D^+ and search for D^0 production by neutrinos in BEBC",
Z. Phys. Vol. C68, pp. 43–46, 1995.

[119] N. Ushida et al.,
"Cross-sections for Neutrino Production of Charmed Particles",
Phys. Lett. Vol. B206, pp. 375–379, 1988.

[120] A. Kayis-Topaksu et al.,
"Leading order analysis of neutrino induced dimuon events in the CHORUS experiment",
Nucl. Phys. Vol. B798, pp. 1–16, 2008,
arXiv: 0804.1869 [hep-ex].

[121] A. Kayis-Topaksu et al.,
"Measurement of charm production in neutrino charged-current interactions",
New J. Phys. Vol. 13, p. 093002, 2011,
arXiv: 1107.0613 [hep-ex].

[122] R. D. Ball et al.,
"Parton distributions for the LHC Run II",
JHEP, vol. 04, p. 040, 2015,
arXiv: 1410.8849 [hep-ph].

[123] R. D. Ball et al.,
"Reweighting NNPDFs: the W lepton asymmetry",
Nucl. Phys. Vol. B849, pp. 112–143, 2011,
arXiv: 1012.0836 [hep-ph].

[124] R. D. Ball et al.,
"Reweighting and Unweighting of Parton Distributions and the LHC W lepton asymmetry data",
Nucl. Phys. Vol. B855, pp. 608–638, 2012,
arXiv: 1108.1758 [hep-ph].

[125] K Morishima and T Nakano,
"Development of a new automatic nuclear emulsion scanning system, S-UTS, with continuous 3D tomographic image read-out",

Journal of Instrumentation, vol. 5, P04011, 2010.

[126] N. Armenise et al.,
"High-speed particle tracking in nuclear emulsion by last-generation automatic microscopes",
Nuclear Instruments and Methods in Physics Research A, vol. 551, pp. 261–270, 2005.

[127] L. Arrabito et al.,
"Hardware performance of a scanning system for high speed analysis of nuclear emulsions",
Nuclear Instruments and Methods in Physics Research Section A: Accelerators, Spectrometers, Detectors and Associated Equipment, vol. 568, pp. 578 –587, 2006.

[128] L Arrabito et al.,
"Track reconstruction in the emulsion-lead target of the OPERA experiment using the ESS microscope",
Journal of Instrumentation, vol. 2, P05004, 2007.

[129] M. D. Serio et al.,
"High precision measurements with nuclear emulsions using fast automated microscopes",
Nuclear Instruments and Methods in Physics Research Section A: Accelerators, Spectrometers, Detectors and Associated Equipment, vol. 554, pp. 247 –254, 2005.

[130] A. Alexandrov et al.,
"A new generation scanning system for the high-speed analysis of nuclear emulsions",
JINST, vol. 11, P06002, 2016.

[131] A. Alexandrov et al.,
"A new fast scanning system for the measurement of large angle tracks in nuclear emulsions",
JINST, vol. 10, P11006, 2015.

[132] V. Tyukov et al.,
"The FEDRA Framework for emulsion data reconstruction and analysis in the OPERA experiment",
Nucl. Instrum. Meth. Vol. A559, pp. 103–105, 2006.